NASA Contractor Report 191162

Instantaneous Velocity Field Imaging Instrument for Supersonic Reacting Flows

M.G. Allen, S.J. Davis, W.J. Kessler, H.H. Legner, K.R. McManus,
P.A. Mulhall, T.E. Parker, and D.M. Sonnenfroh
Physical Sciences Incorporated
Andover, MA

September 1993

Prepared for
Lewis Research Center
Under Contract NAS3–25790

National Aeronautics and
Space Administration

(NASA-CR-191162) INSTANTANEOUS VELOCITY FIELD IMAGING INSTRUMENT FOR SUPERSONIC REACTING FLOWS Final Report (Physical Sciences) 101 p

N94-21607

Unclas

G3/35 0198088

ORIGINAL CONTAINS
COLOR ILLUSTRATIONS

Contents

1. INTRODUCTION . . . 2
    1.1 Velocity Measurement Techniques for Supersonic Reacting Flows . . . 2
    1.2 Overview of Doppler-Shifted Fluorescence Velocity Imaging . . . 3

2. OH COLLISIONAL BROADENING MEASUREMENTS . . . 12
    2.1 Lineshape Broadening Mechanisms . . . 12
    2.2 Experimental Determination of OH (1,0) Band Collision Broadening and Shifting Parameters . . . 14

3. PULSED DYE LASER BANDSHAPE MEASUREMENTS AND MODIFICATIONS . . . 24
    3.1 Measurements of Single-Pulse Laser Bandshape . . . 24
    3.2 Relationship Between Visible and UV Bandshapes . . . 28
    3.3 Modification of Single-Pulse Bandshape . . . 33

4. SUPERSONIC FLOW FACILITY . . . 40
    4.1 Supersonic Burner Overview . . . 40
    4.2 High Frequency Pressure Transducer Design . . . 43
        4.2.1 Heat Transfer Analysis . . . 44
        4.2.2 Frequency-Response Analysis . . . 47

5. JET FLOW MODELLING AND CHARACTERIZATION EXPERIMENTS . . . 50
    5.1 Flow Topology . . . 50
    5.2 Centerline Profiles . . . 51
    5.3 Jet Flow Simulations Using SPARK . . . 54
        5.3.1 Introduction to Jet Flow Simulations . . . 54
        5.3.2 SPARK Code . . . 54
        5.3.3 Application of SPARK to Jet Flowfield . . . 54
        5.3.4 Simulation Results . . . 60
    5.4 Mean Velocity Profile Measurements . . . 70

6. IMAGING INSTRUMENT CHARACTERIZATION EXPERIMENTS . . . 75
    6.1 Experimental Setup and Signal Level Considerations . . . 75
    6.2 Data Reduction and Velocity Calculations . . . 78

7. SUMMARY AND CONCLUSIONS . . . 88

8. REFERENCES . . . 90

List of Figures

1 Schematic Illustration of the Geometry of the Linear Doppler-Shift 4

2 Schematic Diagram of Optical Access for One-Dimensional Flow Measurements 5

3 Molecular Absorption Lineshape and Laser Spectral Bandwidth Overlap for a Narrow-Bandwidth Laser 6

4 Molecular Absorption Lineshape and Laser Spectral Bandwidth for a Broad-Bandwidth Laser . . . 8

5 Molecular Absorption Lineshape and Laser Spectral Bandwidth Overlap for Equivalent Bandwidths 9

6 Schematic Diagram of Flat Flame Burner 14

7 Temperature Profiles Above Flat Flame Burner 15

8 Centerline Temperature as a Function of Equivalence Ratio for Methane-Air Mixtures 16

9 Experimental Setup for OH Collisional Broadening Measurements 16

10 Low-Pressure Discharge OH Source 17

11 OH (1,0) Band $P_1(6)$ Lineshape 19

13 OH Mole-Fraction, Adiabatic Flame Temperature, and Measured Flame Temperature for H_2-Air Flames at Various Equivalence Ratios. 20

14 Collision Width of (1,0) Band Transitions of Varying Lower State Rotational Quantum Number for Stoichiometric H_2-air Flames: Comparison With (0,0) Band Transitions. 21

15 Collision Width of the $P_{1(8)}$ (1,0) Band Transition as Function of H_2-air Equivalence Ratio: Comparison With (0,0) Band Data. 22

16 Experimental Setup for the Laser Bandshape Determinations 24

17 Average Bandshape of Multi-Mode HeNe Laser Showing Resolving Power of Interferometer . . . 25

18 Average Bandwidth of FL-3002 Laser at 250 mJ Pump Energy 26

19 Average Bandwidth of FL-3002 Laser at 150 mJ Pump Energy 26

20 Single-Pulse Bandshapes of FL-3002 Laser With 250 mJ Pump Energy 27

21 500 Pulse Average FL-3002 Laser Bandshape at 565 nm 28

22 Conceptual Diagram of a Self-Convolution 30

List of Figures (Continued)

23 Calculated Single Pulse UV Laser Bandshapes 31

24 Calculated Fluorescence Ratio versus Velocity for Measured UV Laser Bandshapes 32

25 Calculated Fluorescence Ratio versus Velocity for Isentropic Flow Variations 33

26 Schematic Diagram of FL-3002 Oscillator Cavity Configuration Showing Positioning of Partial Beam Block 34

27 Modified Single-Pulse Bandshape of the FL-3002 Dye Laser 35

28 Single-Pulse Bandshapes of Modified FL-3002 Dye Laser. 35

29 Comparison of Standard and Modified Average Visible Bandshape of FL-3002 Dye Laser. 36

30 Single-Pulse UV Bandshapes from FL-3002 Dye Laser at 283 nm. 37

31 Comparison of Measured and Calculated Average UV Bandshapes. 37

32 Comparison of Standard and Modified UV Bandshapes of FL-3002 Dye Laser. 38

33 Comparison Between UV Bandshape Calculated from Average Visible Measurement and a Gaussian Bandshape with FWHM = 0.35 cm^{-1}. 39

34 Schematic Diagram of Burner Facility Layout 40

35 Detailed Schematic of High-Pressure Burner 41

36 Nozzle Temperature and Integrated Heat Flux Profiles 42

37 Schematic Diagram of Gas Delivery System. 43

38 Pressure Transducer Mount Configuration 44

39 Calculation Domain with Specified Boundary Conditions 45

40 Calculated Temperature Distribution in Transducer Mount 46

41 Transducer Mount - final design (dimensions in inches) 46

42 Schematic Diagram of Frequency-Response Calculation Input 47

43 Frequency-Response of Transducer Assembly with Constant Thermodynamic Properties (T(z) = const = 550 K, P_{avg} = 100 psi) 48

44 Calculated Frequency-Response for Isothermal (T = 550 K) and Variable Properties Cases 48

List of Figures (Continued)

45 Diagram Showing Flow Topology of an Underexpanded Sonic Jet 50

46 Example of Centerline Static Pressure Variation for an Underexpanded Sonic Jet 52

47 Variation of Centerline Properties in Regions of Isentropic Expansion. 53

48 Flow Domain for Underexpanded Supersonic Jet 56

49 Grid Point Distribution for Every 3rd in X and Every other in Y 56

50 Outflow Pressure Boundary Condition 60

51 Centerline Flowfield Values for High Pressure Case 61

52 Mach Number for High Pressure Case 61

53 Pressure for High Pressure Case 62

54 Temperature Contours for High Pressure Case 62

55 U-Velocity for High Pressure Case 63

56 Initial SS Pressure p_1^{ss} at Outflow Boundary 63

57 Centerline Flowfield Values for High Temperature Case 64

58 Mach Number Contours for High Temperature Case 65

59 Pressure Contours for High Temperature Case 65

60 Temperature Contours for High Temperature Case 66

61 U-Velocity Contours for High Temperature Case 66

62 Centerline Flowfield Values for Reduced Co-Flow Velocity 67

63 Mach Number Contours for Reduced Co-Flow Velocity Case 67

64 Pressure Contours for Reduced Co-Flow Velocity Case 68

65 Temperature Contours for Reduced Co-Flow Velocity Case 68

66 U-Velocity for Reduced Co-Flow Velocity Case 69

67 OH Mass-Fraction Contours in Jet Flowfield 69

List of Figures (Continued)

68 Experimental Setup for Mean Velocity Profile Measurements 70

69 Doppler-Shifted OH Lineshape at Burner Throat 71

70 Doppler-Shifted OH Lineshape at 8 mm Downstream 72

71 Comparison of Measured and Calculated Mean Velocity Profiles 72

72 Example OH PLIF Images in the Jet Flowfield 73

73 Experimental Configuration for Velocity Imaging Demonstrations 75

74 Comparison of Raw PLIF Images From Slow Gating Camera and Fast Gating Camera 77

75 Comparison of OH Absorption Lineshapes at Selected Conditions in the Jet Flowfield with the UV Laser Bandshape 78

76 Comparison of the Velocity Algorithm for Thermodynamic Variations Shown in Figure 75 79

77 Comparison of the Velocity Algorithm for Various Values of the Relative Sheet Intensity 80

78 Velocity Algorithm Corresponding to the Radial Velocity Determination 80

79 Comparison of Measured and Calculated Radial Velocity Distributions 81

80 Plot of the Relative Sheet Intensity Distributions Before a Burner Firing 82

81 Comparison of PLIF Images from Forward and Backward Propagating Sheets Showing Shift of Backward Sheet 83

82 Example PLIF Images Used to Calculate the Angled Jet Velocity Component 84

83 Velocity Algorithm for Two Camera Velocity Determinations 84

84 Comparison Between Measured and Calculated Angular Velocity Distribution 85

85 Comparison Between Measured and Calculated Angular Velocity Distribution 86

List of Tables

1 Collision-Induced Absorption Frequency Shift for OH(1,0) 23

2 SPARK Code Capability 55

3 Primary SPARK Subroutines 55

4 18 Equation H_2-O_2 Chemistry Model 57

5 Reduced H_2-Air Chemistry Model 58

6 Sonic Jet Inflow Conditions 59

7 Co-flow Inflow Conditions 59

EXECUTIVE SUMMARY

This report describes the technical tasks conducted to develop and demonstrate a new gas velocity measurement technique for high enthalpy reacting flows. The technique is based on Doppler-shifted Planar Laser-Induced Fluorescence (PLIF) imaging of the OH radical. The imaging approach permits, in principle, single-shot measurements of the 2-D distribution of a single velocity component in the measurement plane, and is thus a technique of choice for applications in high enthalpy transient flow facilities. In contrast to previous work in this area, the present program demonstrated an approach which modified the diagnostic technique to function under the constraints of practical flow conditions of engineering interest, rather than vice-versa. In order to accomplish the experimental demonstrations, the state-of-the-art in PLIF diagnostic techniques was advanced in several ways. This report describes each of these tasks in detail and is intended to serve as a reference in supporting the transition of this new capability to the fielded PLIF instruments now installed at several national test facilities.

Among the new results of general interest in LIF-based flow diagnostics, this report includes a detailed set of the first measurements of the collisional broadening and shifting behavior of OH (1,0) band transitions in H_2-air combustion environments. Such measurements are critical in the design of a successful strategy for PLIF velocity imaging; they also relate to accurate concentration and temperature measurements, particularly in compressible flow regimes. Furthermore, the results shed new light on the fundamental relationship between broadening and energy transfer collisions in OH A $^2\Sigma^+$ $v' = 1$.

The first single-pulse, spectrally-resolved measurements of the output of common pulsed dye lasers were also produced during the course of this effort. As with the OH broadening measurements, these data are a significant aspect of a successful velocity imaging strategy, and also have potential implications for many other LIF measurement techniques. Our results indicated the need to modify the commercially available laser cavity in order to accommodate the constraints imposed by typical SCRAMJET combustion characteristics as well as to increase the instrument's velocity dynamic range to span an intra-image range in excess of 2 km/s.

The various technical efforts were brought together in a series of experiments demonstrating the applicability of the technique in a high pressure, high temperature H_2-air combustion system. The resultant images were compared with 2-D flow simulations in order to determine the accuracy of the instrument. Mean velocity imaging in flows with an axis of symmetry was demonstrated with an accuracy of ± 50 m/s out of an intra-image dynamic range of 1600 m/s, including reversed flow. A more complex configuration amenable to single-shot imaging in flows without an axis of symmetry was also demonstrated. Limitations imposed by available equipment resulted in an accuracy of about ± 200 m/s out of 1750 m/s in these demonstrations. Minor modifications to the present configuration were suggested to improve this performance.

In the following pages, each technical task is described in detail, along with significance of the results for the overall imaging velocimeter configuration. This report should allow the user community to integrate this new measurement capability into their existing instrumentation platforms.

1. INTRODUCTION

1.1 Velocity Measurement Techniques for Supersonic Reacting Flows

The resurgence of interest in supersonic propulsion systems (SCRAMJETS) and controlled hypersonic flight places new demands on experimental techniques for high-enthalpy combusting flow property measurements. Among the key parameters in combustor performance assessment is the vector velocity field throughout the propulsion system. Current velocity measurement techniques, such as hot-wire anemometry and laser-Doppler anemometry are generally inapplicable in high-enthalpy, combusting supersonic flow test facilities or are subject to large systematic errors. The OH fluorescence approach investigated in this Phase II SBIR program circumvents many of the inherent limitations in conventional velocity measurement technology. Furthermore, the fluorescence approach is capable of simultaneous, multi-point measurements using laser sheet illumination and fluorescence detection via sensitive, imaging detector arrays.

The experimental challenges associated with obtaining velocity measurements in high temperature, compressible flowfields are profound. Laser-Doppler Anemometry (LDA) techniques have been developed to the point where the three components of the mean and fluctuating velocity vector at a point in the flowfield can be measured. A single velocity component is measured by interfering two coherent beams (derived from a common laser source) at a point in the flowfield and detecting the period of the scattering signature from a particle traversing the resulting fringe pattern.

Although LDA finds common application in near-isothermal, low Mach number flows, it is not appropriate for all flows. In reacting flows, the density variations associated with the temperature variations in the flowfield bias the velocity statistics toward the cold portions of the flow (where the density of scattering centers is higher) and is known to skew the measured distribution of rms fluctuations. Furthermore, at the highest temperatures associated with air-breathing combustion systems (2000 to 3000 K), the seed particles themselves (typically Al_2O_3 or TiO_2) breakdown so that no LDA signal is generated. Finally, in supersonic flows with shock waves, the relatively large ($\sim 1\ \mu m$) seed particles may not always track the velocity of the gas due to the particle inertia.

Hot-wire anemometry has been used in fluid dynamics research for decades. As an intrusive technique, it is inherently highly perturbing to the flowfield downstream of the probe. In supersonic flows, the perturbation may manifest itself as shock waves emanating from the probe or the probe support. Furthermore, the wire (or film) cannot survive the high temperatures associated with combustion. Hence, this technique is unsuitable for high temperature reacting flowfields. In addition, the wire responds to a combination of density, velocity, and temperature so that independent determination of any individual quantity is ambiguous.

Non-intrusive, laser-based gas velocity measurement approaches based on flow tagging have been suggested by several groups. Optical flow tagging approaches are based on marking a line or a cross in the flow with one laser beam and then probing the marked line with a second laser beam or sheet at a known time later. The displacement of the marked gas during the known time delay gives the average convection speed during the time between the two laser pulses. This basic approach has been demonstrated using seeded biacetyl,[1] nascent molecular oxygen (RELIEF method),[2] and water vapor.[3,4] Only the water vapor technique has promise for high temperature flows. The biacetyl seed is not stable above room temperature in the presence of oxygen. The marking of the gas in the RELIEF technique is accomplished via Raman excitation of an excited vibrational level in the oxygen ground electronic state whose lifetime is too short at high temperatures to make meaningful measurements.

The water vapor tagging approach uses a tunable KrF excimer laser to dissociate H_2O into, among other products, ground state OH in a thin line along the laser beam. At some later time, a second laser is used to excite this OH line in order to record its displacement. No demonstrations to date have succeeded in reacting flows where the fluorescence from the background nascent OH distribution overwhelms the visibility of the laser-tagged molecules.

It should be recognized that the flow-tagging measurements are not a direct, spatially resolved measurement of the gas velocity. Indeed, the measurement yields meaningful results only in one-dimensional, or nominally one-dimensional, flows where no directional ambiguity of the marked gas is present. In multi-dimensional or strongly turbulent flows, the marked line or cross in the flowfield will be rapidly disrupted, rendering interpretation of the displaced fluid meaningless.

The approach investigated in this program is a *direct measurement of the velocity field* at every spatially-resolved detection point with no restrictions on the dimensionality or turbulence level of the flow. Furthermore, while the flow tagging approaches require multiple wavelengths with concommitant expensive and complex laser systems, the technique developed in this program is purposely designed to use a single, commercially available pulsed-dye laser system.

1.2 Overview of Doppler-Shifted Fluorescence Velocity Imaging

The velocity measurement approach investigated in this program is based on Planar Laser-Induced Fluorescence (PLIF) imaging of the nascent OH radical in a supersonic combusting flowfield. Details of the fluorescence process have been discussed in detail in the Phase I final report and can be found in the references 7 to 13. Briefly, we recall that the magnitude of the fluorescence signal, S_f, recorded by an individual detector element is given by

$$S_F = \int_{\omega} I_{(\omega)} g_{(\omega)} \, d\omega \cdot \frac{A}{A + Q} \cdot (f_B V_c \, N_t) \cdot \left[\eta \, \frac{\Omega}{4\pi} \right] \cdot \tau_p \qquad (1)$$

where

$I_{(\omega)}$ ≡ laser spectral intensity
$g_{(\omega)}$ ≡ absorption lineshape function
A ≡ effective radiation rate
Q ≡ effective quench rate
f_B ≡ Boltzmann population fraction in absorbing state
V_c ≡ collection volume
N_t ≡ total number density of absorbing species
Ω ≡ collection solid angle
η ≡ transmissivity of collection optics
τ_p ≡ laser pulse duration.

For clarity, throughout this report the optical frequency, ω, is given in units of cm^{-1}. The first factor in Eq. (1), the spectral overlap integral, is the velocity-sensitive term in the fluorescence equation.

The essence of LIF velocimetry is based on the Doppler-shifted absorption frequency of an ensemble of atoms or molecules. The concept is schematically illustrated in Figure 1. A group of molecules possessing a net directed velocity, denoted by the vector **v**, is intersected by a laser beam traveling with a direction and wavelength denoted by the wave vector **k**, both calculated with respect to a stationary reference

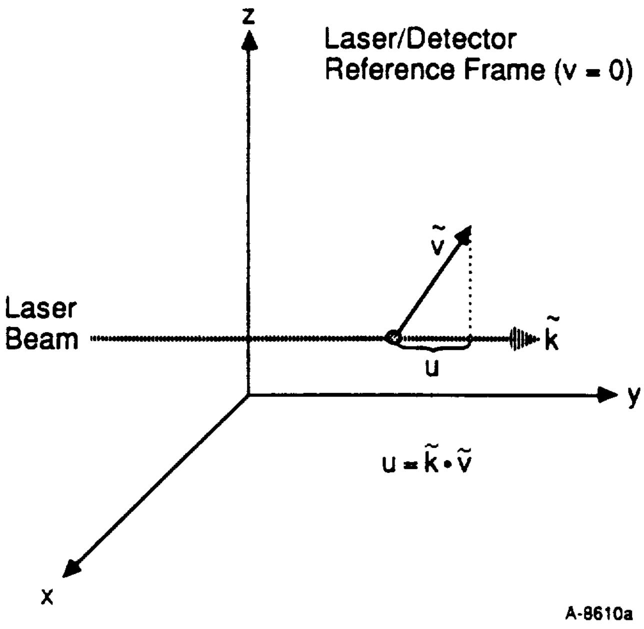

Figure 1. Schematic Illustration of the Geometry of the Linear Doppler-Shift

frame (the laboratory frame). The projection of the gas velocity vector onto the laser field wave vector is given by the scalar u.

The moving gas molecules experience an optical field which is Doppler-shifted relative to an ensemble of stationary molecules. To first order, the magnitude of this Doppler-shift is given by

$$\omega_v = \omega_0 \left[1 \pm \frac{u}{c} \right] \tag{2}$$

where ω_0 is the zero-velocity absorption frequency and c is the velocity of light. Higher order terms due to the relativistic Doppler effect are on the order of $(u/c)^2$ and may be neglected for practical terrestrial velocities.

The most direct measure of the magnitude of the Doppler-shift is made by scanning a laser wavelength across an absorption lineshape and determining the shift of the lineshape with respect to a stationary lineshape. This approach was first suggested by Measures[5] and realized by Zimmerman and Miles.[6] A drawback to this approach, however, is the time required to complete a stable scan of the lineshape. Recently, a modified ring-dye laser has been scanned across OH fluorescence lineshapes in a supersonic reacting flow with an effective time resolution of approximately 1 ms.[7] Using a pulsed-dye amplifier, this approach has been extended to an imaging configuration. As reported in Section 5, we also used this technique to determine the centerline variation of the mean jet velocity in the demonstration burner.

Examination of Eq. (1) reveals that the scanned approach is, in principle, unnecessary. Since the magnitude of the excitation efficiency overlap integral depends on the relative frequency between the laser spectral intensity lineshape and the molecular absorption lineshape, it should be possible to infer the relative velocity by a simple measure of the strength of the fluorescence signal, provided that the lineshapes of the laser and absorber are accurately known. Of course, the fluorescence signal must be normalized to account for variations in absorber number density, fluorescence efficiency, etc. This latter approach is the subject of the present program. It offers the advantage of improved time resolution and the ability to generalize the measurement concept to single-shot, multi-point measurements using laser sheet excitation and intensified detector array fluorescence imaging.

The form of the algorithm derived to determine the flow velocity from single-wavelength LIF measurements depends primarily on two criteria:

1. The dimensionality of the velocity field
2. The relative magnitude of the laser spectral bandwidth ($\Delta\omega_L$) and the molecular absorption bandwidth ($\Delta\omega_A$).

We begin with a discussion of the simplest case of a one dimensional flowfield. Although not strictly required, it is useful pedagogically to first assume that optical access is available both along the flow direction (velocity sensitive) and perpendicular to the flow direction (no velocity sensitivity). This experimental arrangement is illustrated in Figure 2.

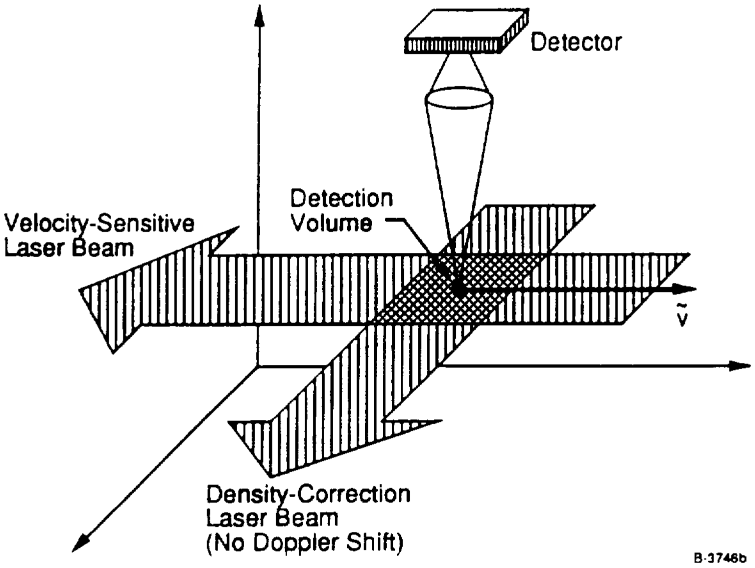
Detector
Detection Volume
Velocity-Sensitive Laser Beam
$\tilde{v}$
Density-Correction Laser Beam (No Doppler Shift)
B-3746b

Figure 2. Schematic Diagram of Optical Access for One-Dimensional Flow Measurements

The magnitude of the fluorescence signal determined by the laser beam crossing the flow axis is denoted by S_{F1} where

$$S_{F1} \sim \int I_{(\omega)} g_{(\omega)} d\omega \quad . \tag{3}$$

Similarly, the magnitude of the fluorescence from the laser beam propagating along the flow axis is given by

$$S_{F2} \sim \int I_{(\omega)} g_{(\omega - \omega_v)} d\omega \tag{4}$$

where ω_v is the Doppler-shifted frequency given by Eq. (2).

In order to derive simple, closed-form expressions for the velocity as a function of the fluorescence signal, it is necessary to make some assumptions regarding the relative width of the laser spectral bandwidth and the molecular absorption lineshape, $g_{(\omega)}$. Heuristically, it is convenient to first assume that the laser spectral bandwidth is much smaller than the molecular absorption lineshape. This is schematically illustrated in Figure 3, which shows the two functions plotted against frequency. The magnitude of the overlap integral is indicated by the hatched region.

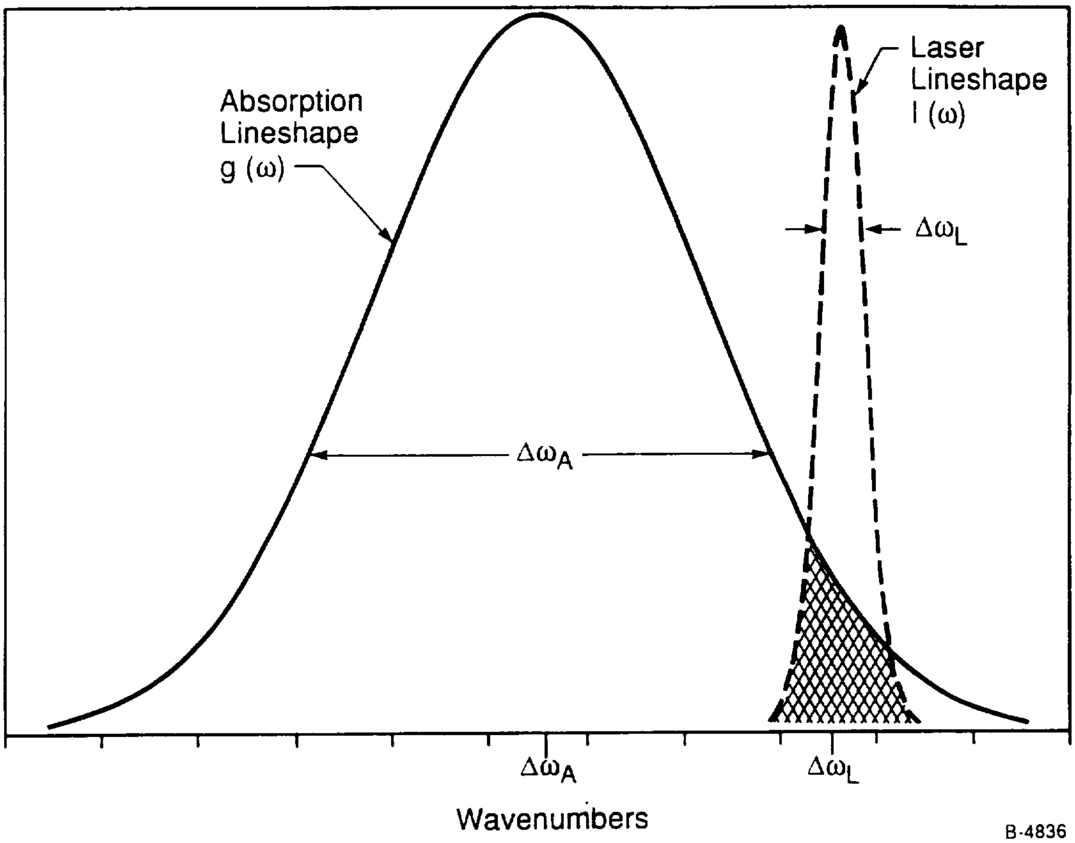

Figure 3. Molecular Absorption Lineshape and Laser Spectral Bandwidth Overlap for a Narrow-Bandwidth Laser

In this limit, we may replace the laser spectral bandwidth with a delta-function in frequency and write

$$I_{(\omega)} \cong I\delta_{(\omega_L)} \tag{5}$$

where: ω_L = laser line-center frequency

and the normalization of the delta function is such that

$$\int I\delta_{(\omega_L)} d\omega = I \quad . \tag{6}$$

Substituting Eq. (5) into Eqs. (3) and (4) gives

$$S_{F1} = I\ g_{(\omega_L)} \tag{7}$$

and

$$S_{(F2)} = I\ g_{(\omega_L - \omega_v)} \quad . \tag{8}$$

Expanding the velocity-shifted lineshape function, $g(\omega_L - \omega_v)$, in a Taylor Series about ω_L and retaining only the linear term gives

$$g_{(\omega_L - \omega_v)} = g_{(\omega_L)} + \frac{\partial g}{\partial \omega}(\omega_L - \omega_v) \quad . \tag{9}$$

Using Eq. (9) to replace the Doppler-shifted lineshape function in Eq. (8) yields the following form for the fluorescence ratio:

$$\frac{S_{F2}}{S_{F1}} = 1 + \frac{\left.\frac{\partial g}{\partial \omega}\right|_{\omega_L}}{g_{(\omega_L)}}(\omega_L - \omega_v) \quad . \tag{10}$$

Substituting for the doppler-shifted frequency, ω_v, and inverting yields the following expression for the flow velocity as a function of the fluorescence ratio:

$$V = \frac{c}{\omega_L}\left(1 - \frac{S_{F2}}{S_{F1}}\right)\frac{g(\omega_L)}{\left.\frac{\partial g}{\partial \omega}\right|_{\omega_L}} \quad . \tag{11}$$

In this case, the velocity algorithm is sensitive to the inverse of the slope of the molecular absorption lineshape normalized by the magnitude of the lineshape. As discussed above, these quantities are sensitive to the local temperature and pressure, depending on the exact frequency of the laser relative to the molecular lineshape center frequency. This basic approach was used by Hiller, et al.[9-11] in the early LIF velocimetry literature. Their approach was to seed the flow with molecular iodine and probe the fluorescence using a frequency modulated Ar^+ laser.

In their work, the sensitivity of the molecular absorption lineshape proved a barrier to quantitative measurements. It was necessary to use two separate laser wavelengths (derived from acousto-optic modulation of the Ar^+ frequency) in order to make a two-point estimate of the slope of the lineshape. Specific laser excitation frequencies were chosen in order to minimize the pressure and temperature sensitivity of this two-point slope estimate. Because the algorithm depended only on the linear term of the linewidth expansion, it was necessary to restrict the range of velocity shifts such that the range of frequencies fell within the linear slope of the molecular absorption lineshape.

The opposite limiting case is found when the laser spectral bandwidth is much larger than the molecular absorption lineshape, schematically illustrated in Figure 4. In this limit, the molecular absorption lineshape is expressed in terms of a delta-function

$$g_{(\omega)} \cong g\delta_{(\omega_A)} \tag{12}$$

where: $\omega_A \equiv$ absorption line-center.

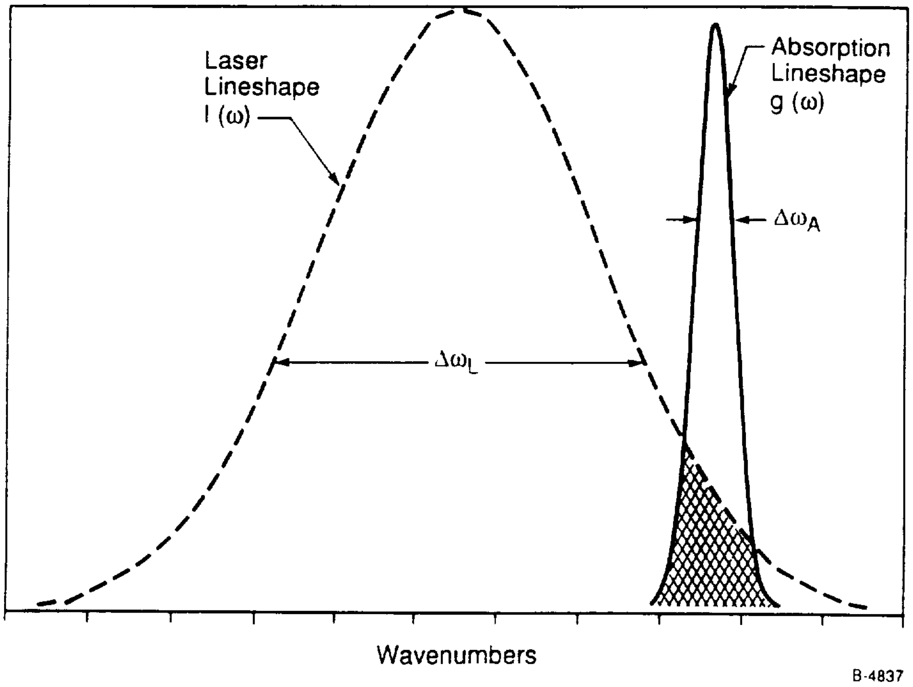

Figure 4. Molecular Absorption Lineshape and Laser Spectral Bandwidth for a Broad-Bandwidth Laser

By expanding the laser lineshape in a Taylor Series and following the same procedure as before, the following expression is derived:

$$V = \frac{c}{\omega_A}\left(1 - \frac{S_{F2}}{S_{F1}}\right)\frac{I_{(\omega_A)}}{\left.\frac{\partial I}{\partial \omega}\right|_{\omega_A}} \quad . \tag{13}$$

Equation (13) is analogous to Eq. (11) except that the normalized lineshape in the algorithm is now the laser lineshape rather than the molecular absorption lineshape. This is convenient since the algorithm is now independent of flow temperature and pressure fluctuations and is only a function of the laser spectral properties. This approach was used by Paul et al.,[12] to measure the velocity distribution in a cold, supersonic jet seeded with NO. In this case, the low temperature and pressure of the flow collapsed the absorption lineshape and a broadband pulsed dye laser was used to excite the fluorescence. This approach has also been recently pursued in hot, low-pressure jets of NO and Ar.[13]

While an attractive approach for low pressure, low temperature flowfields, the broadband laser limit is generally not achievable with commercially available pulsed dye lasers in applications near atmospheric pressure. As detailed in Section 3, most pulsed dye lasers operate with spectral bandwidths (without intracavity etalons for bandwidth narrowing) between 0.1 cm^{-1} and 0.4 cm^{-1} when frequency-doubled into the UV. By comparison, typical OH linewidths near atmospheric pressure and 2000 K are 0.3 cm^{-1}. Hence, neither limiting condition described above can apply.

In the intermediate case, illustrated in Figure 5, there is not a simple, closed form expression for the velocity as a function of the ratio of the fluorescence signals. Rather, we define an implicit velocity algorithm, $\psi_{(v)}$, as follows:

$$\psi_{(v)} = \frac{\int I_{(\omega)} g_{(\omega+\omega_v)} d\omega - \int I_{(\omega)} g_{(\omega-\omega_v)} d\omega}{\int I_{(\omega)} g_{(\omega+\omega_v)} d\omega + \int I_{(\omega)} g_{(\omega-\omega_v)} d\omega} \quad . \tag{14}$$

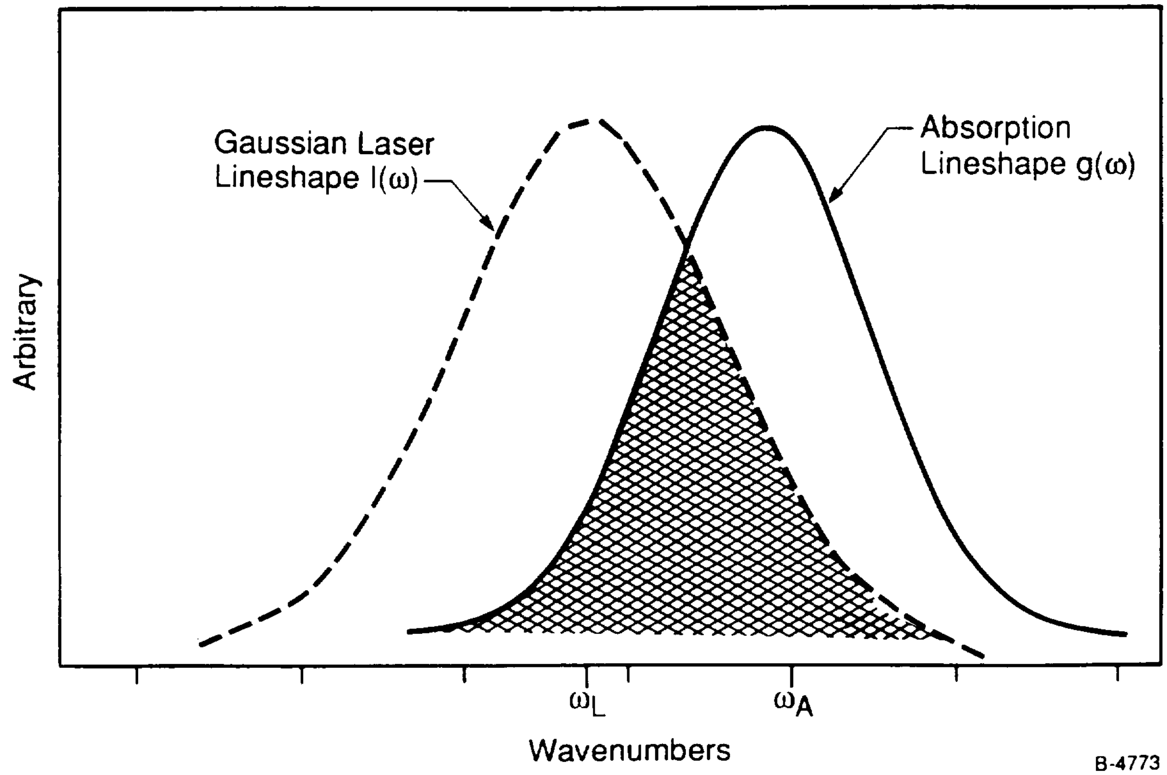

Figure 5. Molecular Absorption Lineshape and Laser Spectral Bandwidth Overlap for Equivalent Bandwidths

We now generalize our basic approach to the case of non-directed flows. As pointed out by Hiller,[11] it is not necessary that one of the fluorescence measurements be directed across the flow with no Doppler-shift. Using counter-propagating beams, up-shifted and down-shifted by the same magnitude, it is possible to derive similar velocity expressions. We denote the up-shifted values as S_{F+} and the down-shifted values as S_{F-}. For the case of the narrow-bandwidth laser, the form of the velocity algorithm derived according to the procedure described above is

$$V = \frac{c}{\omega_L}\left[\frac{2S_{F^+}}{S_{F^+} + S_{F^-}} - 1\right]\frac{g_{(\omega_L)}}{\left.\frac{\partial g}{\partial \omega}\right|_{\omega_L}} \quad . \tag{15}$$

Similarly, for the broad-bandwidth laser, the form of the algorithm is

$$V = \frac{c}{\omega_L}\left[\frac{2S_{F^+}}{S_{F^+} + S_{F^-}} - 1\right]\frac{I_{(\omega_A)}}{\left.\frac{\partial I}{\partial \omega}\right|_{\omega_A}} \quad . \tag{16}$$

In each case, it is only the premultiplier of the normalized slope which is different from the expressions derived from the directed flow cases. Hence, it is possible to determine a single component of the velocity field with optical access at an arbitrary angle to the field. The component so derived will always be aligned with the counter-propagating beam paths.

In the intermediate case, again, no simplification of the overlap integral is possible and the form of the velocity algorithm is given by

$$\psi_{(v)} = \frac{\int I_{(\omega)} g_{(\omega+\omega_v)} d\omega - \int I_{(\omega)} g_{(\omega-\omega_v)} d\omega}{\int I_{(\omega)} g_{(\omega+\omega_v)} d\omega + \int I_{(\omega)} g_{(\omega-\omega_v)} d\omega} \quad . \tag{17}$$

Using Eqs. (3) and (4), Eq. (17) may be manipulated into the following form:

$$\psi_{(v)} = \frac{2S_{F^+}}{S_{F^+} + S_{F^-}} - 1 = \frac{2S_{F^+}}{S_{F\pm}} - 1 \tag{18}$$

where $S_{F\pm} = S_{F+} + S_{F-}$. For a PLIF experiment, this form is preferred since one camera measures only S_{F+} while the second camera integrates both S_{F+} and S_{F-}. The advantage of this is obvious if one considers that the signal noise, σS_F, will be dominated by signal shot-noise which is given by

$$\sigma S_F = (\eta S_F)^{1/2} \tag{19}$$

where η is the detector quantum efficiency. Hence the signal-to-noise ratio is

$$\frac{S_F}{\sigma S_F} = (\eta S_F)^{1/2} \quad . \tag{20}$$

Thus integrating both S_{F+} and S_{F-} on the same detector ameliorates the low signal to noise ratio inherent in the S_{F-} image alone.

From error propagation theory, the uncertainty in the velocity algorithm is related to the uncertainty in the measured quantitites according to the equation

$$\sigma\psi^2 = \left[\frac{\partial\psi}{\partial S_{F+}}\right]^2 \sigma S_F^2 + \left[\frac{\partial\psi}{\partial S_{F\pm}}\right]^2 \sigma S_{F\pm}^2 \quad . \tag{21}$$

Performing the substitution for the partial derivatives and manipulating the result algebraically, we have

$$\frac{\sigma\psi}{\psi} = \frac{2}{S_{F\pm}(2S_{F+} - S_{F\pm})}\left\{(S_{F\pm}\sigma S_{F+})^2 + (S_{F+}\sigma S_{F\pm}^2)\right\}^{1/2} \quad . \tag{22}$$

The actual detected signal is the number of incident photons, S_F, multiplied by the detector quantum efficiency, η. Substituting this and the expression in Eq. (20) for the shot-noise limited uncertainty in each signal, we have the following equation for the velocity algorithm uncertainty due to the signal uncertainty:

$$\frac{\sigma\psi}{\psi} = \frac{2}{(2S_{F+} - S_{F\pm})}\left\{\frac{S_{F+}}{S_{F\pm}}\left[\frac{S_{F\pm} + S_{F+}}{\eta}\right]\right\}^{1/2} \quad . \tag{23}$$

Equation (23) shows that the fractional uncertainty in the algorithm approaches infinity as $S_{F\pm} \rightarrow 2S_{F+}$, or as the velocity approaches zero. The increased fractional uncertainty here is due to the problem in measuring small differences between large numbers in the presence of statistical noise.

Equation 18 is the basic form of the velocity algorithm used to reduce the PLIF images obtained in the experimental demonstrations. This section has illustrated how uncharacterized variations in the the absorption lineshape and laser lineshape may impact the velocity measurement accuracy. These effects were thoroughly analyzed in the Phase I portion of the program and motivated several key tasks of the Phase II program. In particular, direct measurements of the variation in the OH collisional broadening parameters were determined in H_2-air combustion gases at a variety of fuel/air stoichiometries. Direct measurements of single-pulse laser bandshapes were also obtained, demonstrating the need to modify the factory-configured laser cavity in order to gain control of the laser bandshape. These efforts are described in Sections 2 and 3 of this report.

2. OH COLLISIONAL BROADENING MEASUREMENTS

2.1 Lineshape Broadening Mechanisms

Transitions between real levels in atoms and molecules do not occur at only discrete frequencies, but over a narrow range of frequencies within the absorption lineshape. The functional form of this lineshape depends on the surrounding thermodynamic state of the gas. The first broadening mechanism we consider is the thermal broadening of the lineshape due to the random motion of the molecules in the gas. The translational energy associated with the molecules results in a Maxwellian velocity distribution. Each molecule traveling with a given random velocity experiences a slightly Doppler-shifted frequency of the exciting optical field. The ensemble effect of the Maxwellian velocity distribution gives rise to the so-called Doppler profile, expressed as:

$$g_{(\omega)} = 2\sqrt{\frac{\ln 2}{\pi}}\,\frac{1}{\Delta\omega_D}\exp\left[-4\ln 2\,\frac{(\omega-\omega_o)^2}{\Delta\omega_D^2}\right] \tag{24}$$

where: $\Delta\omega_D \equiv$ Doppler-width

and is given by

$$\Delta\omega_D = 2\left[\frac{2\ kT\ \ln 2}{mc^2}\right]^{1/2}\omega_o \tag{25}$$

$\omega_o \equiv$ frequency of the absorption line-center .

If Doppler-broadening were the only broadening mechanism of relevance, the lineshape would depend on a single parameter of the surrounding flowfield - the temperature.

Near atmospheric pressure, however, a second broadening mechanism is important. Collisions with neighboring molecules interrupt the coherent interaction of the molecule with the optical field and perturb the energy levels of the molecule, introducing the so-called Lorentzian lineshape

$$g_{(\omega)} = \frac{\Delta\omega_c}{2\pi(\omega-\omega_s)^2 + \frac{\pi}{2}\Delta\omega_c^2} \tag{26}$$

where ω_s is the shifted line center absorption frequency and $\Delta\omega_c$ is the collision-width. The collisional shift arises from the perturbation of the isolated molecular energy levels during the collision. It is typically expressed as a fraction of the collision width

$$\omega_s = \omega_o + \beta\Delta\omega_c \tag{27}$$

where β may be positive or negative, depending on the structure of the electronic orbitals of the colliding species.

The simultaneous action of both collisional and Doppler-broadening results is expressed as a convolution of the two profiles. The resultant expression is the well known Voigt profile

$$g_{(\omega)} = \left[\frac{mc^2}{2\pi kT}\right]^{1/2} \left[\frac{\Delta\omega_c}{2\pi\omega_o}\right] \int_{-\infty}^{\infty} \frac{\exp\left[\dfrac{-mc^2(\omega'-\omega_s)^2}{2kT\,\omega_o^2}\right]}{[(\omega-\omega_s) - (\omega'-\omega_s)]^2 + \left[\dfrac{\Delta\omega_c}{2}\right]^2} d\omega' \ . \qquad (28)$$

This is usually written in terms of the Voigt function

$$g_{(\omega)} = \frac{2\sqrt{\ln 2}}{\sqrt{\pi}\,\Delta\omega_D} V_{(\xi,a)} \qquad (29)$$

where:

$$V_{(\xi,a)} \equiv \frac{a}{\pi} \int \frac{\exp(-y^2)}{a^2 + (\xi - y)^2} dy \qquad (30)$$

and

$$\xi = 2\sqrt{\ln 2} \left[\frac{\omega - \omega_s}{\Delta\omega_D}\right]$$

$$y = 2\sqrt{\ln 2} \left[\frac{\omega' - \omega_s}{\Delta\omega_D}\right]$$

$$a = \sqrt{\ln 2} \left[\frac{\Delta\omega_c}{\Delta\omega_D}\right]$$

The Voigt "a-parameter" is thus a measure of the relative contribution of collisional and Doppler broadening to the absorption lineshape. Since the probability for transition integrated over the entire lineshape must remain unchanged in the presence of broadening mechanisms, the integral of the lineshape over all frequencies is equal to unity.

While the Doppler-width for a given transition is easily calculated, the collisional-width and -shift are more problematic. Physically, the width is simply proportional to the rate of broadening collisions. As such, it is dependent on the composition of the surrounding gas, the overall gas pressure, and temperature. The pressure dependence is usually separated by expressing the collision width as

$$\Delta\omega_c = \sum_i 2\gamma_{i(T)} P_i \qquad (31)$$

where γ_i is the collision broadening parameter for species i, P_i is the partial pressure of species i, and the summation is over all available collision partners. The temperature dependent collisional broadening parameter may vary with the particular transition involved, as well as the surrounding gas.

Measurements of the rotational level dependence of OH collision broadening have been reported in room temperature gases,[14-16] shock-heated high temperature gases,[17] and flames.[18,19] All of these results were obtained from probing the (0,0) vibrational band transitions near 308 nm. The fluorescence strategy pursued in this and most combustion applications, however, uses (1,0) band excitation near 283 nm, followed by detection of emission from both the (1,1) and (0,0) bands. The collision-induced energy transfer behavior of individual rotational levels in $v' = 1$ is measurably different from corresponding J'-levels in $v' = 0$, and suggests that deviations in the broadening behavior of these transitions might be expected. For example, the cross-section for total rate of removal from $v' = 1$ is greater for both N_2 and CO_2 than the analogous processes in $v' = 0$.[20] Since collsions with neighboring molecules effectively determines the lifetime of the upper state, and the collisional lifetime for $v' = 1$ is as much as 50 percent shorter than that of $v' = 0$, we made the first direct experimental determinations of the collisional broadening and shifting behavior of OH (1,0) band transitions. The measurements were made in H_2- air combustion gases, thereby allowing the results to be used to predict the potential variation in the collision width across a range of fuel-air stoichiometries expected in a typical H_2-fueld SCRAMJET combustor.

2.2 Experimental Determination of OH (1,0) Band Collision Broadening and Shifting Parameters

The experiments were conducted in the post-combustion gases above a flat-flame burner. A schematic of the burner assembly is shown in Figure 6. The burner consists of three separate manifolds. Fuel is introduced into one manifold and then flows through an array of small stainless steel tubes which are threaded through alternate cells of the honeycomb burner surface. Oxidizer gas (in the present study, selectable mixtures of N_2 and O_2) is introduced into a second manifold and flows around the fuel tube array through the remaining cells of the honeycomb in the center 1 in. square. The fuel and the oxidizer rapidly mix above the honeycomb forming an array of blended diffusion-like flamelets which quickly mix into a uniform post-combustion gas as if from a pre-mixed flat flame burner. The diffusion character of the fuel-air

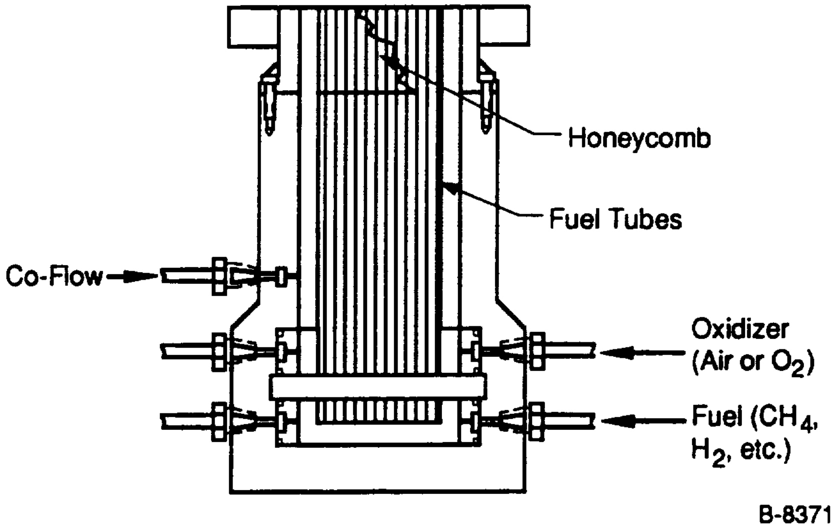

Figure 6. Schematic Diagram of Flat Flame Burner

mixing stabilizes the flame above the burner surface rather than on the surface itself and permits high gas temperatures without burner cooling. It is possible to operate this burner with H_2 fuel and pure O_2 oxidizer.

A third manifold is provided for a co-flowing gas that flows through the honeycomb around the central burner section in a 1/4 in. shroud. This shroud flow stabilizes the combustion gas interface with the surrounding air by eliminating the surrounding shear layer. Furthermore, it prohibits diffusion of room air into the combustion gases near the burner, thereby ensuring that desired fuel/air stoichiometries may be maintained for some distance downstream of the burner surface (typically ~ 10 cm). For our work, this shroud flow consisted of pure N_2.

Examples of temperature profiles across the burner with a methane-air flame are shown in Figure 7. The figure shows thermocouple traces across the full burner width at various heights up to 2.46 cm. The flatness of the temperature traces indicates the homogeneity of the flame. Evidence that the gases above the burner are in equilibrium is shown in Figure 8, a plot of the centerline temperature 1.4 cm above the burner surface as a function of equivalence ratio for a methane-air flame. In this data set, the flow rates have been adjusted to maintain a constant overall gas flow rate for the various fuel/air mixtures. As expected, the centerline temperature peaks at stoichiometric conditions.

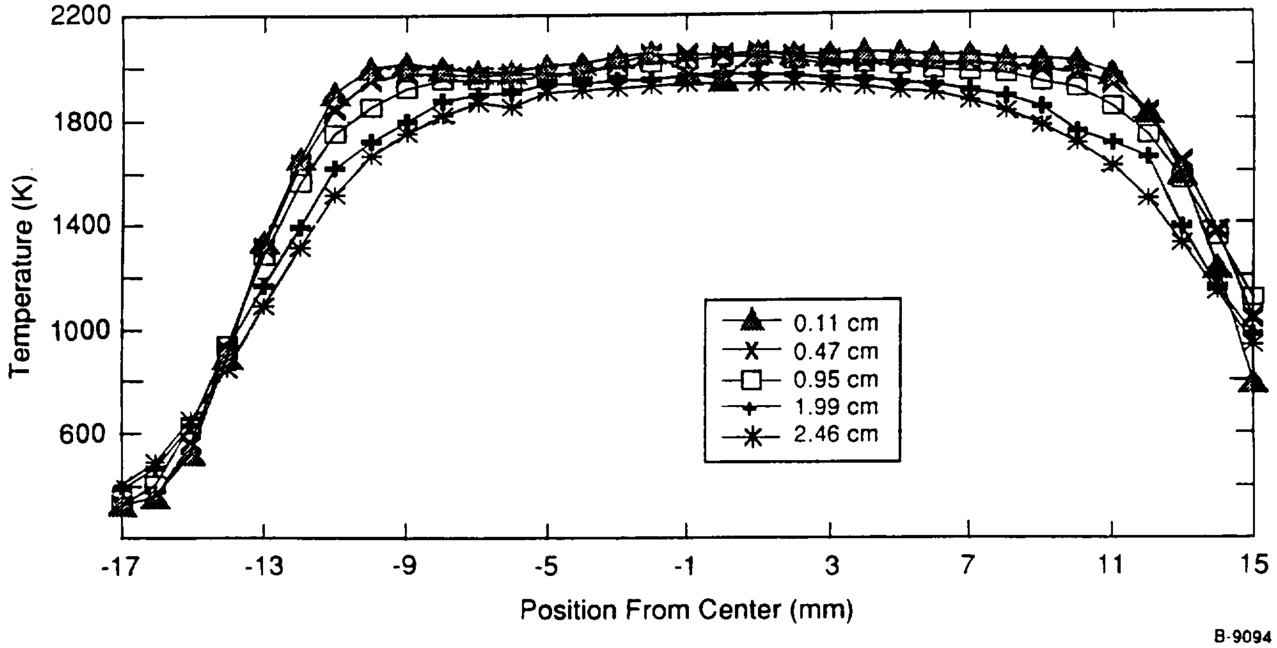

Figure 7. Temperature Profiles Above Flat Flame Burner

Simultaneous absorption and laser-induced fluorescence measurements were made using the experimental setup shown in Figure 9. A Coherent model 699-05 ring dye laser, pumped by a Coherent model INNOVA 100-20 Ar^+ laser, was intra-cavity frequency doubled with a KDP crystal to generate 1 to 3 mW of UV laser radiation near 285 nm. Narrow bandwidth, single axial mode operation is achieved in the travelling wave laser cavity with several intra-cavity spectral filtering elements. The time-averaged bandwidth of the single mode dye laser was about 60 MHz in the visible. Wavelength scanning over a 60 GHz range in the UV was achieved by synchronous tuning of the intra-cavity spectral selective elements. The frequency-doubled laser linewidth was on the order of 100 MHz. This was approximately 100 times smaller than the typical OH absorption linewidth in atmospheric pressure flame environments, so that instrumental broadening of the lineshapes recorded while scanning the dye laser wavelength was negligible.

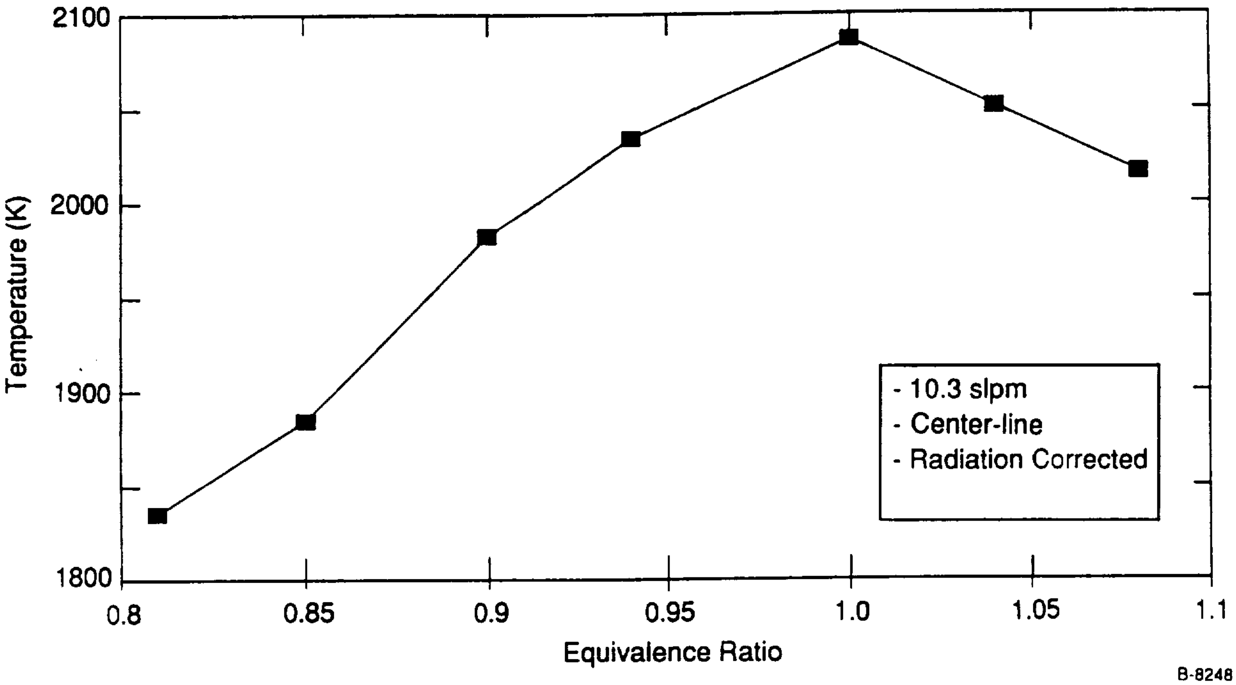

Figure 8. Centerline Temperature as a Function of Equivalence Ratio for Methane-Air Mixtures

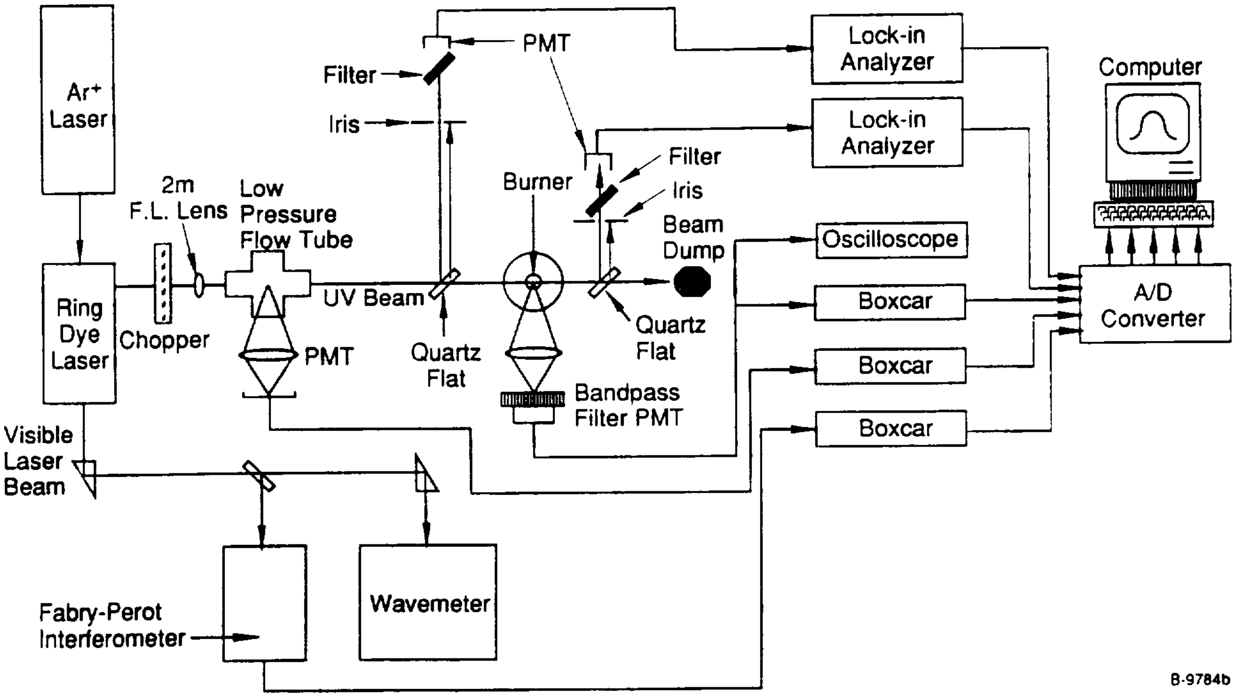
Ar+ Laser
2m F.L. Lens
Low Pressure Flow Tube
Filter
Iris
PMT
Burner
Filter
Iris
Beam Dump
Lock-in Analyzer
Lock-in Analyzer
Computer
Oscilloscope
Boxcar
Boxcar
Boxcar
A/D Converter
Ring Dye Laser
Chopper
UV Beam
PMT
Quartz Flat
Quartz Flat
Bandpass Filter PMT
Visible Laser Beam
Fabry-Perot Interferometer
Wavemeter
B-9784b

Figure 9. Experimental Setup for OH Collisional Broadening Measurements

Residual visible laser radiation was outcoupled from the dye laser and used to monitor the scanning behavior of the laser. A portion of the beam was directed into a Burleigh model WA-20VIS wavemeter to determine the wavelength. The accuracy of the wavemeter (one part in 10^6) was sufficient for determining the identity of the probed transition. The remainder of the visible beam was injected into a Burleigh RC-140 Fabry-Perot interferometer. The interferometer provided a continuous recording of both the laser frequency and dye laser mode behavior during a scan. Transmission through the interferometer was detected with a photodiode, whose output voltage was processed with an SRS Model 250 boxcar signal averager.

The UV laser beam was passed through an EG&G model 192 light chopper, typically operated at 4 kHz, and a 2m focal length quartz lens. A reference signal from the light chopper was used to synchronously trigger the lock-in amplifiers and boxcar averagers of the various detection channels. The position of the focussing lens was adjusted to focus the laser beam beyond the burner. The UV beam first passed through a low-pressure (~ 1 torr) discharge flow reactor source of OH. The flow reactor was used to record OH fluorescence in a collision-free environment with respect to the OH(A) radiative lifetime. Consequently, the energy levels were relatively unperturbed and the lineshape was free from broadening and shifting effects. By simultaneously recording the low pressure fluorescence lineshape and the collision-broadened absorption lineshape in the flame, the absolute collisional shift of the absorption lineshape center frequency was measured.

Figure 10 is a detailed schematic of the flow reactor source. The reactor was constructed from a 2.54 cm diameter Pyrex tube connected to a 2.54 cm diameter aluminum block. The Pyrex tube was coated with halocarbon wax and the detection block was coated with Teflon (Dupont Poly TFE #852-201). The various parts of the apparatus were connected using Viton O-ring joints, making the setup adaptable to many experimental configurations. The reactor was evacuated with a rotary pump, sustaining flow velocities up to 1000 cm/s at a total pressure of 2 torr. Flow rates of all reactants were measured using calibrated Teledyne Hastings-Raydist ST-series mass flow meters.

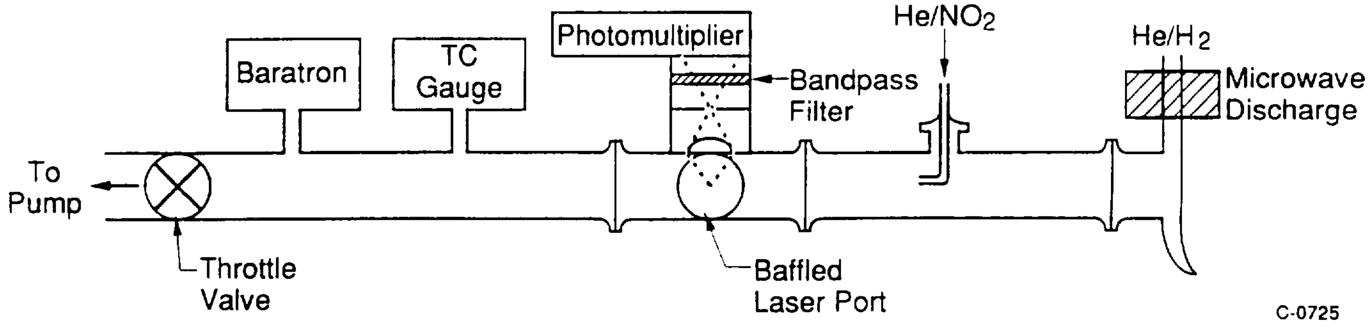

Figure 10. Low-Pressure Discharge OH Source

The OH in the low pressure reactor was generated at 300 K from the reaction

$$H + NO_2 \rightarrow OH + NO \quad . \tag{32}$$

The H atoms were produced using a McCarrol cavity operating at 2.54 GHz to discharge a mixture of 5% H_2 in helium. The H atoms were mixed with a flow of 5% NO_2 in helium at a total pressure of 2 torr. The OH concentration was estimated from measured H_2 mass flow rates to be 5×10^{12} cm^{-3} and the gas temperature of 300 K was determined by the Doppler-width of the fully resolved fluorescence lineshape.

The UV laser beam entered the flow tube detection block through quartz flats mounted at Brewster's angle and crossed the flow path at right angles through a series of skimmer-type optical baffles. Fluorescence was collected along the third perpendicular axis by an F/1.0 optical train, filtered using a 20 nm bandpass filter centered at 315 nm. A Hamamatsu R943-02 photomultiplier detected the fluorescence. The photocurrent was amplified by an Ithaco model 1642 current amplifier and processed by a synchronously-triggered boxcar signal averager (Stanford Research Systems model SR250).

After passing through the flow reactor, the UV beam was attenuated by an order of magnitude using a neutral density filter oriented at Brewster's angle. By attenuating the laser, we ensured that the laser intensity was within the linear regime of the photomultipliers. The beam then passes through a 6 mm thick UV flat and the front surface reflection is directed through a frosted Schott color glass UG-11 filter placed at an angle in front of a Hamamatsu R955 photomultiplier. Frosting each surface of the Schott glass filter and tilting it at an angle with respect to the incident laser beam reduces spurious etaloning effects in the reference intensity detection arm as the laser wavelength is scanned. Etaloning effects were a limiting artifact in the baseline linearity of the absorption lineshape measurement and great care was taken to reduce their effect on the ratio of the reference signal to the absorption signal. The rear surface reflection from the beam splitter was blocked by an aperture stop placed in front of the filter. The photomultiplier photocurrent was processed with an EG&G PAR lock-in amplifier.

The remaining UV light passing through the 6 mm beam splitter was directed across the centerline of the flat flame burner and onto a second 6 mm quartz flat. The front surface reflection from this flat was directed to a second detection channel, identical in setup to the reference intensity arm. Both photomultipliers were place equidistant from the 2m focussing lens and use of the double-beam splitter ensured that the light intensity in each channel was comparable. This setup also reduced the effect of relative etaloning and beam walkoff in the two detection channels. The bias voltage of the photomultipliers was adjusted to yield similar photocurrents when the laser wavelength was adjusted between OH absorption features.

Initially, we used a fourth detection channel to permit simultaneous OH fluorescence and absorption measurements in the combustion gases above the flat flame burner. However, OH(A) emission from the flame produced unacceptably large noise levels on the fluorescence lineshape. In practice, the signal to noise in this channel was insufficient to permit extraction of some collisional broadening parameters. We only used it to verify that the overall lineshape of the fluorescence and absorption lineshapes were the same. This verification eliminated our concern of possible effects on the absorption lineshape from non-uniformities in the gas conditions along the laser beam propagation path.

The first goal of our experimental approach was to make repeated measurements of an isolated lineshape at the same flame conditions so that a statistically significant estimate of our experimental uncertainty could be made. Figure 11 shows an example $P_1(6.5)$ lineshape taken in a stoichiometric ($\phi = 1.0$) H_2-air flame. The postflame gas temperature, measured at 1 cm above the burner surface using a radiation corrected thermocouple, was 2050 K. The solid line is the experimental absorption lineshape and the dashed line is a Voigt lineshape fit to the data. The lower curve is the point by point residual difference between the fit and the experimental lineshape.

The fitting routine searched for the Voigt a-parameter which minimized the rms sum of the residual differences for a given temperature and line-center frequency. The symmetry of the residuals and their small magnitude over the entire lineshape suggests that the Voigt fit was satisfactory and the higher-order lineshape models are not required. Some drift in the experimental baseline is evident in Figure 11 and was a persistent experimental difficulty throughout these high precision experiments. Although the baseline drift was small,

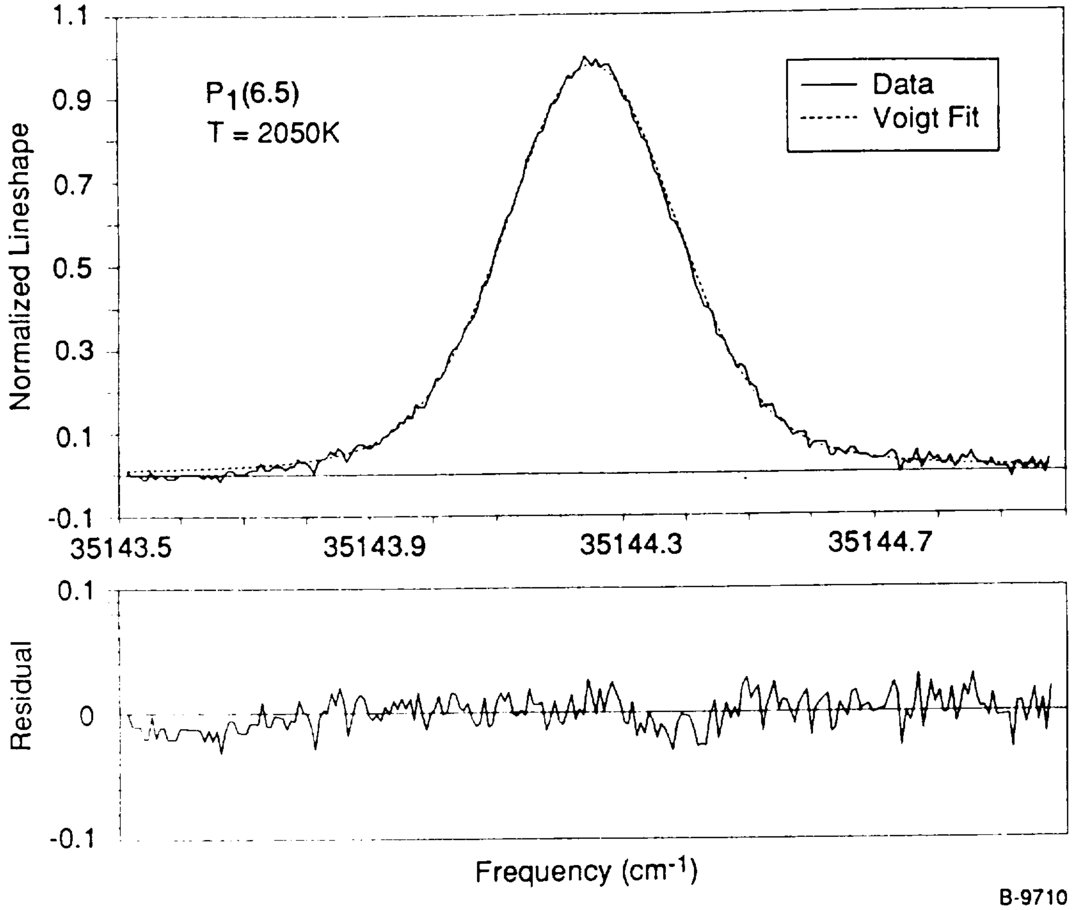

Figure 11. OH (1,0) Band $P_1(6.5)$ Lineshape. Solid line is experimental data; dashed line is Voigt fit. Bottom curve is residual difference between fit and data. For this data, T = 2050 K, a = 0.244.

about 1% of the maximum signal, it was most pronounced in the wings of the lineshape where the sensitivity to collisional effects is highest. We attribute the drift to small etaloning effects in the optical setup which is a typical limitation in measurements of weak absorption features.

After numerous improvements to the experimental setup to reduce baseline drifts in the measured lineshapes, nineteen separate measurements of this lineshape were made in two separate experiments resulting in an average a parameter of $a = 0.22 \pm 0.03$. From the Voigt a parameter and the gas temperature of 2050 K, we calculate a collision width for this experiment of $\Delta\omega_c = 0.073 \pm 0.008$ cm^{-1}. The uncertainty in the a parameter and the collision width is limited by the accuracy of the baseline correction. The collision width is a collective measurement of the effects of OH collisions with the ensemble of available partners in the postflame gases. Experimental data on the collisional behavior of (0,0) band transitions has been reported for individual collision partners such as H_2O, CO_2, and N_2.[17,19] In order to compare our measurements to this data, we must consider the composition of the postflame gases.

Figure 12 shows the calculated equilibrium major species mole-fractions in the postflame gases as a function of fuel equivalence ratio. The calculations were made using the STANJAN chemical equilibrium routines. Figure 13 shows the calculated equilibrium OH concentration and adiabatic flame temperature obtained from the same routine. Also shown in Figure 13 are the experimentally determined temperatures, which show equilibrium behavior in the shape of the curve as well as thermal losses to the burner surface, reflected in an overall lowering of the gas temperature. Using the composition data from Figure 12, the

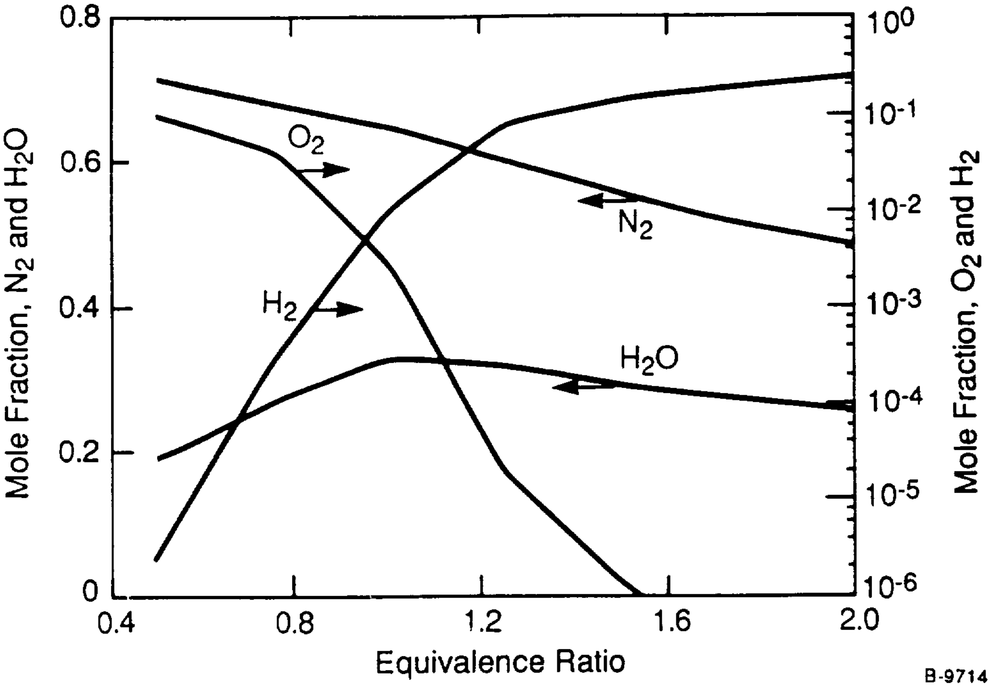

Figure 12. Equilibrium Major Species Distributions for H_2-Air Flames at Various Equivalence Ratios. Note that O_2 and H_2 mole-fractions are plotted against the log scale on the right ordinate of the figure, while N_2 and H_2O mole-fractions are plotted against the linear scale on the left ordinate of the figure.

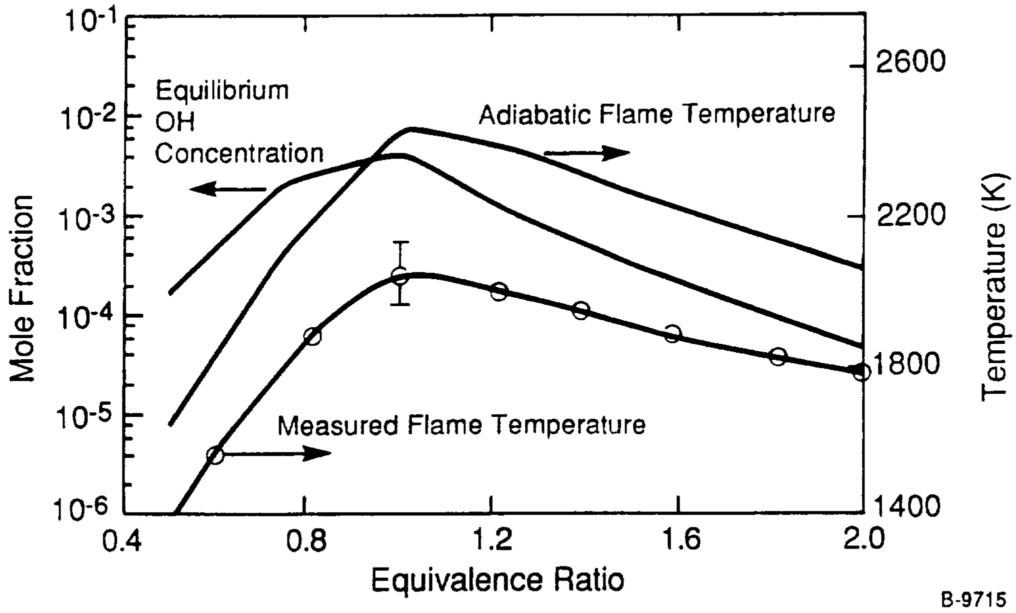

Figure 13. OH Mole-Fraction, Adiabatic Flame Temperature, and Measured Flame Temperature for H_2-Air Flames at Various Equivalence Ratios.

measured temperatures, and previously reported collisional broadening parameters for (0,0) band transitions[15-17], we can compare our measured collision widths to those obtained using (0,0) band data. For stoichiometric conditions, the equilibrium product gas is essentially 67% N_2 and 33% H_2O at 2050 K. This gas mixture and temperature corresponds to a (0,0) band collisional width (at this J") of $\Delta\omega_c = 0.073$, essentially the same as our (1,0) band measurement.

Figure 14 is a plot of measured (1,0) band collision widths in the stoichiometric H_2-air flame for several values of the lower state quantum number compared to the collision widths calculated from the (0,0) band data from references 1 and 2 at these conditions. The error bars in the (1,0) band data (shown as solid squares) represent the width of the standard deviation of the redundant measurements made on each transitions. The error bars in the (0,0) band data are taken from Refs. 15 and 17. The agreement between the data from the two bands is within the experimental uncertainty for all data points. It appears that the "knee" in the J-dependence (due principally to the H_2O contribution) seen in the (0,0) band is also present in the (1,0) band data.

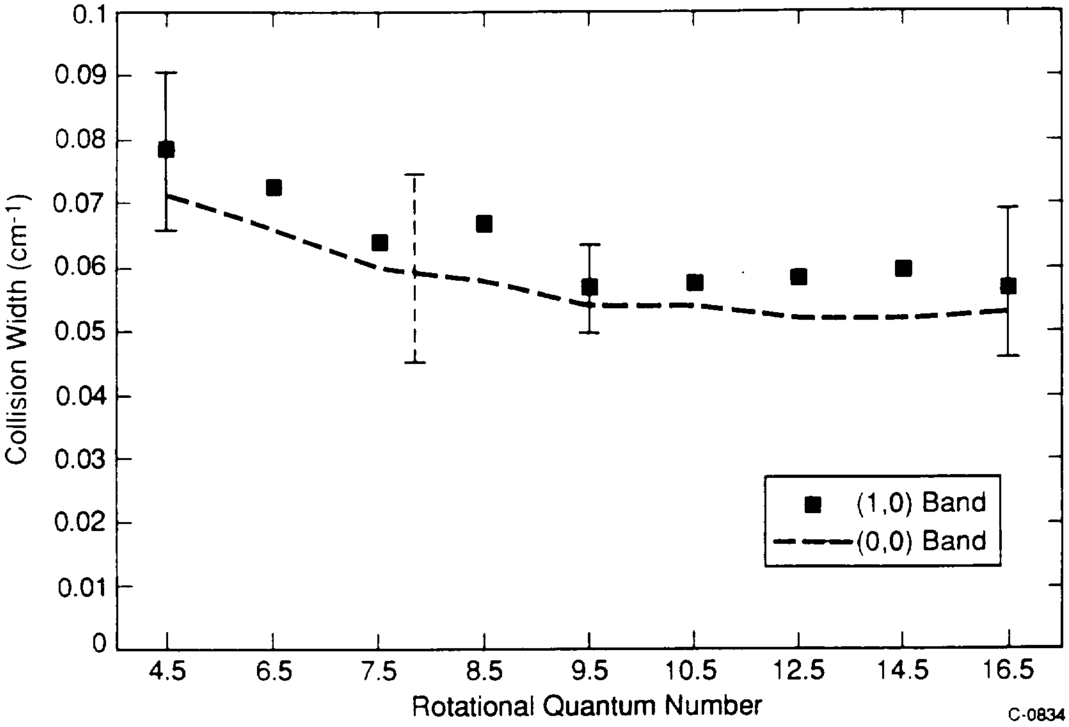

Figure 14. Collision Width of (1,0) Band Transitions of Varying Lower State Rotational Quantum Number for Stoichiometric H_2-air Flames: Comparison With (0,0) Band Transitions.

The overall agreement is somewhat surprising, particularly in view of the difference between the collisional interactions of the v′ = 1 level and the v′ = 0 level. In addition to rotational transfer and electronic quenching collisions, energy transfer pathways common to both levels, the v′ = 1 level also undergoes vibrational transfer collisions to the v′ = 0 level. This vibrational pathway proceeds with a rate approximately one-half of the electronic quenching rate, suggesting that the total collisional lifetime of the v′ = 1 level should be shorter. It is reasonable to expect, then, that the collisional width of the (1,0) band transitions might by measurably larger than those of the (0,0) band. That this is not the case highlights the difference in the nature of the molecular interactions associated with line-broadening collisions (which include inelastic as well as elastic collisions) and energy transfer collisions. Other implications of these results for energy transfer in OH A $^2\Sigma^+$ are discussed in the publication of this work (Ref. 21).

Because the OH velocimeter will be required to make measurements across a variety of stoichiometries, we also investigated the dependence of the (1,0) band transitions with flame equivalence ratio. Figure 15 is a plot of the collisional width of the $P_1(7.5)$ transition with flame equivalence ratio. Once, again, this collisional width reflects the combined action of all the available collisional partners in the gas - a mixture which is a strong function of the overall equivalence ratio. As discussed above, at an equivalence ratio of unity, the gas mixture is essentially water vapor and nitrogen. For equivalence ratios below unity, excess oxygen is present in the post flame gases. For equivalence ratios above unity, excess hydrogen is present. Collisional broadening behavior for (0,0) band transitions is not available for O_2 and H_2. Instead, the dashed line in Figure 15 is plot of the (0,0) band collision width calculated for each equilibrium gas mixture and temperature assuming that the H_2 collisional behavior is like that of H_2O and that the O_2 collisional behavior is like that of N_2. The agreement near unity equivalence ratio is again good, but the present study measures larger collisional linewidths further away from unity than predicted by this first order model. Most likely, this difference is due to somewhat larger broadening by H_2 and O_2 than predicted by analogy to H_2O and N_2. However, our measurements are pertinent for the present purposes and we can now bound the possible variation in the collisional linewidth across a PLIF image in a H_2-air diffusion flame.

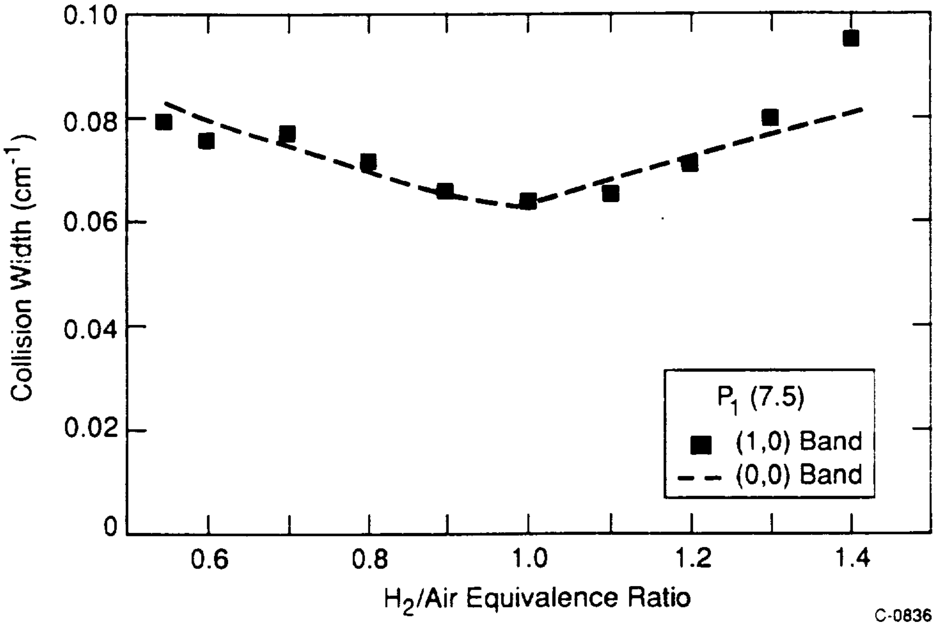

Figure 15. Collision Width of the $P_1(7.5)$ (1,0) Band Transition as Function of H_2-air Equivalence Ratio: Comparison With (0,0) Band Data.

The measured collsion-induced shift for J″ = 6.5 - 8.5 is summarized in Table 1, along with the standard deviation of the measurement ensemble, σ. Because the shift measurement accuracy is based on the accuracy of the line-center determination from the collisionless fluorescence measurement in the 300 K flow reactor, collisional shift data are only available for this range of J″ where sufficient population existed in both

Table 1. Collision-Induced Absorption Frequency Shift for OH(1,0)

Parmeter	$P_1(6.5)$	$P_1(7.5)$	$P_1(8.5)$
Shift (cm^{-1})	-0.008	-0.006	-0.008
σ (cm^{-1})	±0.001	±0.001	±0.004
ß	0.11	0.08	0.10

the low temperature and high temperature gases. Over this range, the collisional shift-to-width ratio is 0.1, in agreement with the measurement by Shirinzadeh, et al.,[16] using a (0,0) band transition.

In summary, this section reports the results of an experimental determination of the OH (1,0) band collisional broadening parameters in H_2-air combustion. These results are used to calculate the velocity algorithms presented in Subsection 1.2 which, in turn, are used to reduce the fluoresence ratio images to velocity. The velocity algorithm also depends on the form of the UV laser bandshape. The following section describes the experimental determination and modification of single-pulse UV laser bandshapes from a Lambda-Physik FL-3002 excimer-pumped dye laser.

3. PULSED DYE LASER BANDSHAPE MEASUREMENTS AND MODIFICATIONS

The programmatic goal of single-pulse velocity imaging requires an understanding of the single-pulse bandshape produced by commercially-available multi-mode pulsed dye lasers. Despite their profusion in laser-based flow diagnostics, little information was available in the literature or from the manufacturer regarding their spectral behavior. Since the velocity algorithms of the Phase I program depended sensitively on the assumptions regarding the laser bandwidth and the pulse-to-pulse bandwidth stability, we devoted a portion of the Phase II program to direct measurements of the single-pulse laser bandshapes.

3.1 Measurements of Single-Pulse Laser Bandshape

The experimental setup for the laser bandshape measurements is shown in Figure 16. A Lambda Physik FL3002 laser was pumped with a Questek 2080 excimer laser operating with XeF at 351 nm. The dye laser was operated with Coumarin 540A dye and tuned to ~565 nm, corresponding to the approximate visible wavelength employed for frequency doubling to the OH (1,0) band absorption transitions. The laser was aligned for maximum power with the frequency-doubling crystal in place. The crystal was then removed, without changing the overall dye laser alignment. This procedure ensured that the laser bandwidth measurements would be made at the optimum alignment where it will be used in the velocimetry application, namely, the maximum pulse energy in the UV.

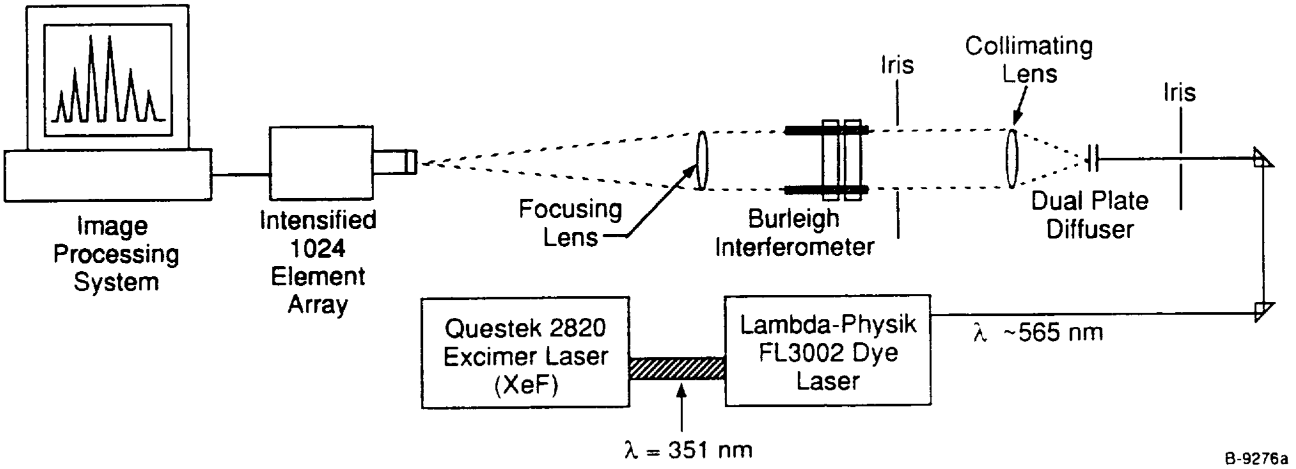

Figure 16. Experimental Setup for the Laser Bandshape Determinations

The laser beam was then spatially filtered with an iris to isolate the coherent beam from the low level of ASE and stray light co-propagating with it and directed onto a dual plate diffuser screen. The diffuser screens scrambled the spatial coherence of the beam and generated a quasi-uniform, nearly speckle-free plane of light. Light from this plane was collimated by a 4 in. focal length lens and directed through a Burleigh RC140 Fabry-Perot Interferometer. A second aperture was used to restrict the number of off-axis rays propagating through the system. The transmission interferogram was imaged onto an intensified linear photodiode array using a 1 m or 50 cm focal length lens, depending on the Free-Spectral Range (FSR) of the interferometer and the required frequency resolution.

For some of the time-averaged bandshape measurements, the linear array system was replaced with a 200 μm diameter pinhole and a photomultiplier tube. The mirrors of the Fabry-Perot were then piezoelectrically scanned and the transmission through the pinhole recorded, providing a measure of the average bandshape. This scanned-central-spot approach achieves the highest resolution for planar mirror interferometers.

Figure 17 is an example of the transmission recorded through the 200 μm pinhole as the Fabry-Perot mirrors were scanned over their 0.716 cm^{-1} free spectral range. For this experiment, a multi-mode HeNe laser was used as a means of establishing the resolving power of the instrument. With careful alignment, the individual cavity mode full-width at half-maximum (FWHM) was resolved to 0.0091 cm^{-1}, resulting in a calculated finesse (the ratio of the FSR to the minimum resolvable feature) of 79. With the alignment of the interferometer optimized, the FL-3002 pulsed dye laser beam was co-aligned with the HeNe beam and directed through the interferometer. Figure 18 is the recorded transmission from a interferometer mirror scan similar to that of Figure 17. The large spacing between peaks two and three is the result of the piezo-electric ramp voltage "flyback" and does not indicate a non-linearity in the mirror scan. The dye laser was operated at 565 nm and was pumped with 250 mJ from the XeF excimer laser. The dye laser pulse energy was approximately 25 mJ.

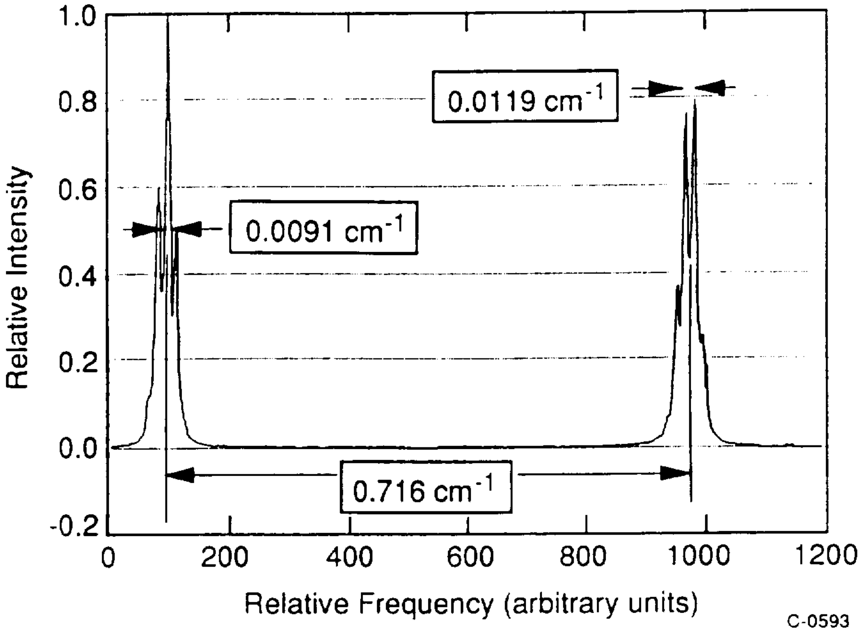

Figure 17. Average Bandshape of Multi-Mode HeNe Laser Showing Resolving Power of Interferometer

The dye laser was carefully aligned to achieve high pulse energy and the recorded average bandwidth was 0.15 cm^{-1}. Reducing the pump energy from 250 to 150 mJ resulted in a dye pulse energy reduction to 15 mJ and a somewhat narrower dye laser bandwidth, as shown in Figure 19. Here, the average laser bandwidth is 0.13 cm^{-1}. This behavior is probably due to a reduced number of laser cavity modes being pumped above threshold. Similar measurements were made with the laser tuned to 540 nm, the peak of the dye curve for Coumarin 540 dye. A slight increase in the averaged linewidth was noted, again probably due to a larger number of axial cavity modes above threshold. Observation of the interference pattern by eye suggested that the mean bandshapes recorded in Figures 18 and 17 reflected the average contribution from multiple laser modes which jittered slightly in frequency from pulse to pulse. Since the OH fluorescence measurements for the velocimeter will be made on a single pulse basis, it was important that we optimize the alignment of the interferometer for similar high resolution using the linear photodiode array detector.

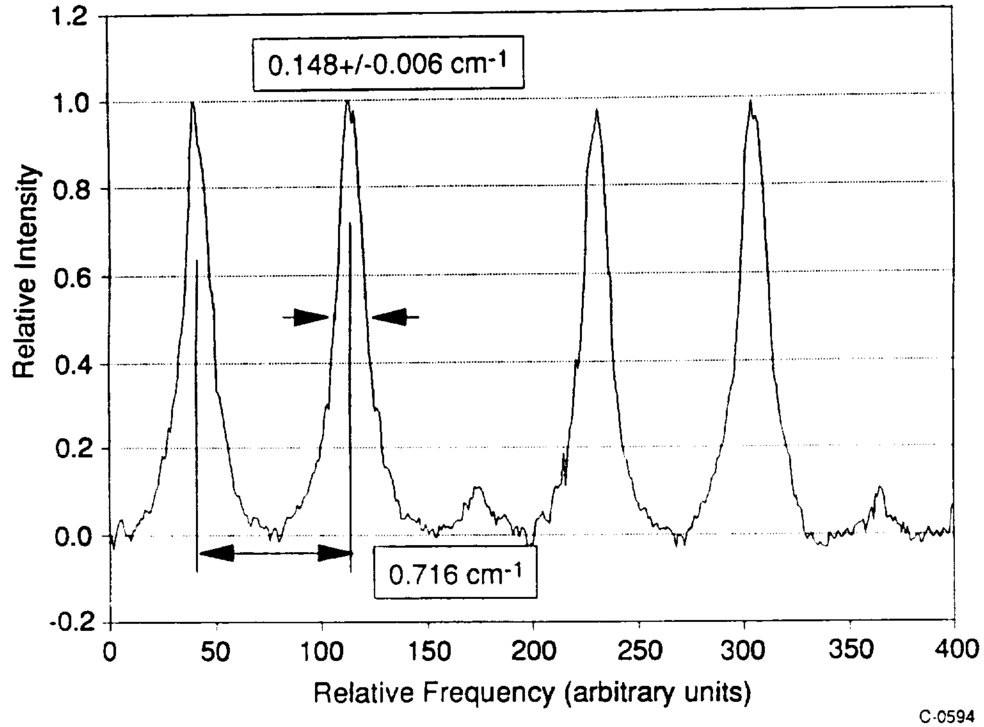

Figure 18. Average Bandwidth of FL-3002 Laser at 250 mJ Pump Energy

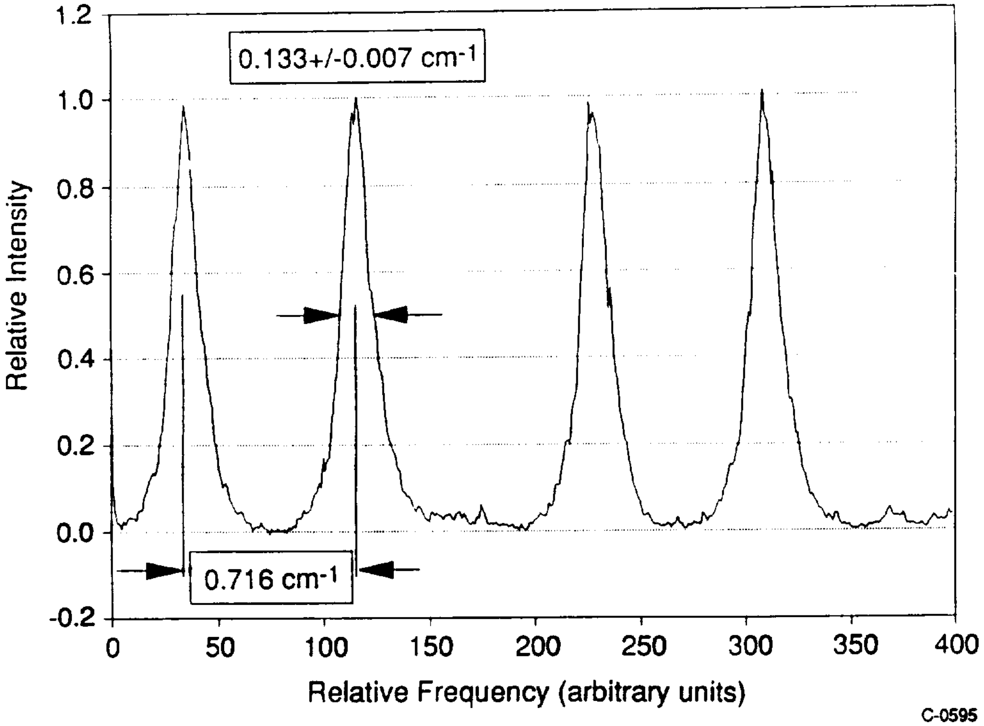

Figure 19. Average Bandwidth of FL-3002 Laser at 150 mJ Pump Energy

In general, imaging of the ringed interference pattern will always result in some reduction of resolution since the inherent finesse of the interferometer drops off from the central spot. After reducing the FSR of the interferometer to 0.242 cm^{-1}, we were able to record single pulse bandshapes such as those shown in Figure 20. The dashed and solid lines are the bandshapes corresponding to two separate laser pulses recorded at 565 nm with 250 mJ of pump energy and 25 mJ of dye laser energy. With the high spectral resolution provided by our improved detection scheme, a significantly more complicated bandshape emerges than that shown in Figures 18 and 19. The frequency spacing between the peaks in the solid curve is 0.017 cm^{-1} and corresponds to the axial cavity mode spacing of the laser, given by the formula

$$\Delta\omega_{cav} = \frac{1}{2L} \tag{33}$$

wh~re L is the cavity length.

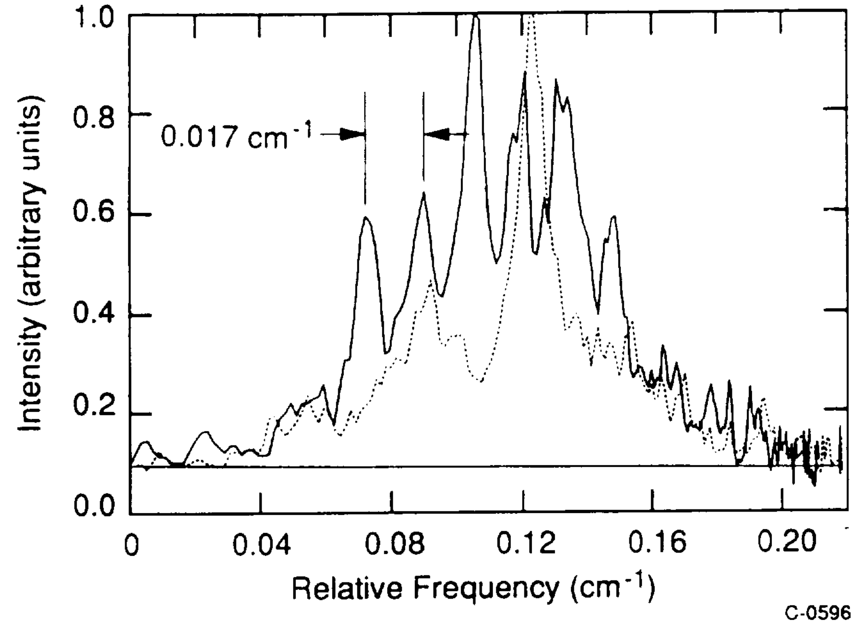

Figure 20. Single-Pulse Bandshapes of FL-3002 Laser With 250 mJ Pump Energy

In the solid curve, six cavity modes are lasing strongly above threshold. In the dashed curve, only two or three cavity modes are strongly lasing and the absolute frequency of the modes has shifted somewhat. It is important to note that it is this *singe-pulse* bandshape that, when frequency-doubled, gives rise to the single-pulse fluorescence. Note also that the width of the envelope of the pulses of the solid curve is approximately 0.08 cm^{-1} while for the dashed curve, most of the energy is in a single cavity mode whose width is only about 0.015 cm^{-1}. Clearly, this spectral behavior is significant for Doppler-shifted fluorescence measurements where we depend on convolution of the velocity-dependent laser and OH absorption lineshapes.

A further confirmation of our view that the dye laser bandshape is made up of random fluctuations of individual axial cavity modes is shown in Figure 21. This figure shows the average of 500 individual pulses recorded at 10 Hz in 50s with the linear detector. These measurements were made at 565 nm with 25 mJ dye pulse energy. Here, the fluctuations of the cavity modes from pulse to pulse are averaged. Over this time period, the spectral stability of the axial cavity mode structure is sufficient that the individual modes remain partially resolved. The FWHM of this ensemble of modes is only about 0.08 cm^{-1}, as opposed to

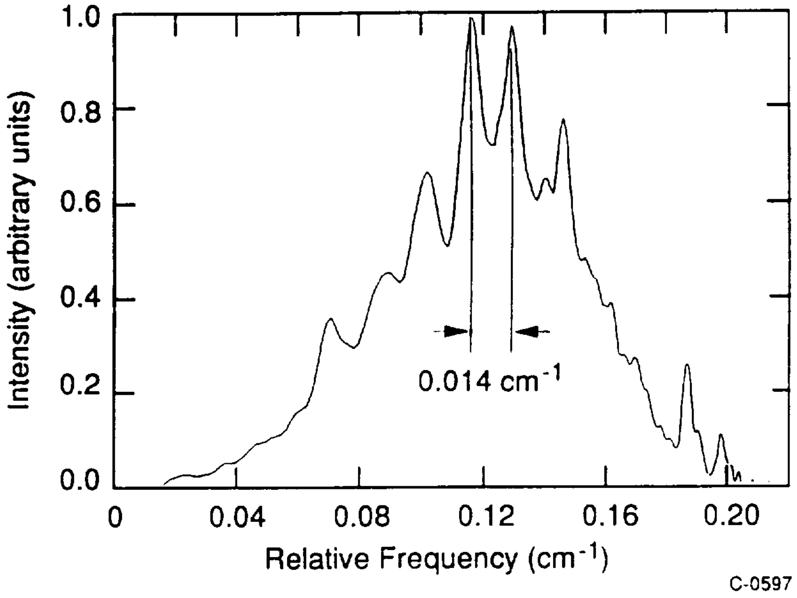

Figure 21. 500 Pulse Average FL-3002 Laser Bandshape at 565 nm

~0.13 cm^{-1} in the scanned-pinhole measurements of Figure 18. Some of this difference may be due to small changes in the laser alignment, which we have observed to result in significant variations in the dye laser bandwidth, between the two measurements. It may also be due to improved measurement resolution using the linear array which has an effective pinhole diameter of 25 μm, corresponding to the pixel spacing on the detector. Again, a slight increase in the overall bandwidth was noted when the laser was tuned to 540 nm.

These measurements suggest that the general manufacturer's specifications for the dye laser bandwidth used for the modelling studies of the Phase I portion of the program are too crude for actual measurement application. In order to understand the effect of these measured laser bandshapes on the overall predicted performance and accuracy of the instantaneous imaging velocimeter, we must analyze the frequency-doubled dye laser bandshape.

3.2 Relationship Between Visible and UV Bandshapes

The measured visible bandshape may be related to the corresponding UV bandshape by considering the physics of the frequency-doubling in the intra-cavity non-linear crystal (BBO for the FL-3002 laser). The colloquial term "frequency-doubling" is applied to describe the various non-linear optical interactions occuring in the crystal. Through the orientation of the crystal axis with respect to the propagating laser field, only certain interactions will be permitted. For this discussion, we are concerned principally with interactions arising from the second-order non-linear susceptibility, or $\chi^{(2)}$, which relates the induced polarization in a medium to the square of the incident field amplitude.

Consider first an applied electric field consisting of two monochromatic sources at ω_1 and ω_2 incident on the non-linear medium, representing two infinitesinal components of the laser bandshape (following the analysis of Ref. 22):

$$\mathbf{E} = E_1\cos(k_1x - \omega_1t) + E_2\cos(k_2x - \omega_2t) \tag{34}$$

where k_1 and k_2 are the wave-vectors associated with the two waves propagating in the x-direction. The non-linear polarization, **P**, is proportional to $\chi^{(2)}E^2$, giving

$$P \sim \chi^{(2)}[E_1^2\cos(2k_1x - 2\omega_1t) + E_2^2\cos(2k_2x - 2\omega_2t)] \tag{35}$$

corresponding to pure second harmonic generation (SHG) at twice the input frequencies. In addition, there are also created terms proportional to the sum and difference frequencies

$$P \sim \chi^{(2)}E_1E_2[\cos\{(k_1 + k_2)x - (\omega_1 + \omega_2)t\} + \cos\{(k_1 - k_2)x - (\omega_1 - \omega_2)t\}] \tag{36}$$

All three processes, in principle, occur simultaneously. Assuming the pump fields at ω_1 and ω_2 are not substantially depleted, the conversion efficiency is given by[22]

$$\frac{I_n}{I_o} = \frac{2\omega^2 d^2 \ell^2 I}{n^3 c^3 \epsilon_o}\mathrm{sinc}^2\left[\frac{\Delta k\ell}{2}\right] \tag{37}$$

where I_n is the intensity of the new field (at the second harmonic, sum, or difference frequency), d is the element of the non-linear susceptibility tensor for a given crystal orientation and interaction, l is the crystal path length, n is the real index of refraction of the non-linear medium, c is the speed of light, and ϵ_o is the permittivity of free space. The sinc^2 term contains the important phase-matching criterion which requires that the incident fields' phase velocity equal that of the new field (thereby maintaining coherent interaction along the crystal):

$$\Delta k = k_{2\omega} - 2k_{\omega} \qquad \text{(second harmonic)} \tag{38}$$

or

$$= k_{\omega_1+\omega_2} - k_{\omega_1} - k_{\omega_2} \qquad \text{(sum generation)} \tag{39}$$

or

$$= k_{\omega_1-\omega_2} - k_{\omega_1} - k_{\omega_2} \qquad \text{(difference generation)} \tag{40}$$

The phase synchronism factor is unity for $\Delta kl = 0$. Phase matching is obtained by adjusting the angle of the crystal axis with respect to the propagating field (hence the angle tuned crystal) which is adjusted to maximize the second harmonic conversion, i.e,

$$k_{2\omega} \approx 2k_{\omega} \tag{41}$$

If ω_1 and ω_2 are close together in frequency, then

$$2k_{\omega_1} \approx 2k_{\omega_2} \approx k_{\omega_1} + k_{\omega_2} \tag{42}$$

and the sum frequency generation will be nearly phase-matched as well. The difference field generation, however, oscillating at $\omega_1 - \omega_2$, is far removed in frequency from the second harmonic and sum frequency fields and will not be phase-matched (or will emerge from the crystal in the far-infrared and not contribute to the UV laser bandshape). In the remainder of our analysis, we will assume that the phase synchronism factor is equal for both SHG and sum frequency generation and constant over the UV laser bandshape.

If we now consider a single frequency of the UV bandshape at ω_3, we see that intensity of the field at this frequency is given by the combined contributions of SHG and sum frequency generation. The SHG is proportional to the sum of the square of the incident intensity at $\omega_3/2$ and the sum frequency generation is proportional to the product of the intensities at all symmetric frequencies ω_1 and ω_2 such that

$$\frac{\omega_3}{2} + \omega_1 = \frac{\omega_3}{2} - \omega_2 \tag{43}$$

and

$$\omega_1 + \omega_2 = \omega_3 \quad . \tag{44}$$

This concept is illustrated graphically in Figure 22. A visible bandshape, $I_{(\omega)}$, is shown, along with a reversed and shifted bandshape, $I_{(x-\omega)}$. The intensity of the converted field at twice the center frequency of the shift, $2\omega_n$, is proportional to the square of the intensity at ω_n plus the sum of the product of all the intensities at symmetric frequencies about ω_n, as indicated by the shaded area. Note that $2\omega_n$ is the same as ω_3 in Eqs. (43) and (44). Similar calculations for every value of x yields the bandshape of the "frequency-doubled" field, now centered about twice the frequency of the incident field.

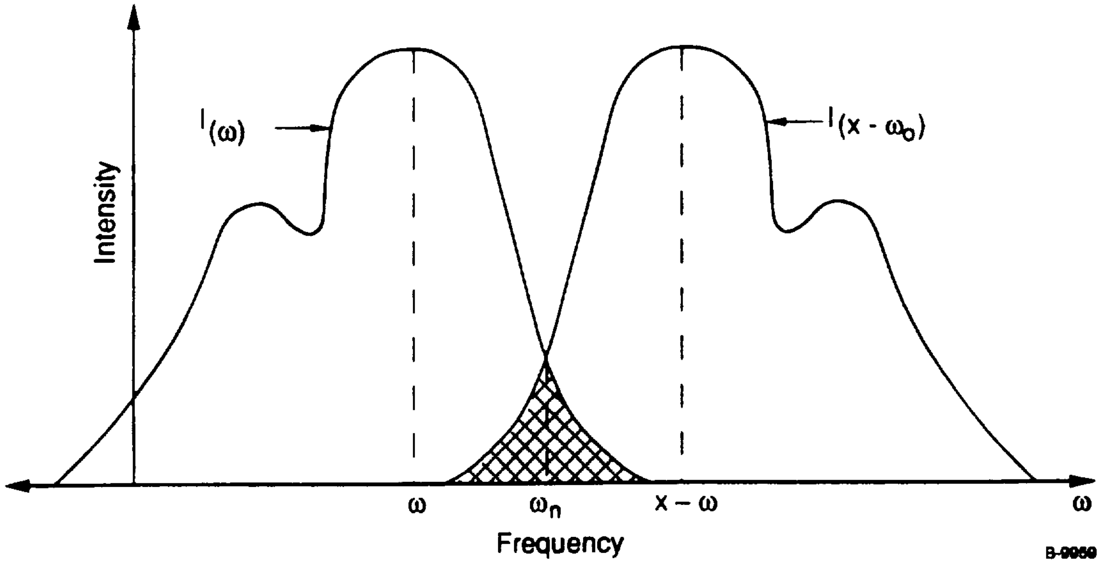

Figure 22. Conceptual Diagram of a Self-Convolution

This approach leads to the definition of the self-convolution of the incident visible laser bandshape

$$I_{2\omega_n} = \int_{-\infty}^{+\infty} I_\omega I_{(x-\omega)} d\omega \tag{45}$$

where the functional variable of the self-convolution is identified with one-half of the "frequency-doubled" field.

Performing this analysis on several single-pulse visible bandshapes, such as shown in Figure 20, results in an approximation of the UV bandshape which would actually excite the Doppler-shifted fluorescence. Figure 23 shows the calculated single-pulse UV bandshapes from four measured visible bandshapes, two of which were shown in Figure 20. The smoothing effect of the self-convolution is immediately evident and these results are consistent with our experimental observations that the fluorescence intensity in a stable OH field does not fluctuate markedly from laser pulse to laser pulse. The FWHM of the bandshapes, however, is considerably narrower than the Lambda-Physik literature would indicate. Typical widths are about 0.2 cm^{-1}, less than half of the expected linewidth used in the Phase I modelling study.

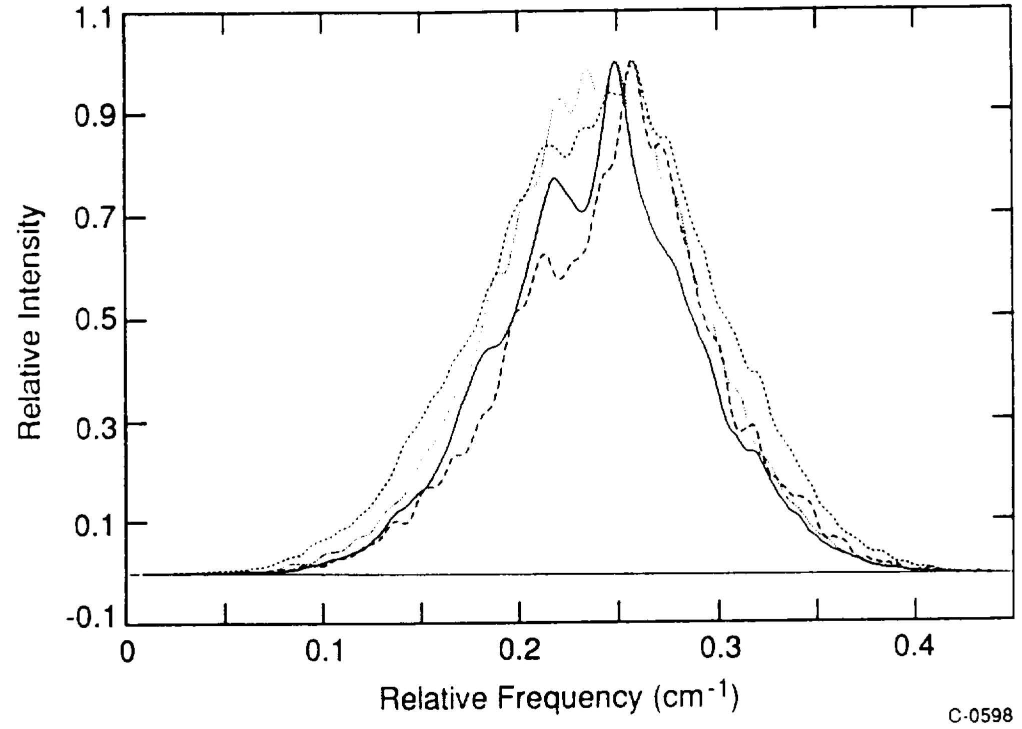

Figure 23. Calculated Single Pulse UV Laser Bandshapes

In order to examine the effect of the laser bandshape stability, we first consider the case of OH in a 1 atm, 2050 K hydrogen/air flame (corresponding to the stoichiometric conditions in our flat-flame burner study of the OH collision broadening parameters). For equilibrium major product concentrations, the Voigt a-parameter for the OH absorption bandshape is 0.195. Recall that for counter-propagating laser sheets, the following ratio is constructed from the up-shifted (S_{f+}) and down-shifted (S_{f-}) measurements,

$$\psi = \frac{2S_{F^+}}{S_{F\pm}} - 1 \tag{46}$$

Figure 24 is calculation of ψ for several UV laser bandshapes and the OH absorption bandshape described above. The two dashed lines represent the variation in the velocity sensitivity when the laser is tuned to a frequency near the FWHM of the convolution profile of stationary OH molecules. These two curves were calculated using the frequency-doubled versions of the two-bandshapes shown in Figure 20. Even for these rather large variations in the shape of the single-pulse visible bandshape, the smoothing effect of the

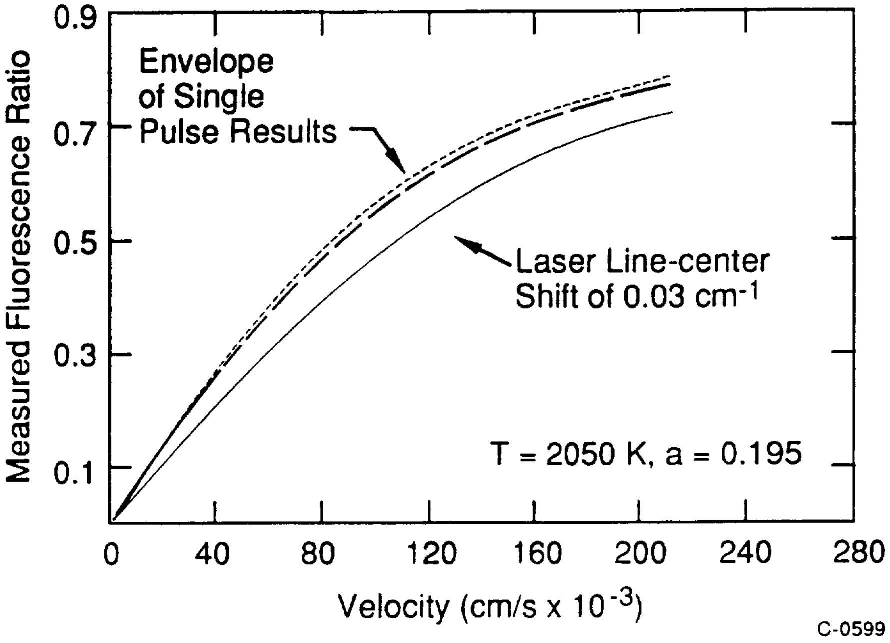

Figure 24. Calculated Fluorescence Ratio versus Velocity for Measured UV Laser Bandshapes (See text for explanation)

frequency-doubling and the relatively small contribution of the laser linewidth to the convolution linewidth results in only about 6% uncertainty in the measured velocity at 120,000 cm/s.

The solid line is the fluorescence ratio calculation when one of the laser bandshapes is shifted in frequency by 0.03 cm^{-1}, in this case toward the absorption center frequency. This shift results in a 27% change in the inferred velocity from a given measured fluorescence ratio. Hence, for these relatively narrow laser bandshapes, pulse-to-pulse instability of the exact laser bandshape has much less effect on the uncertainty of the velocity measurement than does the absolute stability of the laser center frequency.

Another consequence of the narrower-than-expected laser bandshape is shown in Figure 25. This figure contains three families of three curves each. Each family of curves corresponds to a particular detuning of the laser center frequency with respect to the static OH absorption line-center frequency and is indicated by the legend. Within each family, the three curves represent isentropic variations of the gas conditions. The gas conditions were chosen as representative of portions of the exhaust from the supersonic burner to be used for the experimental verifications to follow in the second year of the program. The conditions are: 2 atm, 1820 K: 1 atm 1500 K, and 0.5 atm, 640 K. At lower pressures and temperatures, the OH bandshape becomes narrower, thereby altering the shape of the fluorescence ratio/gas velocity curve. Compared to the conditions investigated analytically in the Phase I program, the narrower laser bandshape here results in substantial variations in the inferred velocity at a given fluorescence ratio. No "ideal" detuning appears to exist which can minimize or eliminate these unwanted dependencies on temperature and pressure. The nominal case is the best compromise between large velocity dynamic range and pressure/temperature sensitivity, although this case has nearly 50% uncertainty at 60,000 cm/s and a velocity dynamic range which is limited to about 100,000 cm/s.

This unacceptably large uncertainty can be reduced by broadening the laser profile so that the convolution profile is less sensitive to small variations in the absorption bandshape. Slight misalignment of the dye laser cavity is the most obvious approach for broadening the bandwidth since we know from prior

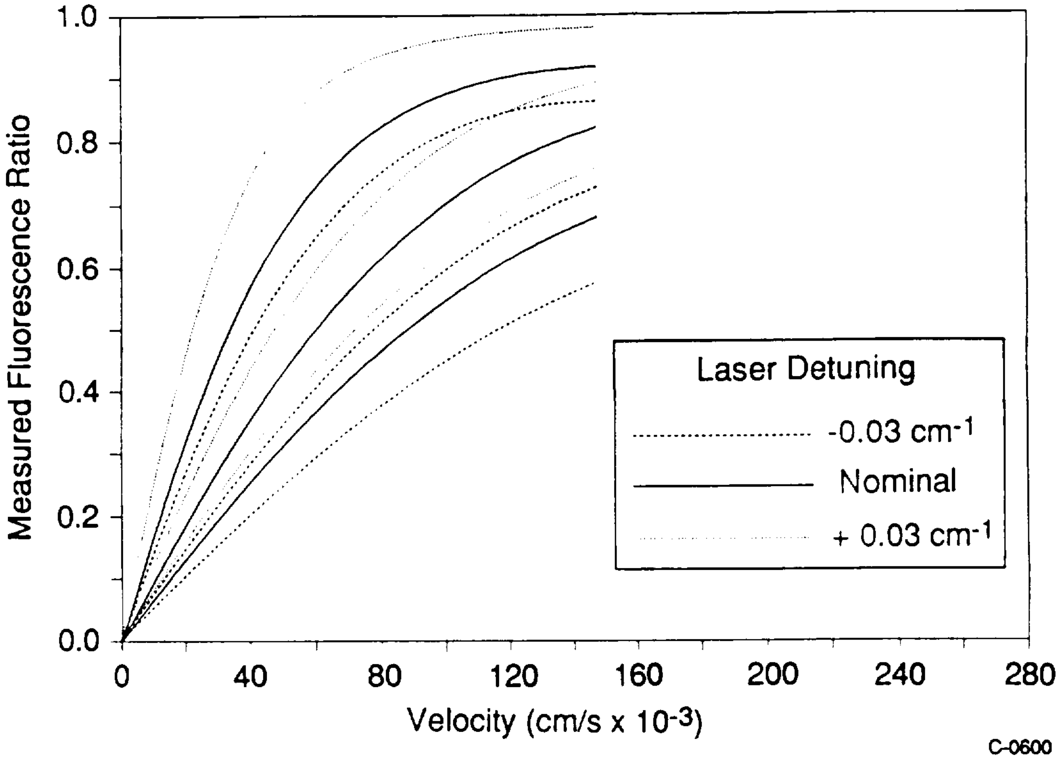

Figure 25. Calculated Fluorescence Ratio versus Velocity for Isentropic Flow Variations

experience that much broader *mean* bandshapes are possible. However, misalignment seemed to result in no substantial increase in the *single-pulse* bandshape, but rather an increased instability in the center-frequency of the bandshape. As shown in Figure 25, 15% changes in the laser center-frequency can introduce substantial uncertainty in the measured velocity.

3.3 Modification of Single-Pulse Bandshape

It was clear that a larger laser bandwidth was required. There are several options for increasing the single-pulse laser linewidth. The simplest is to purposely operate the dye laser grating tuning element in a lower order, thereby reducing the dispersion of this frequency-selective element in the laser oscillator. Further increase to the laser bandwidth may be realized by partially blocking the grating, thereby reducing the dispersion of the grating reflection.

Figure 26 shows a schematic of the dye oscillator configuration with our modification. In the Lambda-Physik design, the laser beam oscillates between a fixed end mirror and a variable-angle grating. The cavity is out-coupled from a front-surface reflection off the first prism of the prism beam expander assembly, reflected again off the grating, and directed back through the dye cell where it is single-pass amplified. The grating, of course, acts as the wavelength selection element by only back reflecting wavelengths matching the Littrow condition along the oscillator axis.

The bandwidth of the oscillator is related to the resolving power of the grating, leaving aside the complexity of gain narrowing due to saturation and mode competition. This resolving power is simply proportional to the number of grooves illuminated by the oscillator beam, hence the purpose of the beam expander in the standard configuration. By inserting a partial beam block, we effectively reduce the size of

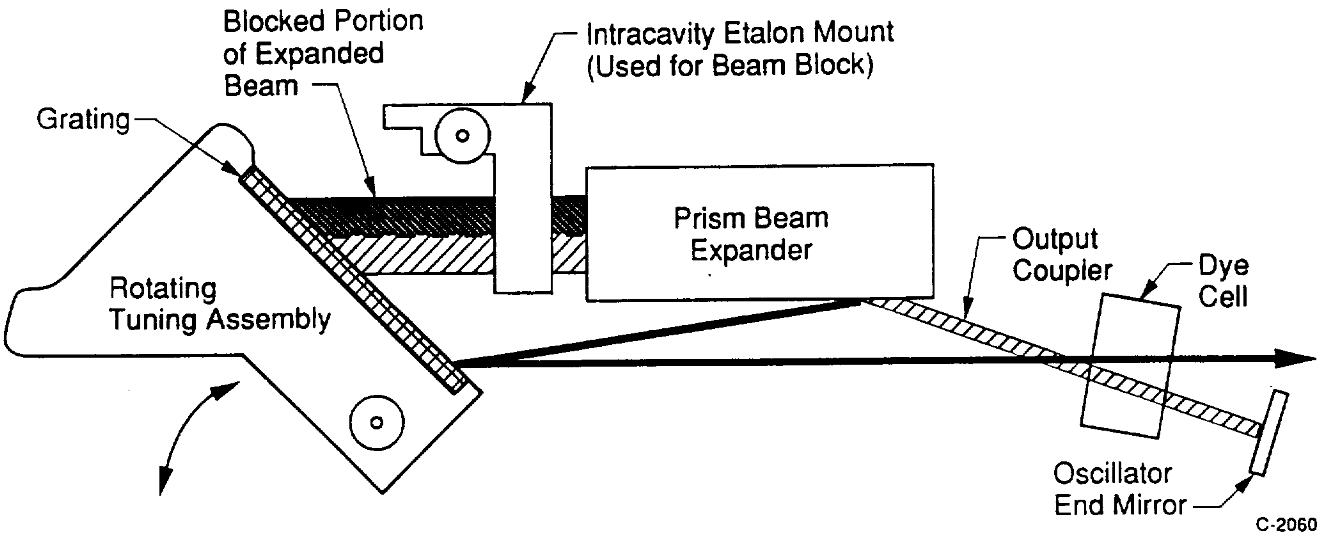

Figure 26. Schematic Diagram of FL-3002 Oscillator Cavity Configuration Showing Positioning of Partial Beam Block

the grating, thereby increasing the bandwidth of the radiation which will retro-reflect back through the cavity. Since this bandwidth is an upper limit for the envelope under which the laser modes may oscillate, we would expect this approach to yield a larger envelope of laser modes without any substantial change in the width of the individual modes themselves. Ideally, we would like to smooth the overall bandshape by increasing the cavity mode width as well as increase the number of available modes. In principal, the cavity mode width is inversely related to the lifetime of the cavity. Hence, additional loss elements in the cavity will reduce the cavity lifetime and should increase the bandwidth of individual modes.

To explore this concept, we initially attempted a modification addressing both the envelope bandwidth and individual mode bandwidth. The etalon holder was fitted with a 80 cm focal length cylindrical lens whose power axis was aligned with the grating axis. This lens slightly converged the oscillator beam incident on the grating, thereby increasing the acceptance angle bandwidth of the grating. Since the light circulating in the oscillator was no longer exactly collimated, there was a walk-out loss, diminishing the cavity lifetime and thus broadening the width of individual modes.

Both concepts (beam block and intracavity lens) were evaluated using the single-pulse monitoring setup shown in Figure 16. The intracavity cylindrical lens was found to increase the single-pulse bandwidth to ~ 1 cm^{-1}, broader than we desired. We then concentrated on the beam block option. Figure 27 is a comparison of the visible single-pulse laser bandshape with and without the oscillator beam block. Clusters of individual cavity modes are visible in both bandshapes, but the modified bandshape is more than twice as broad. Significantly, this broadening was achieved with no loss of power. As the blocking was increased beyond half of the grating, the laser pulse energy gradually decreased, therefore we settled with the half blocked position.

Figure 28 is compilation of five single-pulse bandshapes from the modified laser. The pulse-to-pulse stability is essentially the same as with the standard configuration, demonstrating that the modification has not deteriorated the frequency stability of the laser. The extent of the modification is most clearly demonstrated in Figure 29, a comparison of the average bandshapes of the modified and standard configuration. The standard configuration average bandwidth is 0.15 cm^{-1} whereas the modified configuration is 0.24 cm^{-1}, a factor of 1.6 increase. This is close to the doubling of the bandwidth that we desired.

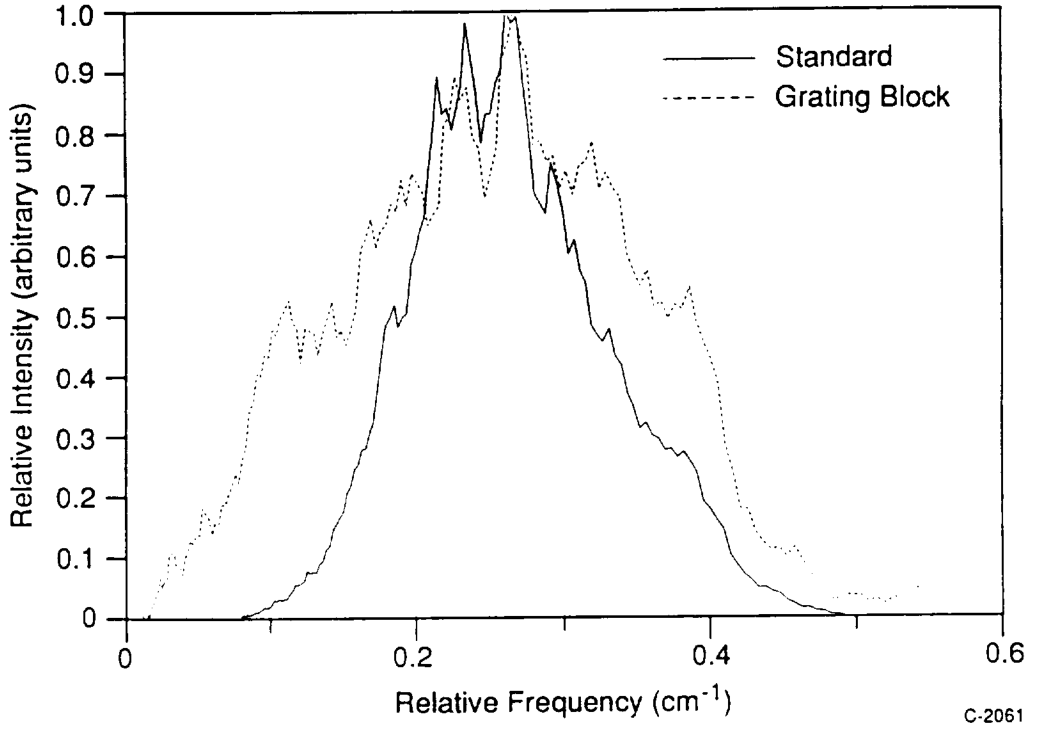

Figure 27. Modified Single-Pulse Bandshape of the FL-3002 Dye Laser. The laser was tuned to 565 nm and the pulse energy was 25 mJ.

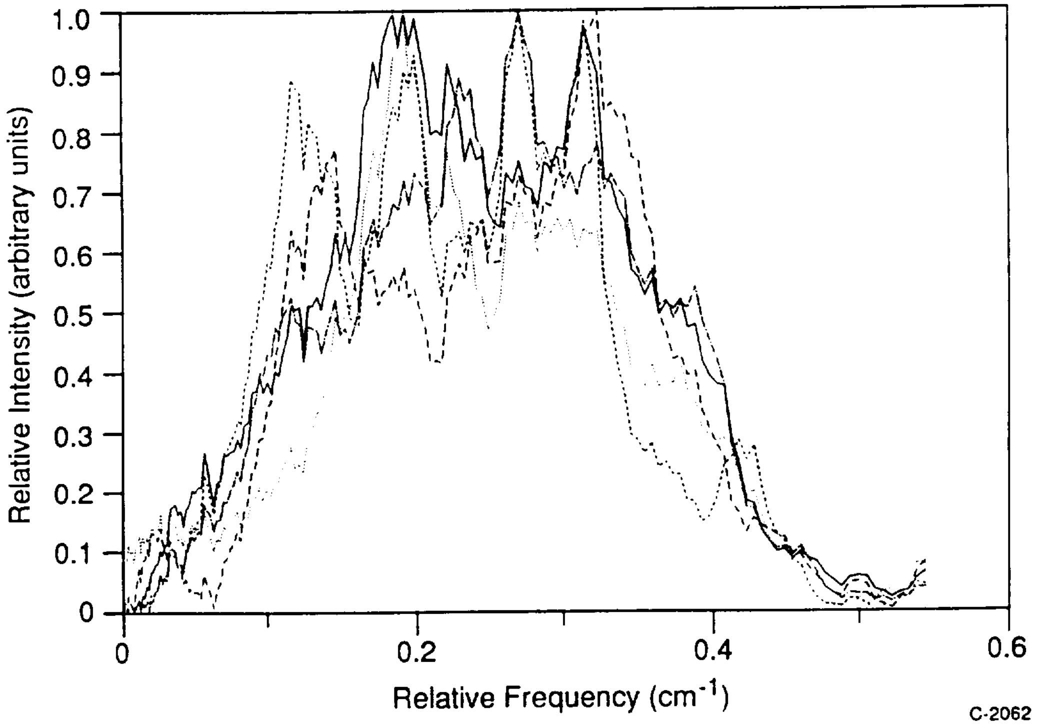

Figure 28. Single-Pulse Bandshapes of Modified FL-3002 Dye Laser.

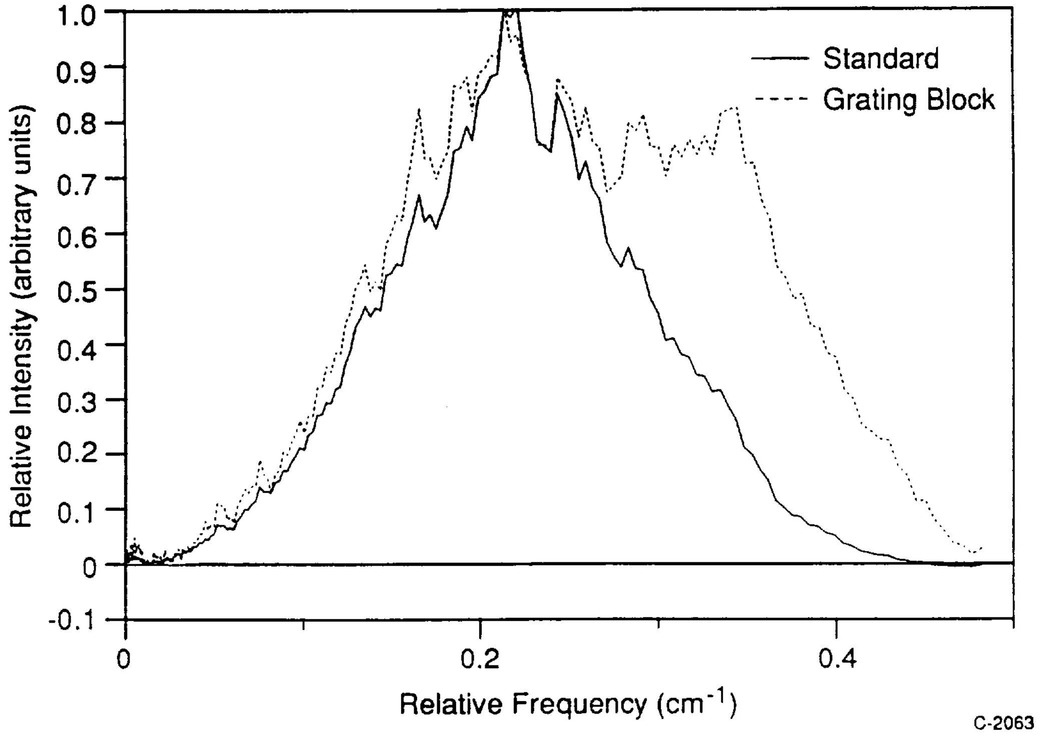

Figure 29. Comparison of Standard and Modified Average Visible Bandshape of FL-3002 Dye Laser.

We also investigated the UV bandshapes following frequency-conversion directly by fitting the interferometer with UV-reflective mirrors. The finesse of this setup was somewhat lower than with the visible mirrors, principally due to the increased alignment tolerances associated with the UV, but was nevertheless sufficient to check our frequency-conversion model and to verify the exact UV wavelength following the oscillator modification. Figure 30 shows three single-pulse bandshapes of the UV output at 283 nm.

As predicted by our model, the UV bandshapes do not exhibit fully resolved cavity modes. In our model, these modes are smoothed by the self-convolution of the visible bandshape. The zig-zag pattern on the data is due to noise in these low signal-level scans. Some undulations indicate the presence of modal structure, as we would expect, although the overall UV bandshapes are considerably smoother than their visible counter parts.

The bandwidth of each of these single pulses is approximately 0.24 cm^{-1}. It was not possible to simultaneously measure visible and UV bandshapes, so we can only compare our model predictions using average bandshapes. To check the model, we measured the average bandshape in the UV, then removed the BBO crystal and changed the interferometer mirrors as quickly as possible, trying to preserve the laser alignment. Our model of the UV-conversion was then exercised to convert the measured visible bandshape into a UV bandshape. This calculated bandshape is shown in comparison to the measured UV average bandshape in Figure 31. Except for one wing of the measured bandshape, the agreement between the calculated and measured bandshapes is excellent. We believe the asymmetry of the measured UV bandshape is an artifact of the measurement procedure related to the frequency-dependent transmission of the interferometer across an individual fringe.

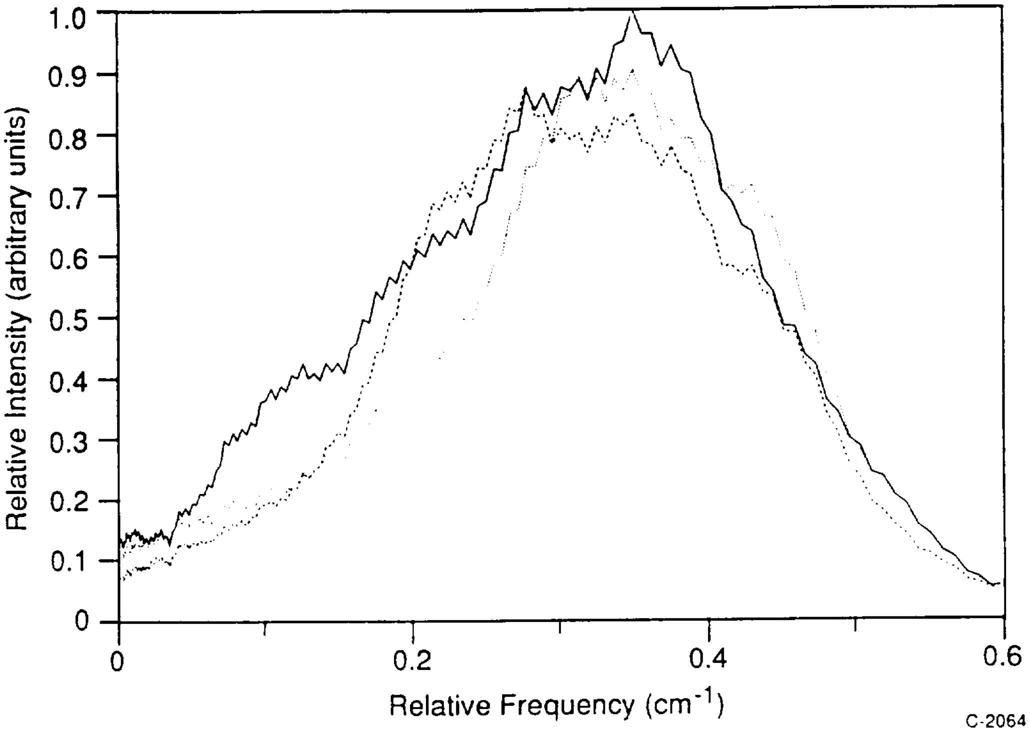

Figure 30. Single-Pulse UV Bandshapes from FL-3002 Dye Laser at 283 nm.

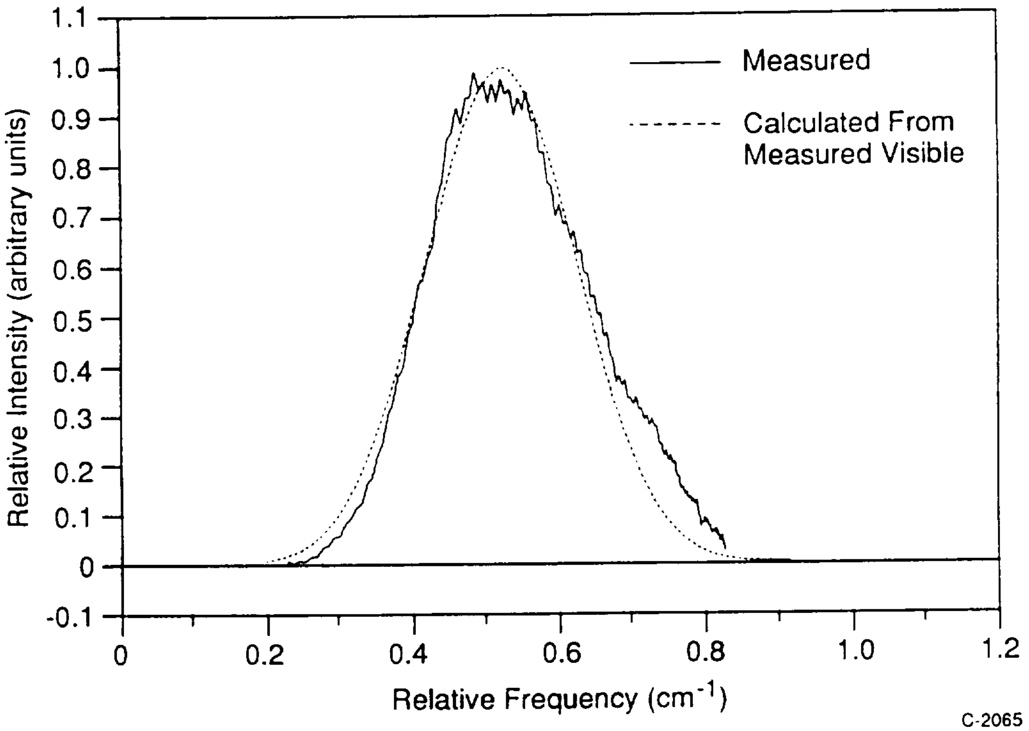

Figure 31. Comparison of Measured and Calculated Average UV Bandshapes.

This agreement had a very direct and significant impact on the operational configuration of the imaging velocimeter. Since the laser bandshape requires measurement during a velocity measurement sequence, we must measure either the visible or UV bandshape. The UV pulse energy, however, is very low and we desire to use all of the available energy for the fluorescence measurement rather than splitting a portion off for the bandshape measurement. Further, the low signal levels in the interferometer and the difficulty in achieving good alignment in the UV result in a somewhat poorer record of the UV bandshape compared with the visible. The demonstrated ability to convert a measured visible bandshape into its corresponding UV bandshape relieved one of the need to split off part of the UV light. Excess visible radiation was naturally available from the incomplete UV-conversion, so that using it for the bandshape measurement did not affect the UV pulse energy.

Lastly, we show a direct UV measurement of the effect of the oscillator grating block modification on the UV bandshape in Figure 32. The dashed line shows the bandshape for the modified UV pulse which, unfortunately, overfilled the free-spectral range of the interference pattern near the origin. We can estimate the true FWHM of the modified bandshape from twice the right side half-width at half-maximum, giving a modified bandwidth of 0.33 cm^{-1}, approximately 1.5 times greater than the standard configuration bandwidth. With our verified UV-conversion model, we may calculate the modified UV bandshape from the modified visible bandshape shown in Figure 6. The results of this calculation are shown in Figure 33, where the calculated modified UV bandshape is shown compared a Gaussian bandshape with FWHM = 0.35 cm^{-1}. The modified average UV bandshape is closely Gaussian with its FWHM broadened by approximately the same factor as the visible bandshape.

In summary, this section has described the detailed experimental and analytical investigation conducted of the single-pulse and UV bandshape behavior of an excimer-pumped dye laser. These are among the first such observations and the results have implications for a variety of laser-based flow diagnostic

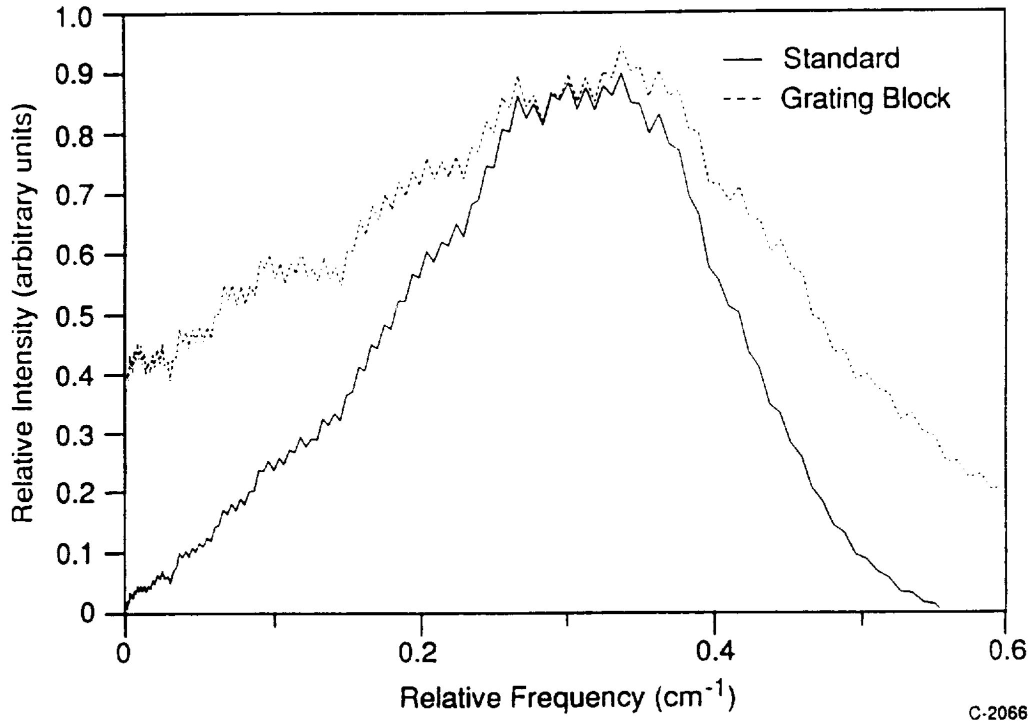

Figure 32. Comparison of Standard and Modified UV Bandshapes of FL-3002 Dye Laser.

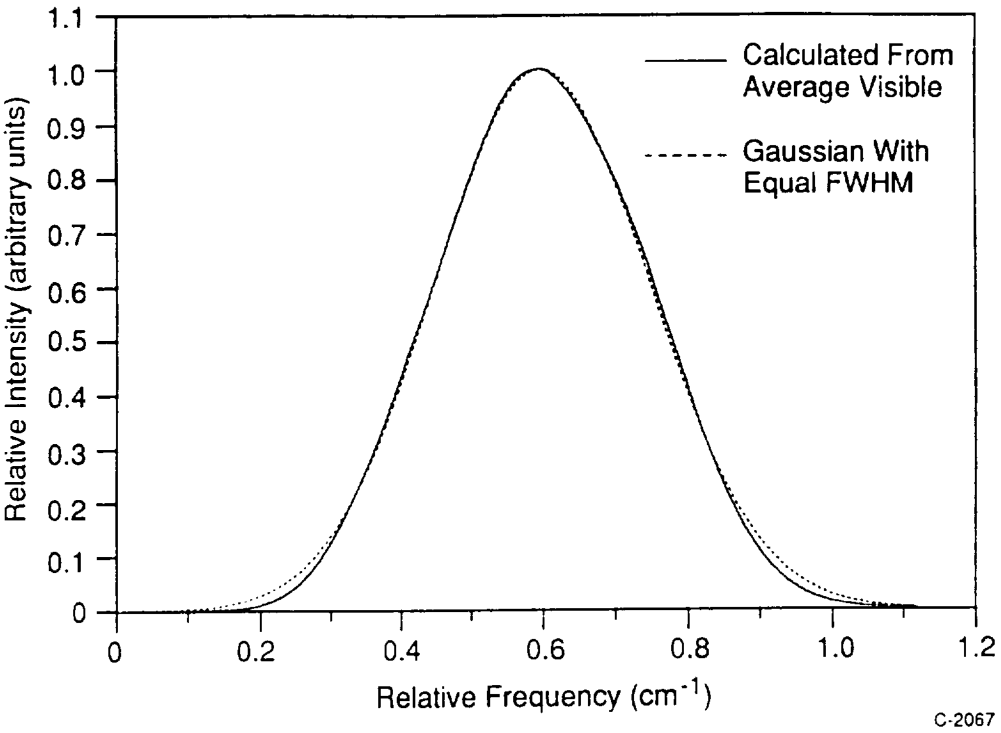

Figure 33. Comparison Between UV Bandshape Calculated from Average Visible Measurement and a Gaussian Bandshape with FWHM = 0.35 cm^{-1}.

techniques, particularly at elevated pressures where the details of the laser and absorption lineshape overlap integral (the velocity-sensitive first factor in Eq. (1)) can be an important concern in quantifying the fluorescence measurements. As we were completing our measurements, an article appeared which, although it did not address the cavity modifications which we explored, confirmed the essential observations we made of the single pulse bandshape behavior.[23] We are in the process of preparing a manuscript describing our results for publication. These results, along with the OH lineshape measurements described in the previous Section, were used to quantitatively reduce the fluorescence image ratios to velocity maps.

4. SUPERSONIC FLOW FACILITY

4.1 Supersonic Burner Overview

Development and optimization of the velocity imaging technique required a stable, continuous source of high velocity gases at temperatures and pressures relevant to SCRAMJET operation. As detailed in the Phase I Final Report, an underexpanded supersonic jet flow with high temperature, high pressure stagnation conditions provides a good test flowfield. The jet flow is reasonable well understood, both experimentally and analytically, and contains a wide range of velocity, pressure, and temperature variations in a small region downstream of the jet exit. These variations provide a stringent test of the technique's ability to determine gas velocity in the presence of large, uncharacterized in-plane variations in temperature and pressure. This section describes the development of a high pressure supersonic $H_2/O_2/N_2$ burner used as the principal test-bed in the program.

A schematic diagram of the burner facility layout and its relationship to the imaging systems and counter-propagating laser sheets is shown in Figure 34. The cylindrical burner is mounted in a rigid yoke in the center of a 3 x 6 ft mobile table. The yoke assembly is mounted on a rotating translation stage assembly which allows precise control of the jet exhaust flow position. The entire assembly may be rotated in order to adjust the vector product of the core gas flow and the laser beam and then translated along the jet axis at the given orientation. In this manner, the optical setup for the imaging or pointwise measurements can be carefully aligned at a fixed position in the jet and then axial jet properties determined by translating the burner.

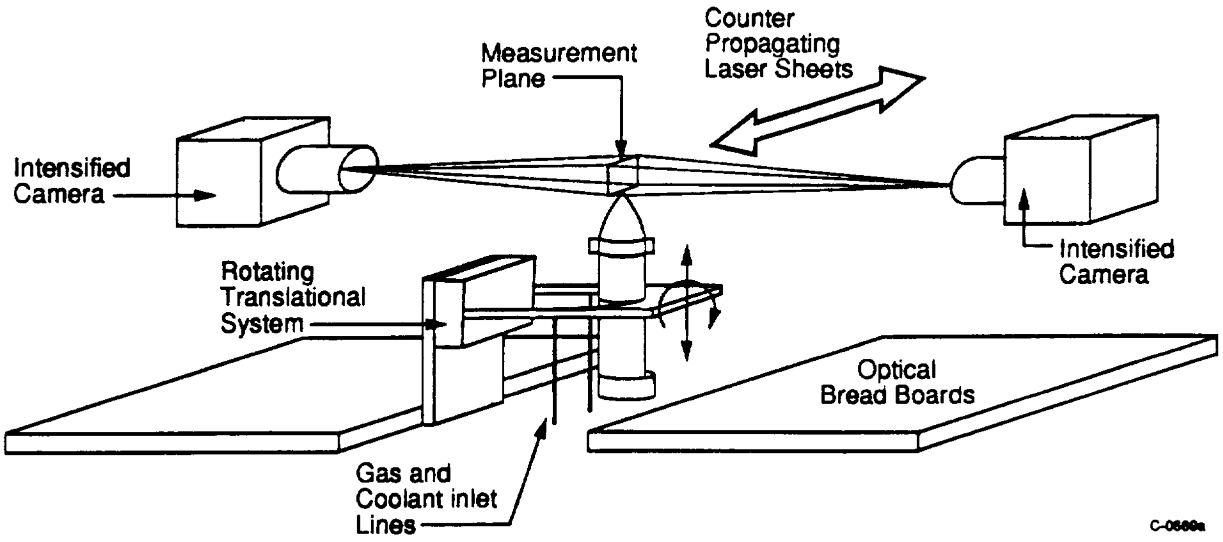
Measurement Plane
Counter Propagating Laser Sheets
Intensified Camera
Intensified Camera
Rotating Translational System
Optical Bread Boards
Gas and Coolant inlet Lines
C-0666a

Figure 34. Schematic Diagram of Burner Facility Layout

Gas delivery, cooling, and instrumentation feed lines are attached to the mounting yoke through flexible lines. Optical breadboards bracket two sides of the mounting assembly for positioning the intensified camera systems, photomultiplier tubes, or any other optical detection systems required. The other two sides of the mounting assembly consist of aluminum plates with positioning holes for mounting optical rails. The optical rails carried the various laser beam steering and shaping optics for the velocimeter.

A more detailed schematic of the burner itself is shown in Figure 35. A detailed thermal and mechanical design was completed to allow construction and safe operation of a continuously flowing, high-pressure, high-temperature burner. The body of the burner consists of a 2 in. id carbon steel pipe 6 in. in length which is surrounded by a press-fit copper jacket. The copper jacket is provided to improve the temperature uniformity of the cooling system. The stainless steel burner base is machined with a slight annular indentation. Four sonic hydrogen injectors are located symmetrically around this indentation, along with a spark ignitor and condensation drain. The hydrogen injectors are connected to a common fixed manifold at the based of the mounting system. The base is mechanically held to the burner body by a large stainless steel flange nut which clamps the base to the threaded carbon steel burner body. A copper gasket is used to seal the base/body interface.

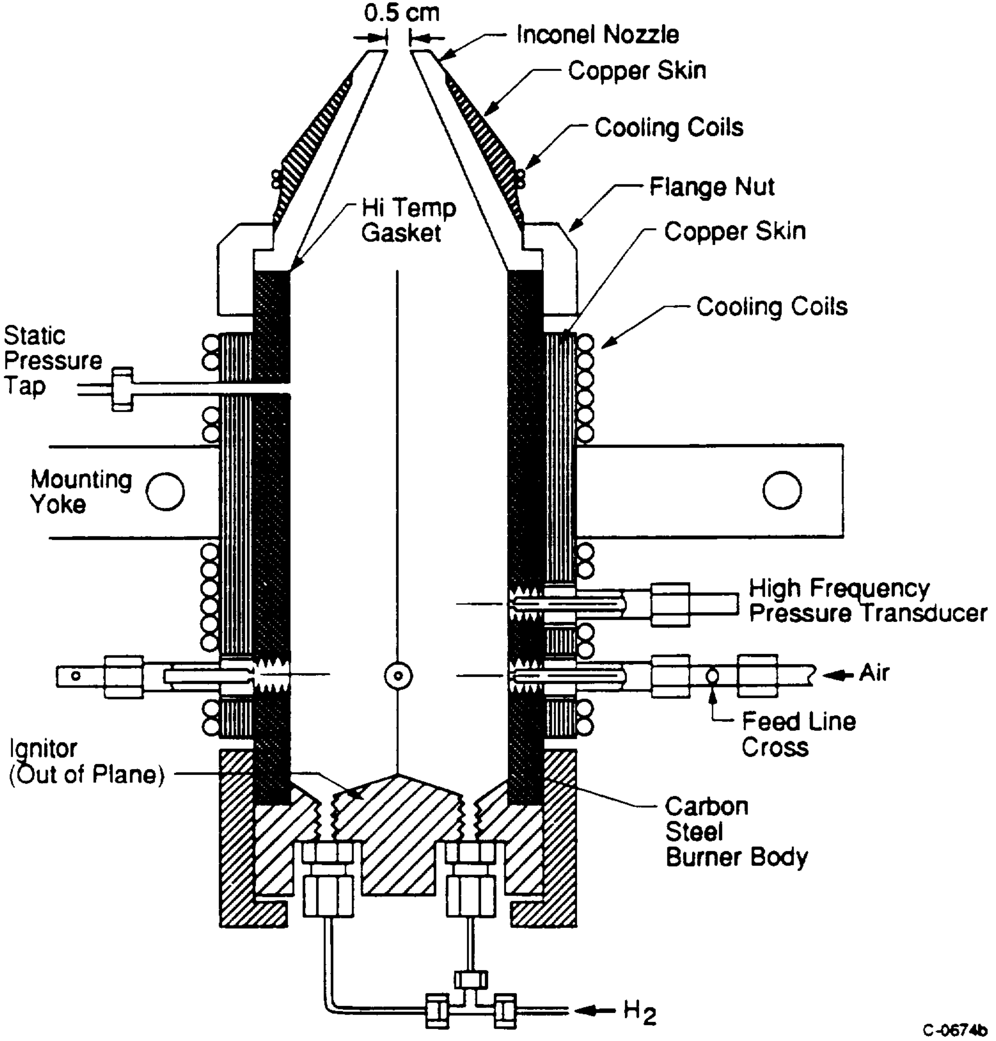
0.5 cm
Inconel Nozzle
Copper Skin
Cooling Coils
Flange Nut
Hi Temp Gasket
Copper Skin
Cooling Coils
Static Pressure Tap
Mounting Yoke
High Frequency Pressure Transducer
Air
Feed Line Cross
Ignitor (Out of Plane)
Carbon Steel Burner Body
H_2
C-0674b

Figure 35. Detailed Schematic of High-Pressure Burner

Four sonic, radial oxidizer jets are placed symmetrically around the burner one radius above the base. The oxygen/nitrogen ratio of the oxidizer may be separately adjusted. Immediately above the oxidizer jets is a tap for a high-frequency pressure transducer, which is discussed in more detail in Subsection 4.2. A static pressure tap is provided above the mounting yoke. Stainless steel cooling coils are silver-soldered onto the entire length of the copper jacket. A 70 deg interior taper nozzle, manufactured from Inconel 600, tapering to a 5 mm exit diameter, is clamped onto the end of the burner in the same manner as the base. A tapered copper skin is press-fit onto the nozzle for improved heat transfer in the nozzle cooling system.

The extreme heating of the burner nozzle was a principal design constraint in the burner and the coolant requirements. In order to maximize the enthalpy in the gas, it was desired to run the burner wall temperatures as high as possible. This necessitated selection of DOW-THERM A coolant (a commercial blend of 30% biphenyl oxide and 70% biphenyl), a common heat transfer solution in the chemical processing industry. Using a closed loop cooling cycle pressurized to 150 psi, this permited operation at interior wall temperatures up to 700 K. The heat transfer to the nozzle wall was modelled using a turbulent boundary layer heat transfer solution (standard turbulent pipe flow, later verified with a more complete convective solution from the STAN-5 code) coupled to a finite difference conduction solution through the wall and copper jacket.

A solution showing the interior wall temperature profile and integrated heat flux along the nozzle is shown in Figure 36, assuming a 2200 K, 100 psi gas. For reference, the adiabatic flame temperature for stoichiometric hydrogen/air combustion is 2440 K. As shown in the figure, the uncooled nozzle orifice rises to slightly above 1200 K, near the mechanical limits of the Inconel. This can be lowered by simply adjusting the amount of cooling. As shown, the integrated heat flux for this solution is slightly above 800W, whereas the nozzle portion of the cooling system is designed to extract up to 1500W at full capacity. For a safety margin, we consider the same solution with a 50% increase in the convective heat transfer coefficient. This solution is shown as the dashed lines in the figure. By increasing the coolant capacity to its design limit, it is still possible to maintain the nozzle orifice temperature within its safe operating limits.

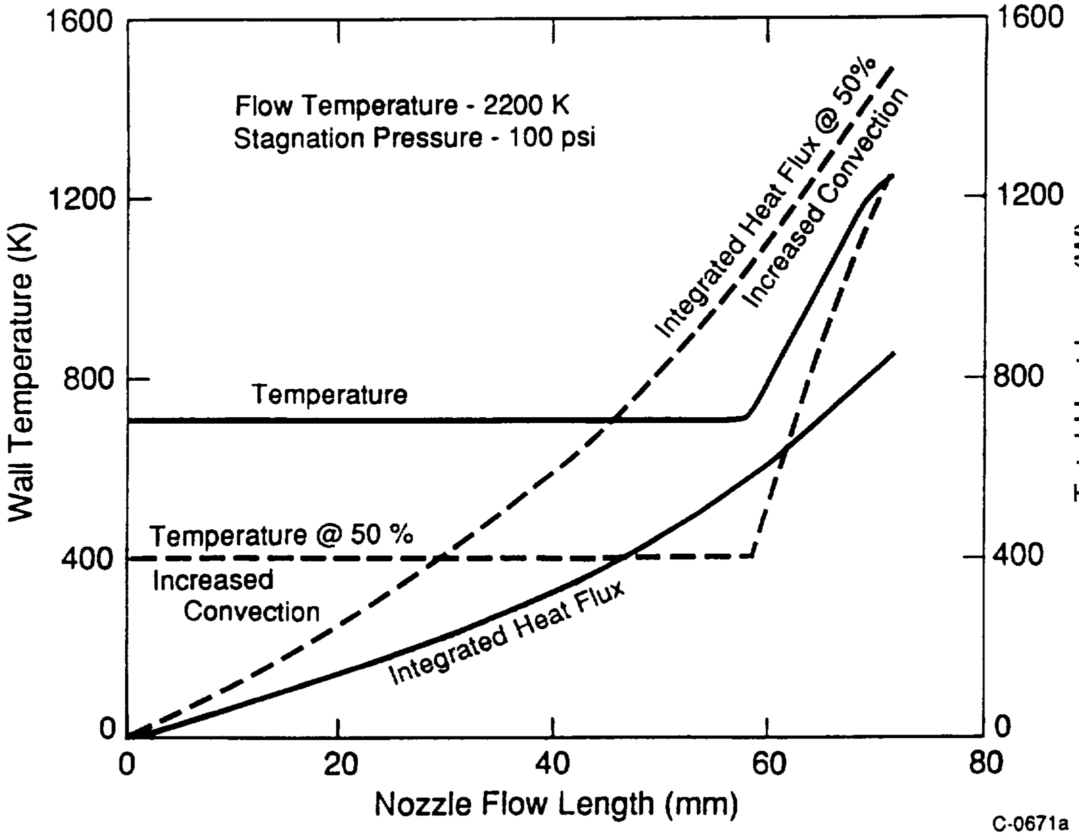

Figure 36. Nozzle Temperature and Integrated Heat Flux Profiles

A schematic diagram of the gas delivery system is shown in Figure 37. Oxygen, nitrogen, and hydrogen are delivered to separate rotameters on the flow metering panel attached to the mobil burner cart. Maximum gas delivery pressure to the burner is ~300 psi. Static flow pressure at the rotameters and immediately upstream of the injection nozzles are continuously monitored during a run. An automated safety system monitors the burner pressure and shuts off the hydrogen flow in the event of a sudden drop in burner pressure. This hydrogen shut-off is also triggered by a suddenly loss of pressure in the coolant system. The coolant system is a closed-loop with separate control of the burner body and nozzle coolant flow rates and a water cold-side heat exchanger. The system is pressurized with nitrogen over a small reservoir. Both the coolant temperature and pressure are continuously monitored during a run.

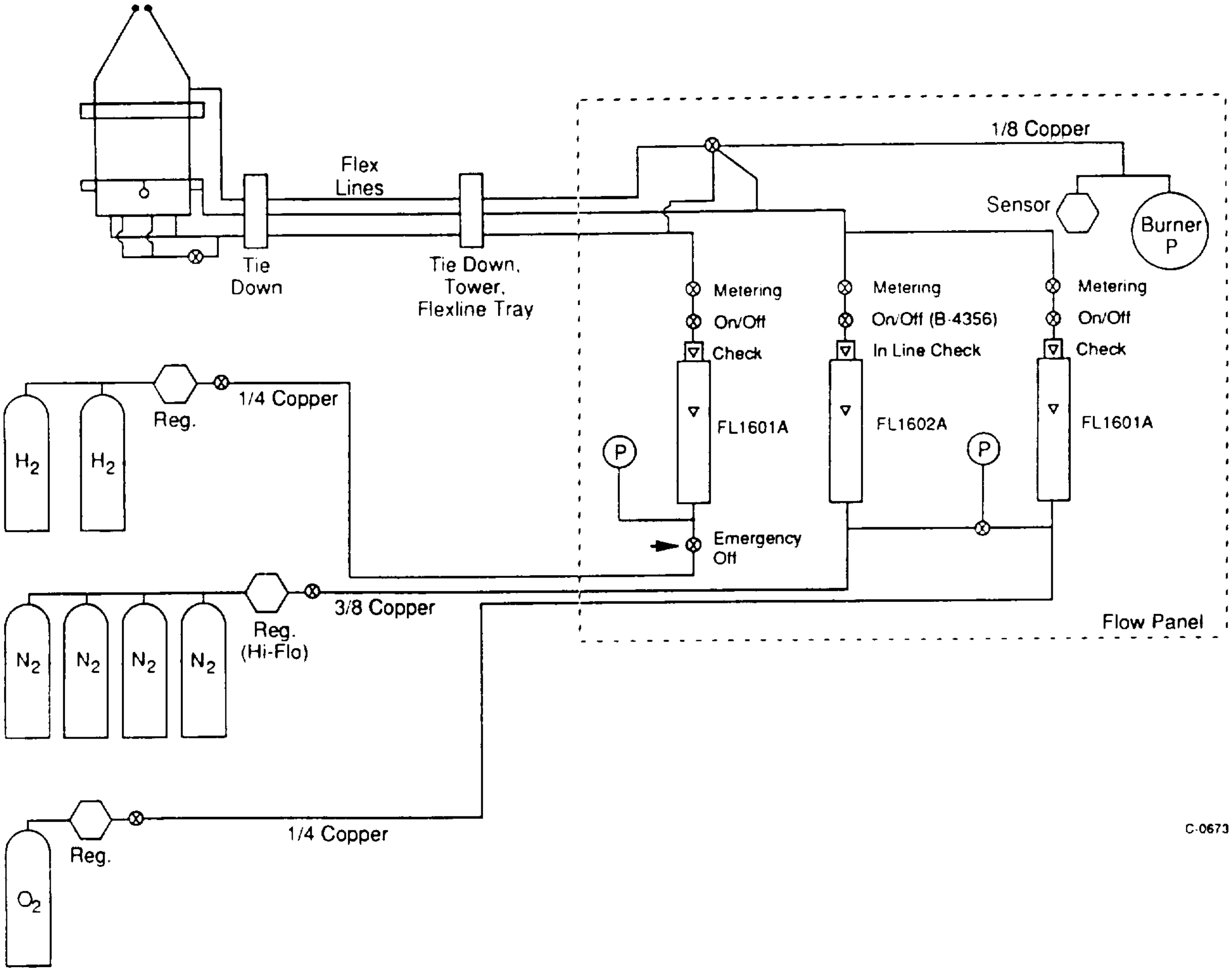
Flex Lines
Tie Down
Tie Down, Tower, Flexline Tray
1/8 Copper
Sensor
Burner P
Metering
On/Off
Check
FL1601A
Metering
On/Off (B-4356)
In Line Check
FL1602A
Metering
On/Off
Check
FL1601A
P
P
Emergency Off
Flow Panel
Reg.
1/4 Copper
H_2
H_2
3/8 Copper
Reg. (Hi-Flo)
N_2
N_2
N_2
N_2
Reg.
1/4 Copper
O_2
C-0673

Figure 37. Schematic Diagram of Gas Delivery System.

4.2 High Frequency Pressure Transducer Design

A principal complication in the experimental portion of the Phase I program was due to large amplitude pressure instabilities in the first version of the high pressure burner. These instabilities resulted in poor fuel and air mixing and non-uniform exhaust profiles. Because of this, a great deal of care was given in the design of the Phase II test bed. All fuel and air injectors are sonic, thereby eliminating feed-line instabilities. The combined radial and axial injector systems enhanced rapid mixing and burning. In addition, the radial air jets were located near the position of the maximum amplitude of the 1/4 wave axial instability mode of the burner. This positioning was intended to disrupt any standing wave instabilities which might otherwise develop.

In the initial shake-down runs of the burner, we monitored the burner pressure with a fast-response pressure transducer in order to identify any instabilities which might be present. Flush wall-mounted transducers provide maximum frequency response for most flow applications; however, due to thermal operating limits associated with the piezoelectric transducer element used for this application (PCB Piezotronics Model 111A22; maximum temperature = 400 K), a liquid-cooled mounting jacket separating the transducer from the hot combustion environment was necessary to ensure proper transducer performance. Two major considerations in the design of the transducer mounting jacket were: a) that it provides a safe thermal environment for the transducer; and b) that the high-frequency response of the transducer/mount combination is adequate for the given application. For the chosen configuration (Figure 38) the frequency response characteristics are influenced by the thermal field and because of this a heat transfer analysis of the proposed design was performed first.

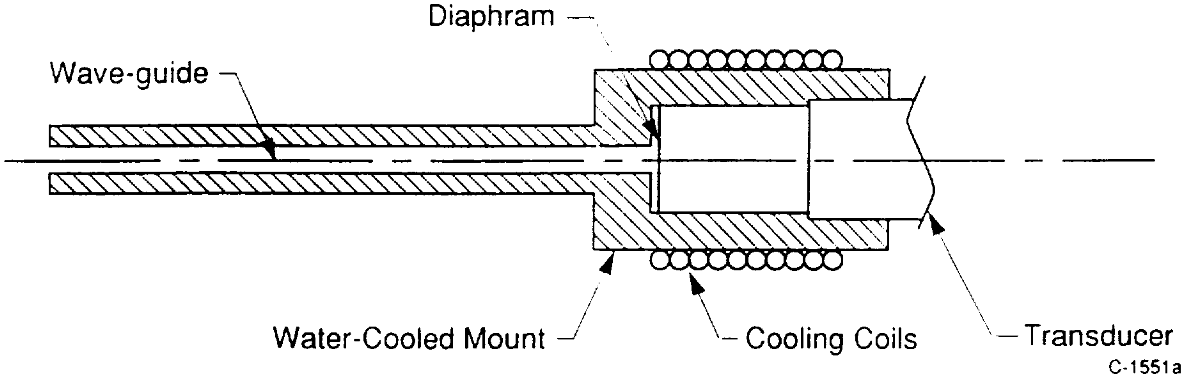

Figure 38. Pressure Transducer Mount Configuration

4.2.1 Heat Transfer Analysis

To predict the temperature field in the transducer mount, a heat transfer analysis was performed. The assumptions used in the present analysis are: a) conduction is the only mode of heat transfer; b) no flow exists in the transducer wave-guide; c) the system is in steady state; and d) cooling fluid (water at 30 C) may be supplied at a sufficient flowrate to maintain an isothermal outer wall. The heat conduction equation may be written as follows:

$$\nabla^2 T + \frac{q}{k} = \frac{1}{\alpha}\frac{\partial T}{\partial t} \quad . \tag{47}$$

After using the simplifying assumptions listed above, we are left with the following equation to solve

$$\nabla^2 T = 0 \quad . \tag{48}$$

Assuming a cylindrical and axisymmetric geometry, this equation takes the following form:

$$\frac{1}{r}\frac{\partial}{\partial r}\left[r\,\frac{\partial T}{\partial r}\right] + \frac{\partial^2 T}{\partial z^2} = 0 \quad . \tag{49}$$

Equation (49) was solved using a finite difference scheme. After replacing the derivatives with central difference expressions and rearranging, we are left with the following expression for the temperature, $T_{i,k}$, at each node on the calculation grid

$$T_{i,k} = \frac{\Delta r^2 \Delta z^2}{2\left(\Delta r^2 + \Delta z^2\right)}\left[\frac{T_{i+1,k}-T_{i-1,k}}{2r_i\,\Delta r} + \frac{1}{\Delta r^2}\left(T_{i+1,k} + T_{i-1,k}\right) + \frac{1}{\Delta z^2}\left(T_{i,k+1} + T_{i,k-1}\right)\right] \quad . \tag{50}$$

Because Eq. (48) is elliptic, boundary conditions must be specified along the entire perimeter of the solution domain to render the problem well posed. Figure 39 shows an example of the calculation grid along with the boundary conditions used. It should be noted that the transducer mount could be modelled as a solid piece due to the steady-state assumption made above. If this assumption had not been made, the differences in thermal conductivity of the gas in the waveguide and that of the waveguide wall would need to be accounted for.

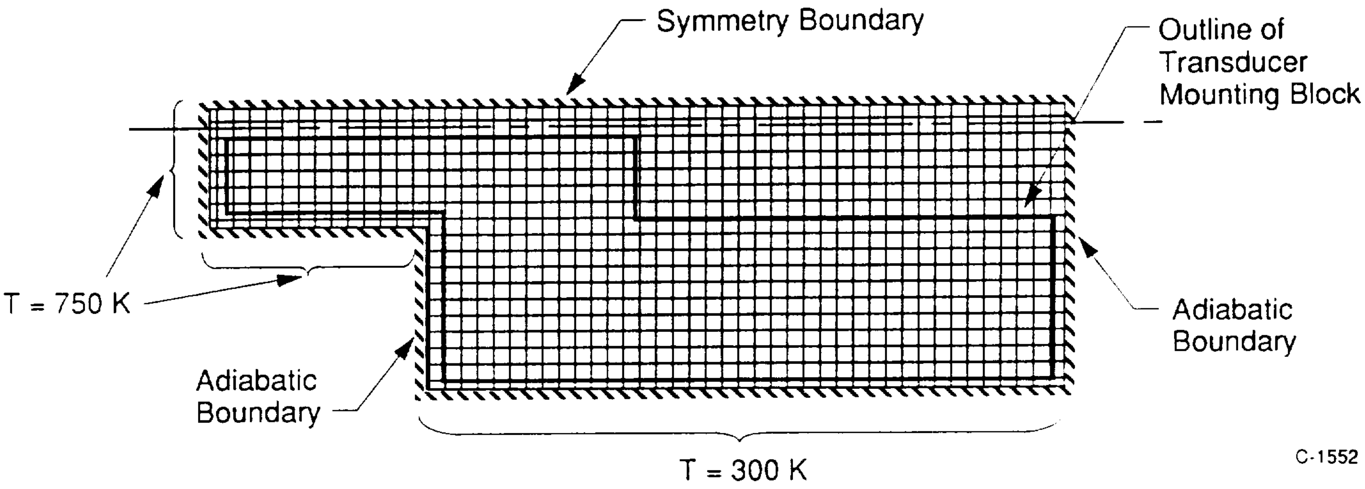

Figure 39. Calculation Domain with Specified Boundary Conditions

Figure 40 shows a series of curves representing the calculated temperature distribution in the transducer mount. Each curve represents the axial temperature profile for a fixed radius. The maximum temperatures in the mount occur along the centerline and it is this profile which dictates the minimum length of the waveguide and standoff distance of the transducer face. Figure 41 shows a drawing of the transducer mount final-design along with pertinent dimensions. It was found that a minimum waveguide length of approximately 1.5 cm was necessary in order that the transducer face be sufficiently isolated from the high-temperature combustion gases.

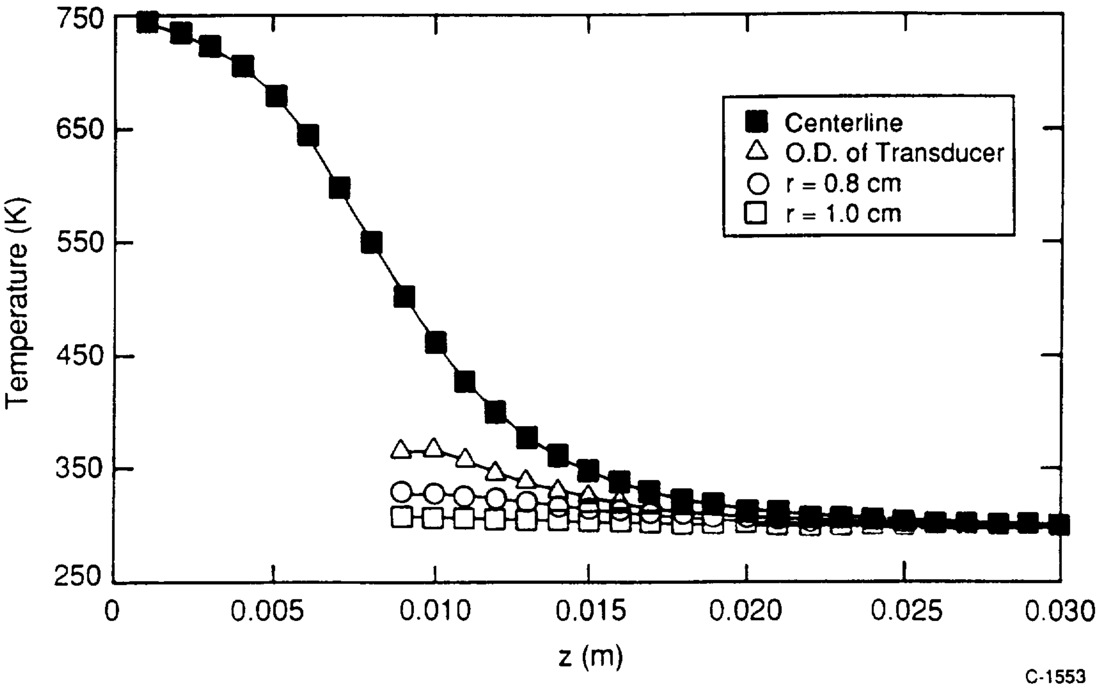

Figure 40. Calculated Temperature Distribution in Transducer Mount

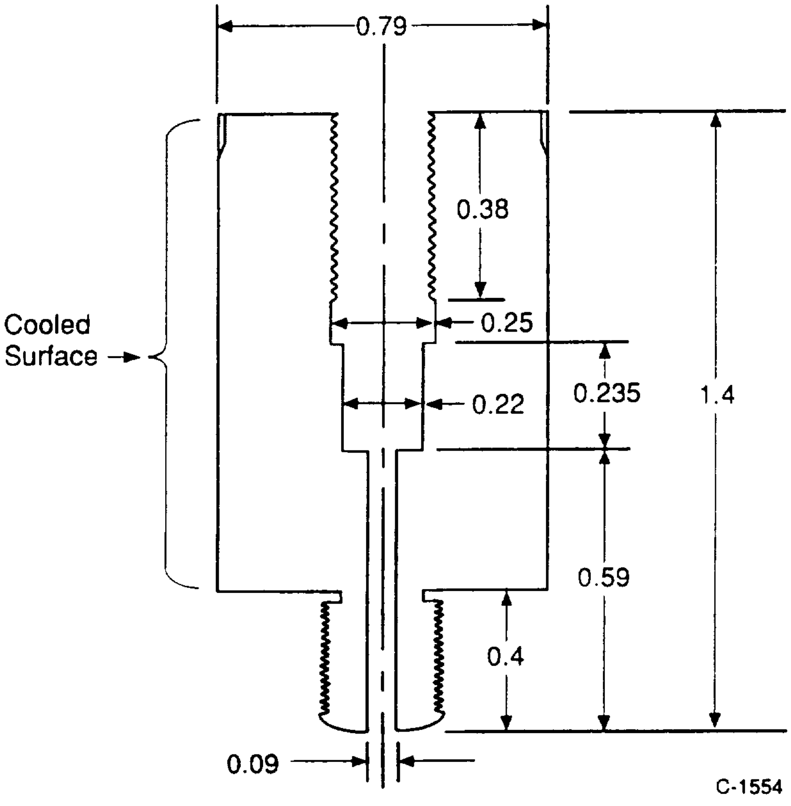

0.79
0.38
0.25
0.235
1.4
0.22
0.59
0.4
0.09
Cooled Surface
C-1554

Figure 41. Transducer Mount - final design (dimensions in inches)

4.2.2 Frequency-Response Analysis

The frequency-response of the transducer mount shown in Figure 41 was predicted using a NASA Lewis supplied computer program. The program solves for the pressure amplitude ratios and phase angles across a series of tube/volume segments for a specified set of excitation frequencies.[24] The equations solved are known as the Bergh and Tijdeman equations[25] and model longitudinal and radial acoustic wave propagation in the system. Attenuation of pressure waves due to viscous damping in the fluid is also modelled and variable fluid thermodynamic properties may be specified.

Figure 42 shows a schematic diagram of the calculation input. The waveguide is modelled as a series of constant property sections and the program allows for a total of ten sections. The program input consists of specification of the segment geometry and the viscosity (μ) and density (ρ) of the fluid in each segment. An accommodation for flexible walls is included in the program; however, this was not used in the present case. Figure 43 shows the predicted frequency response curves for the present transducer mount design with constant thermodynamic properties specified. The density and viscosity specified for this case were those of air at T = 550 K which is near the mean temperature along the centerline of the mount. The amplitude response shows a resonant frequency near 3.8 kHz and a second resonance near 11.4 kHz. It is likely that these frequencies correspond to the quarter-wave and three-quarter-wave modes of the waveguide.

A second calculation was performed with variable properties specified. The properties were based on the calculated centerline temperature profile shown in Figure 40. Figure 44 compares the results from the two frequency response calculations in the vicinity of the predicted quarter-wave resonance. The specification of variable properties in the waveguide causes an increase in the resonant frequency (approximately 15%) thus a small improvement in the frequency response of the system for the low-frequency range (dc - 4 kHz).

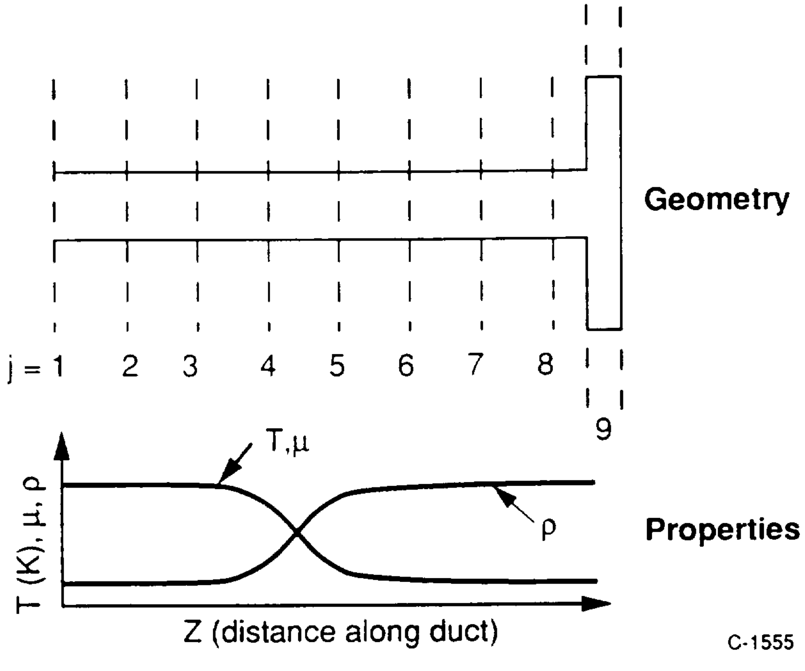

Figure 42. Schematic Diagram of Frequency-Response Calculation Input

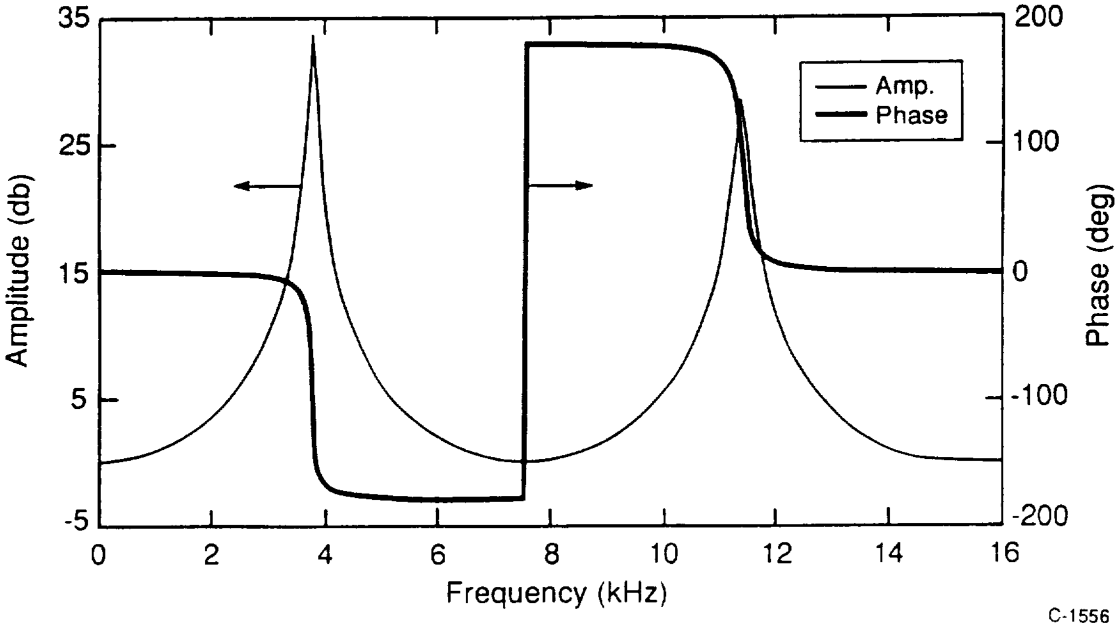

Figure 43. Frequency-Response of Transducer Assembly with Constant Thermodynamic Properties ($T(z)$ = const = 550 K, P_{avg} = 100 psi)

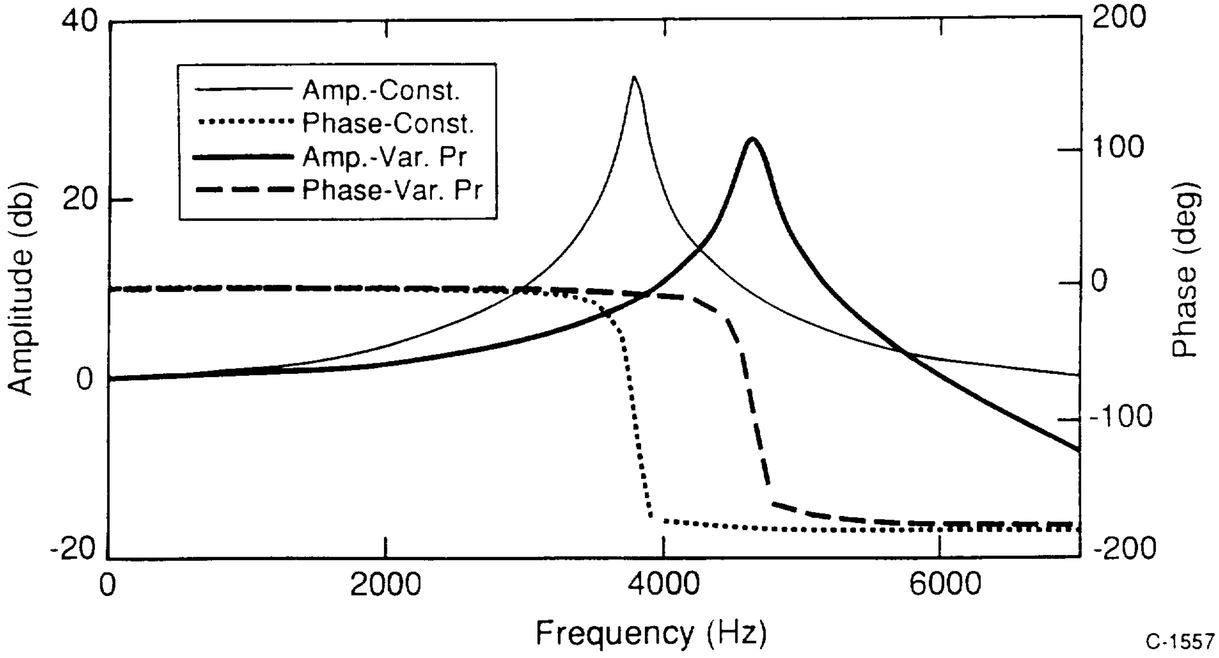

Figure 44. Calculated Frequency-Response for Isothermal ($T = 550$ K) and Variable Properties Cases

This variable frequency response was not a barrier to the present application. We used the pressure fluctuation spectra only in qualitative sense, i.e., to identify the approximate frequency of observed resonances. The most likely instability mode of the combustor was the fundamental half-wave longitudinal mode, which we estimated to be at about 2500 Hz. This mode would be clearly visible, if excited, in the output of the transducer. The next order longitudinal mode will be near 5000 Hz, again visible, although embedded among the resonances of the mount. The fundamental tangential mode should be at about 5500 Hz while the fundamental transverse mode is above 11,000 Hz. In actual implementation, no substantial peaks in the fluctuation spectra were observed.

This section has described the procedures used to design the supersonic burner test-bed facility. As described in more detail in Section 6, the burner performed excellently throughout the program. Stable combustion was achieved at the design pressure of 100 psi for extended periods (typically ~30 minutes). No significant instabilities were recorded either by the pressure transducer or by PLIF imaging of the OH distribution in the jet exhaust. Initial measurements of the OH concentration in the exhaust flow indicated that the exhaust temperature was lower than desired due to overly efficient cooling of the burner wall. A simple modification consisting of inserting a 2″ diameter alumina tube wrapped with zirconia felt inside the combustor plenum alleviated this problem. This modification and the jet flow conditions achieved during the program are described in Section 5.

5. JET FLOW MODELLING AND CHARACTERIZATION EXPERIMENTS

The underexpanded exhaust jet flow from the high-pressure burner formed the principal test flow for all of the imaging velocimeter development testing. This test flow was chosen, in part, because of its wide range of thermodynamic flow properties within a few jet diameters and because of the large body of literature regarding experimental and analytical studies of similar jets. This section presents the results of a detailed literature search of the overall structure, or topology, of the underexpanded jet flowfield. These results were used to predict the baseline operational characteristics of the burner and, initially, provide a standard for comparison to the velocity measurements. During the course of the program, however, PSI acquired the capability of modelling the mean axisymmetric flowfield using the NASA Langley SPARK code. These results are discussed in detail in Subsection 5.3.

5.1 Flow Topology

The flowfield structure in the near-field of an underexpanded supersonic jet is shown schematically in Figure 45. In the underexpanded case, the jet Mach number, M_e, at the nozzle exit is greater than or equal to one and the static pressure, P_e, is greater than the ambient pressure, P_a. The ratio of P_e and P_a is called the nozzle exit pressure ratio, P_r, and is useful in describing different flow regimes. As the flow emerges from the nozzle it begins to expand and accelerate into the ambient region due to the mismatch in static pressure between the nozzle exit and the atmosphere. The formation of an expansion fan occurs near the nozzle lip and this fan propagates across the jet axis and toward the external jet boundary where it is reflected back towards the jet flow as a series of compression waves. These compression waves coalesce near the periphery of the supersonic core flow in the form of a barrel, hence the name barrel shock. When the nozzle exit pressure ratio is sufficiently large ($P_r \geq 2$), the barrel shock culminates in a normal shock, called a Mach disc, and a reflected shock. The intersection of the barrel shock, Mach disk, and reflected shock is called the triple point.

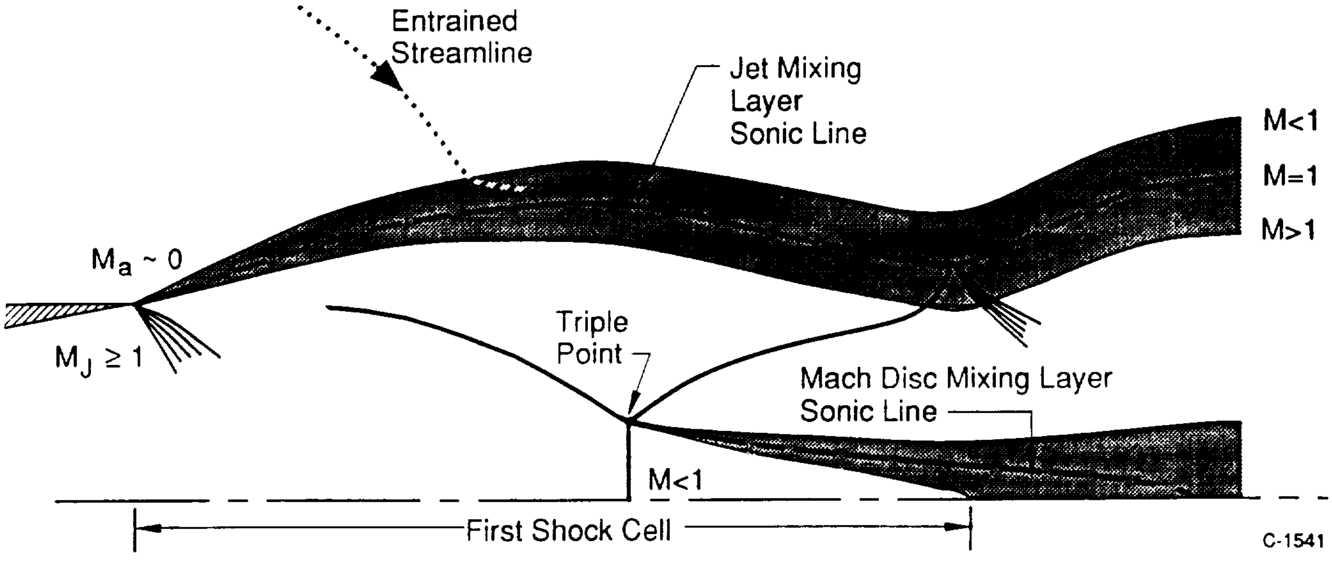

Figure 45. Diagram Showing Flow Topology of an Underexpanded Sonic Jet (from Ref. 26)

The flow immediately downstream of the Mach disc is subsonic whereas the flow downstream of the oblique reflected shock is supersonic. This results in the formation of a shear layer between these two flow streams whose velocities are eventually equilibrated through momentum transfer. With a sufficiently high nozzle exit pressure ratio, the processes leading to Mach disc formation may be repeated. Ewan and Moodie[24] found that only one Mach disc formed for isothermal air jets with $3 \leq P_r \leq 14$. In any case, the pressure mismatch between the jet flow and the ambient is eventually equilibrated through successive oblique expansion and compression waves which form a diamond shaped pattern along the jet axis in the potential core region. Following the dissipation of the diamond shock structure, the jet's radial velocity profile passes through a transition region and then reaches a fully developed state where the profile is self-similar and approximately Gaussian. The centerline velocity in the fully developed region may be described by a decaying exponential function.

Key geometric parameters in the description of the underexpanded jet flow include the nozzle exit diameter, D_e, the length of the barrel shock (distance from the nozzle exit to the Mach disc), L_b, and the Mach disc diameter, D_m. A number of authors have attempted to correlate L_b and D_m with D_e and the nozzle exit pressure ratio, P_r (Refs. 27-29). The resulting expressions are as follows:

$$L_b = 0.77\ D_e + 0.068\ D_e^{1.35}\ Pr\ ;\ D_m \simeq 0.65\ D_e \tag{51}$$

$$L_b = 0.64\ D_e Pr^{1/2}\quad ;\quad D_m \simeq 0.6 \text{ to } 0.8\ D_e \tag{52}$$

$$L_b = 0.67\ D_e Pr^{1/2}\quad . \tag{53}$$

The first correlation shown is based on a curve fit to isothermal air-jet data for the pressure ratio range $3 \leq P_r \leq 14$. The second and third are based on a collection of experimental data from both isothermal and heated jet conditions and for $10 \leq P_r \leq 10^5$. Evaluating the above expressions at the nominal operating conditions of the PSI supersonic jet facility ($P_o = 6.8$ atm; $P_e = 3.8$ atm; $P_a = 1$ atm; $D_e = 5$ mm) yields values of $L_b = 6.1$, 8.4, and 8.7 mm, respectively. Values for the Mach disc diameter are approximately the same for the two available correlations with $D_m \simeq 3$ mm.

Relations (52) and (53) were considered the most appropriate since they covered the largest range of available data. The primary purpose for these estimates was for setting up the grid spacing for the SPARK code calculation (the grids were more finely distributed in the vicinity of the Mach disk in order to accurately capture the shock location). Further, these estimates are used below to predict first-order conditions for the Mach number and other property variations along the jet centerline.

Fox[30] has studied the variation of the primary wavelength of the shock cell spacing, ω, with nozzle exit pressure ratio. Although his published results concern nozzle exit Mach numbers, M_e, between 2 and 3 (compared to the present case where $M_e \simeq 1$), an extrapolation of his results suggest that $\omega \approx 2$ for the present case.

5.2 Centerline Profiles

The flow conditions and thermodynamic properties along the centerline of the supersonic jet may vary substantially in comparison to its subsonic counterpart. Figure 46 is a computation of the static pressure variation in the jet near-field for an underexpanded jet with $M_e = 2$ and $P_r = 5$. In the calculation, the pressure drops from 5 atm to less than 0.1 atm in a distance of about 4 D_j, which corresponds to the location of the Mach disc. Following the normal shock, there is a pressure rise and then a decaying oscillation of the static pressure about the ambient value. The wavelength of the oscillation corresponds to the shock-cell spacing and may be approximated by the primary wavelength, ω, defined above. Because the example in Figure 46 was taken from a calculation scheme which has not been validated for the given conditions, it should be used for qualitative purposes only (However, L_b and ω agree very well with the data presented in Ref. 30).

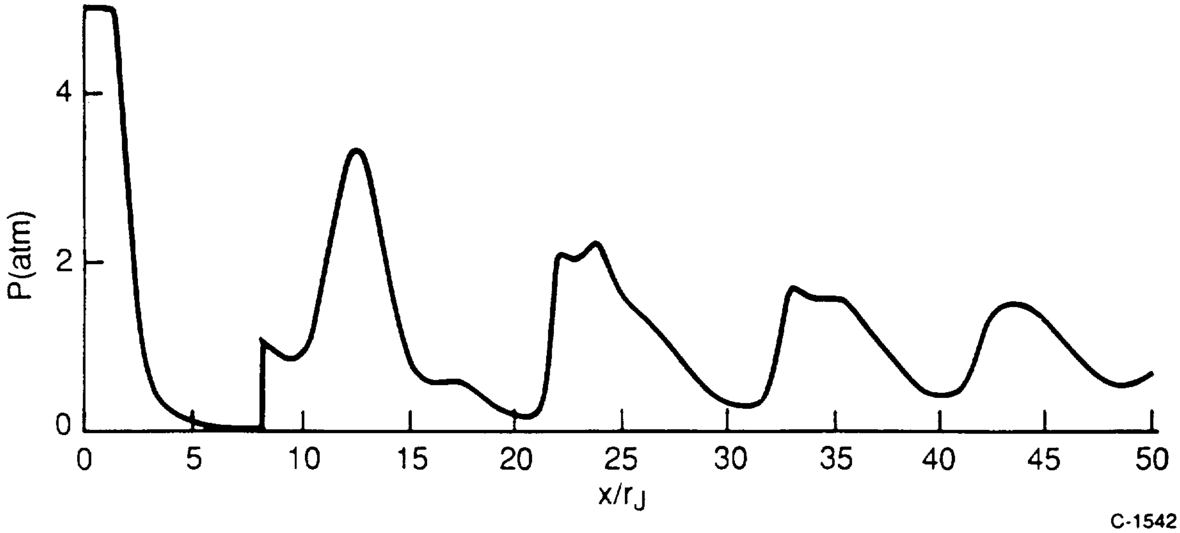

Figure 46. Example of Centerline Static Pressure Variation for an Underexpanded Sonic Jet (from Ref. 31)

The initial expansion of the gas which occurs upstream of the Mach disc may be modelled as being isentropic. Therefore, the following relations describe the static temperature and pressure as a function of Mach number and stagnation values:

$$\frac{T_o}{T} = 1 + \frac{\gamma-1}{2} M^2 \tag{54}$$

$$\frac{P_o}{P} = \left[1 + \frac{\gamma-1}{2} M^2\right]^{\frac{\gamma}{\gamma-1}} . \tag{55}$$

Furthermore, Askenas and Sherman[29] give a correlation for the jet centerline Mach number as a function of the ratio of specific heats, γ, and streamwise distance from the nozzle exit, x:

$$M(x) = A\left[\frac{x}{d_o} - \frac{x_o}{d_o}\right] - \frac{1}{2A}\,\frac{\gamma+1}{\gamma-1}\left[\frac{x}{d_o} - \frac{x_o}{d_o}\right]^{1-\gamma} + \frac{0.73}{A}\left[\frac{x}{d_o} - \frac{x_o}{d_o}\right]^{-\left(\frac{\gamma+1}{2}\right)} \tag{56}$$

where x_0 is the jet virtual origin and A is a constant equal to 4.17 for the present case.[30] Using Eqs. (54) through (56), M(x), p(x), T(x) and U(x) may be calculated for the present conditions and the result is shown in Figure 47. The maximum jet Mach number upstream of the Mach disc, M_1, may be deduced from Figure 47 along with the known value of L_b. Using the maximum and minimum values of L_b computed from Eqs. (51) through (53) yields values for M_1 of 2.3 and 3.0.

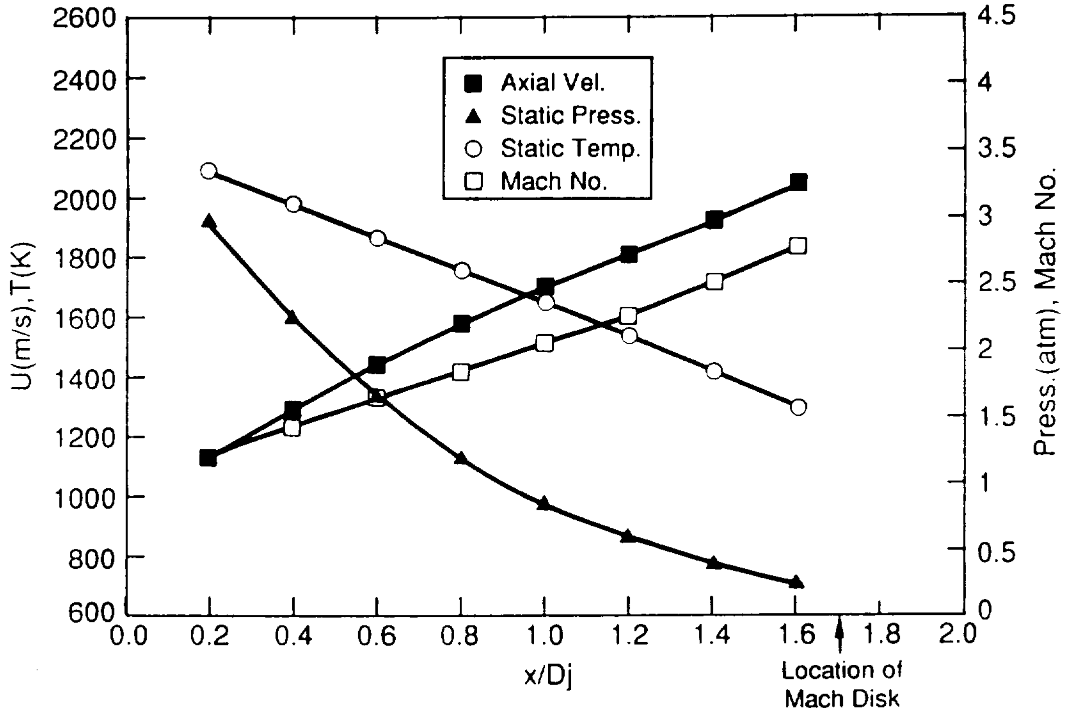

Figure 47. Variation of Centerline Properties in Regions of Isentropic Expansion.

Hiller[33] suggests another method to estimate M_1 which is based on the assumption that the static pressure just behind the Mach disc is twice the ambient value. Then using Eq. (55) along with the equation describing the strength of a normal shock:

$$\frac{P_2}{P_1} = 1 + \frac{2\gamma}{\gamma+1}\left(M^2\sin^2\alpha-1\right) \quad , \tag{57}$$

M_1 may be calculated and this leads to $M_1 = 2.7$ for the present conditions. From experimental data, Hiller found this calculation technique to give a lower limit on M_1 and because of this felt that the value of $M_1 = 2.3$ deduced from Eq. (51) was too low.

The actual jet Mach number is best determined by measuring the location of the Mach disc, using a visualization technique such as Schlieren photography or PLIF, then solving for M_1 using Eq. (56). Following this, the static pressure and temperature on both sides of the Mach disc may be computed using Eqs. (54), (55), and (57) provided that the reservoir conditions are known.

5.3 Jet Flow Simulations Using SPARK

5.3.1 Introduction to Jet Flow Simulations

The flowfields in the near field of underexpanded supersonic jets are multi-dimensional and generally complex. In order to understand these flowfields better and provide points of comparison for the PLIF images generated during the experimental part of the program, computational studies of the jet flows were performed using the SPARK Code.[34,35] This code solves the compressible, Reynolds-averaged, Navier-Stokes equations including finite-rate chemistry for the important gas species found in these high temperature jets. Although other studies[36] of underexpanded jets have been undertaken using the SPARK Code, they have emphasized the very near field encompassing the Mach disk only. The current effort includes the Mach disk flow as well as several shock cells downstream of the Mach disk. This extended flowfield proved to be rather challenging due to the mixed subsonic-supersonic flow in the outflow plane of the computational domain. The ultimate results of the computational effort provide new calculations for extended underexpanded jet flowfields. They compare well with the experimental measurements.

5.3.2 SPARK Code

The SPARK Code has a fourteen year history that began with the TWODLE[37] Code developed by Drummond at NASA-Langley Research Center. This code utilized MacCormack's explicit algorithm[38] to solve the 2-D Navier-Stokes equations for internal flow applications using equilibrium H_2-air chemistry. TWODLE was extended to include finite-rate chemistry by Drummond in subsequent years. The new code was called SPARK[34] since it could now handle combustion problems with heat release effects. Transport models for turbulence and species binary diffusion were also incorporated into the code. Specific application to a hydrogen-air mixing layer were well described in Ref. 34 where the finite-difference results were compared to a spectral technique. Although a detailed theoretical or users manual for the SPARK code does not currently exist, the mixing layer study[34] provides the most extensive information of the code and serves as a pseudo manual. The extension[35] of the SPARK Code to three dimensions was performed by Carpenter who improved the finite-difference algorithm by making it fourth-order compact. The three-dimensional code has been, and is currently, a very valuable tool for "real" combustor designs and supersonic combustion applications. Not surprisingly, primary users of the SPARK family of codes reside at NASA Langley. There are also many versions of SPARK being used in industry and at universities. Numerous application studies using SPARK[39-43] continue to appear in the literature.

The specific capability of the SPARK Code is summarized in Table 1. All of these capabilities, except the last two turbulence models, are part of the SPARK code version that is currently in operation at PSI. The numerical finite difference techniques employed in SPARK are implicit with specific emphasis on the implicit treatment of the chemical source term. Solutions are spatially second-order accurate utilizing a prediction-corrector scheme. Time-accurate as well as time asymptotic simulations can be performed using the SPARK code. Furthermore, an extensive set of numerical control parameters can also be exploited to optimize solution convergence.

5.3.3 Application of SPARK to Jet Flowfield

In order to apply the SPARK Code to any flowfield, several subroutines must be modified to suit the flow of interest as outlined in Table 2. As might be expected, the MAIN subroutine controls the simulation with the specification of both the physical and numerical parameters. In addition, one must input initial conditions for all the independent flow variables (U, V, T, p and f_n) where U is the velocity in the x-direction, V is the velocity in the y-direction, or the r-direction for the axisymmetric version of the SPARK

Table 2. SPARK Code Capability

Equations Solved	Navier-Stokes, energy, species continuity
Thermodynamics Model	Real gas
Chemistry Model	Equilibrium or Finite-rate
Transport and Diffusion Models	Sutherland viscosity, thermal conductivity Chapman and Cowling binary diffusion
Turbulent Transport	Mixing length Baldwin-Lomax Eggers jet turbulence Advanced models (k-ϵ, PDF)

Table 3. Primary SPARK Subroutines

Subroutine	Purpose
MAIN	Define physical and numerical calculation parameters as well as initial conditions
BC	Set boundary conditions around the entire flow domain
GEOM	Specify the geometric extent of the flow domain
PROPN	Specify the thermodynamic and kinetic rate properties for the gas species in the flow problem
TRAN	Specify the location of the grid-point locations

Code that is being used in the present application. In addition, T is the gas temperature, p is the pressure and the f_n's are the n gas specie mass fractions.

The flow domain is specified in subroutine GEOM. For the underexpanded jet flow, an axially-symmetric flowfield is assumed. Consequently, only one-half of the entire flow domain requires numerical solution. The geometric specification of the supersonic jet problem is shown in Figure 48. The domain is 7.5 mm in height and 30 mm in length. Furthermore, the jet flow source is 2.5 mm in width as shown in the figure.

The grid point distribution within the flow domain is specified in the subroutine TRAN. Grid point concentration is used on both x and r directions. In the streamwise direction, the primary grid-point concentration is analytically specified in the vicinity of the Mach disk location and in the radial direction grid points are concentrated in the viscous jet region using an exponential relationship.[44] All of the grid points are illustrated in Figure 49. In total there are 40 grid points radially and 95 grid points in the axial direction.

The thermodynamics and kinetics for a nine-species, high-temperature, hydrogen-air mixture is incorporated into the PROPN subroutine. The thermodynamics information is standard and doesn't require any additional comment. The kinetic-rate equations employed in this subroutine were developed during the course of the study.

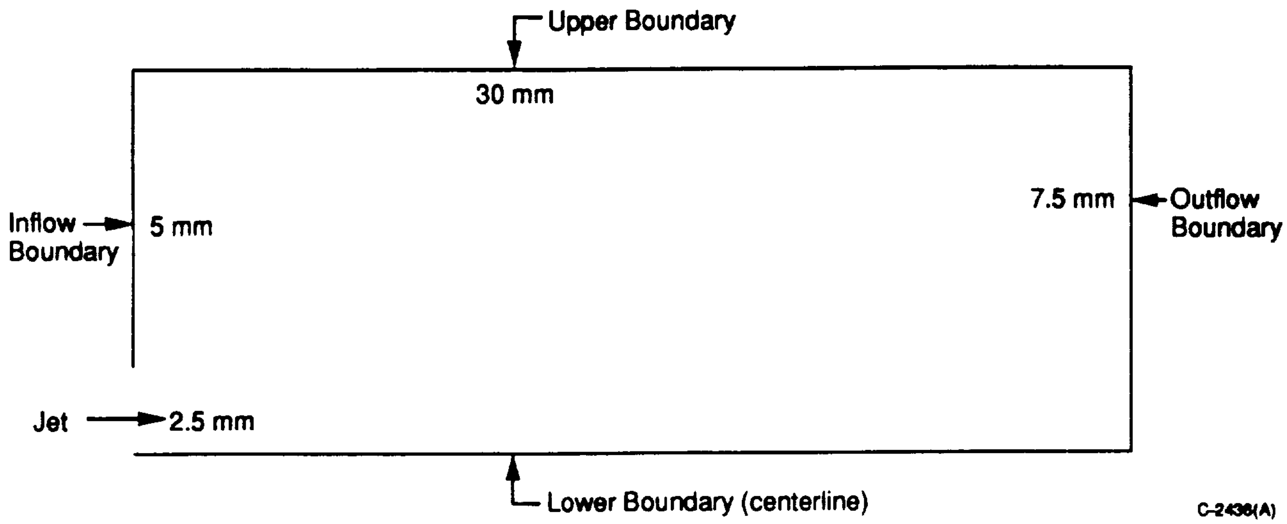
Upper Boundary
30 mm
Inflow Boundary
5 mm
7.5 mm
Outflow Boundary
Jet
2.5 mm
Lower Boundary (centerline)
C-2436(A)

Figure 48. Flow Domain for Underexpanded Supersonic Jet

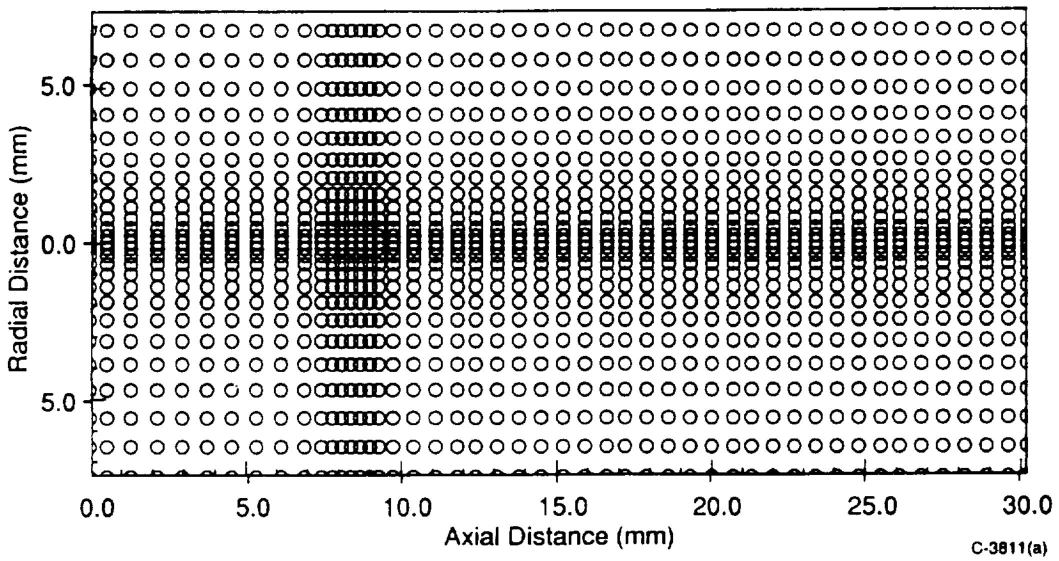

Figure 49. Grid Point Distribution for Every 3rd in X and Every other in Y

Initially, we retained the 18-equation H_2-O_2 chemistry model developed by Drummond[34] that was present in the original code. That model is summarized in Table 3. The reaction rate variables apply to the modified Arrhenius form for the forward reaction rate coefficient:

$$k = AT^n \exp(-E/RT) \tag{58}$$

Nitrogen was carried along as a passive scalar for this model.

Since the laboratory experiments use air rather than O_2, we developed a reduced reaction mechanism for H_2 air chemistry based on consideration of more extensive mechanisms in the literature[45,46] and the flow

Table 4. 18 Equation H_2-O_2 Chemistry Model

No.	Reaction	Reaction Rate Variables		
		A (cm^3/mole/s)	n	E(cal/gmole)
1	$H_2 + O_2 = OH + OH$	0.170×10^{14}	0	48,150
2	$H + O_2 = OH + O$	0.142×10^{15}	0	16,400
3	$OH + H_2 = H_2O + H$	0.316×10^{8}	1.8	3,030
4	$O + H_2 = OH + H$	0.207×10^{15}	0	13,750
5	$OH + OH = H_2O + O$	0.550×10^{14}	0	7,000
6	$H + OH + M = H_2O + M$	0.221×10^{23}	-2.0	0
7	$H + H + M = H_2 + M$	0.653×10^{18}	-1.0	0
8	$H + O_2 + M = HO_2 + M$	0.32×10^{19}	-1.0	0
9	$HO_2 + OH = H_2O + O_2$	0.5×10^{14}	0	1,000
10	$HO_2 + H = H_2 + O_2$	0.253×10^{14}	0	700
11	$HO_2 + H = OH + OH$	0.199×10^{15}	0	1,800
12	$HO_2 + O = OH + O_2$	0.5×10^{14}	0	1,000
13	$HO_2 + HO_2 = H_2O_2 + H$	0.199×10^{13}	0	0
14	$HO_2 + H_2 = H_2O_2 + H$	0.301×10^{12}	0	18,700
15	$H_2O_2 + OH = HO_2 + H_2O$	0.102×10^{14}	0	1,900
16	$H_2O_2 + H = OH + H_2O$	0.5×10^{15}	0	10,000
17	$H_2O_2 + O = OH + HO_2$	0.199×10^{14}	0	5,900
18	$M + H_2O_2 = OH + OH + M$	0.121×10^{18}	0	45,500

residence times involved. Considerable simplification occurs by neglecting the ignition part of the problem. This is reasonable for our flow since the exhaust flow consists of combustion products of stoichiometric or fuel-lean mixtures. The reaction rate variables for this reduced set are given in Table 4.

The discussion of the boundary conditions (subroutine BC) has been reserved for last in this subsection. It is one of the more critical aspects of any flow simulation code, but for the current application the mixed subsonic-supersonic outflow boundary conditions is an integral part of the solution technique. The reasons for this will be developed below. The individual boundary conditions pertaining to the flow domain illustrated in Figure 48 will be described in turn. We begin with the symmetry conditions at the axis. There are two ways to implement axis of symmetry boundary conditions. One way is to set the radial velocity equal to zero along the axis at $j = 1$ and set all the radial derivatives of the other flow variables equal to zero. This is implemented by setting, e.g.,

$$U(i,j=1) = U(i,j=2) \qquad (59)$$

Table 5. Reduced H_2-Air Chemistry Model

No.	Reaction	Reaction Rate Variables		
		A (cm^3/mole/s)	n	E(cal/gmole)
1	$H_2 + O_2 = OH + OH$	5.5×10^{13}	0	57,800
2	$H + O_2 = OH + O$	1.2×10^{17}	-0.91	16,500
3	$OH + H_2 = H_2O + H$	1×10^{8}	1.6	3,030
4	$O + H_2 = OH + H$	1.5×10^{7}	2.0	7,550
5	$OH + OH = H_2O + O$	3.4×10^{13}	0	5,020
6	$H_2O + H + OH = H_2O + H_2O$	1.4×10^{23}	-2.0	0
7	$N_2 + H + OH = H_2O + N_2$	2.2×10^{22}	-2.0	0
8	$H_2 + H_2O = H + H + H_2O$	3.3×10^{15}	0	96,000
9	$NO_2 + M = NO + O + M$	2×10^{16}	0	65,600
10	$NO_2 + H = NO + OH$	3.47×10^{14}	0	1,470

for the x-direction velocity. A second, more attractive way of implementing the boundary condition, is to reflect variables across the axis. This is accomplished by defining a grid location a small distance δ below the axis (j=1) as well as another grid location precisely δ above the axis (j=2). Then, all the flow variables except the v-velocity will have the same condition as given by Eq. (59). The v-velocity will now have the reflection condition:

$$v(i,j=2) = -v(i,j=1) \tag{60}$$

Both forms of the axis conditions were used during the course of the study with the reflection condition being preferable.

The next boundary condition, as we proceed in a clockwise direction around the domain, is the inflow condition. The sonic jet enters the domain between the axis and 2.5 mm above the axis as shown in Figure 48. Three different sonic jet conditions were used during the course of the study. They are summarized in Table 5. In order to control instabilities that traverse the domain in the x-direction, a slow subsonic co-flow is used in the inviscid flow parallel to the jet flow. Prof. Haj-Hariri of the University of Virginia has utilized this co-flow technique[47] in similar applications. The conditions for the co-flow are specified in Table 6. Although there is some limited influence of the co-flow on the overall underexpanded jet flowfield, the basic features of the flow remain unchanged as illustrated in the next subsection.

The boundary conditions on the upper so-called "infinity" boundary are the easiest to implement. In order to insure that no mass is lost through this boundary, all the derivatives in the normal direction of the flow variables are set equal to zero.

The most significant boundary condition to specify for the underexpanded jet is the outflow condition. The primary reason for the criticality of this condition is that the flow is a mixed subsonic/supersonic flow at

Table 6. Sonic Jet Inflow Conditions

	Baseline Case	High Pressure Case	High Temperature Case
Flow Variables			
U (m/s)	926.0	882.5	971.2
p (atm)	3.8	4.0	4.0
T (K)	2050	1855	2240
Species Mass Fractions			
f_1 [H_2]	1.956×10^{-4}	0.491×10^{-6}	1.669×10^{-4}
f_2 [O_2]	1.261×10^{-3}	2.607×10^{-2}	3.175×10^{-2}
f_3 [H_2O]	0.2528	0.2439	0.3142
f_4 [OH]	6.188×10^{-4}	4.668×10^{-4}	3.456×10^{-3}
f_5 [H]	2.318×10^{-6}	1.161×10^{-7}	6.582×10^{-6}
f_6 [O]	1.005×10^{-5}	9.185×10^{-6}	1.778×10^{-4}
f_7 [NO]	0.0	1.791×10^{-3}	5.138×10^{-3}
f_8 [NO_2]	0.0	3.619×10^{-5}	5.895×10^{-6}
f_9 [N_2]	0.7451	0.7277	0.6451

Table 7. Co-flow Inflow Conditions

Variables	Parameter Values
U (m/s)	34.8
p (atm)	1.0
T (K)	300.0
f_2 [O_2]	0.2221
f_9 [N_2]	0.7779

the outflow exit plane. Consequently, a condition appropriate to either a subsonic or a supersonic flow would be inappropriate, i.e., neither a fixed pressure level appropriate to a subsonic flow nor an extrapolation of the pressure appropriate to a supersonic flow can be employed. This dilemma is resolved by developing a boundary condition algorithm that computes the local Mach number at every grid point on the outflow boundary. Wherever $M < 1$, a subsonic condition is applied but wherever $M \geq 1$, a supersonic condition is used. The implementation of the mixed boundary condition is best described with the help of Figure 50. One starts at the centerline of the jet and begins to calculate the Mach number. Near the axis, the flow will most likely be subsonic. Eventually, as one gets far enough from the axis, the flow just becomes supersonic. If the corresponding pressure is called p_1^{ss}, then for the subsonic grid points, one sets $p = p_1^{ss}$. For the grid points where $M \geq 1$, extrapolation is employed. The flow again becomes subsonic near the top of the domain. In this region one sets the pressure equal to the atmospheric pressure which prevails above the viscous jet. Other provisions associated with this algorithm are as follows: (1) prior to the flowfield becoming supersonic at the outflow boundary, use $p = 1$ atm as the boundary condition; (2) several regions of embedded supersonic flow are also accommodated in the algorithm.

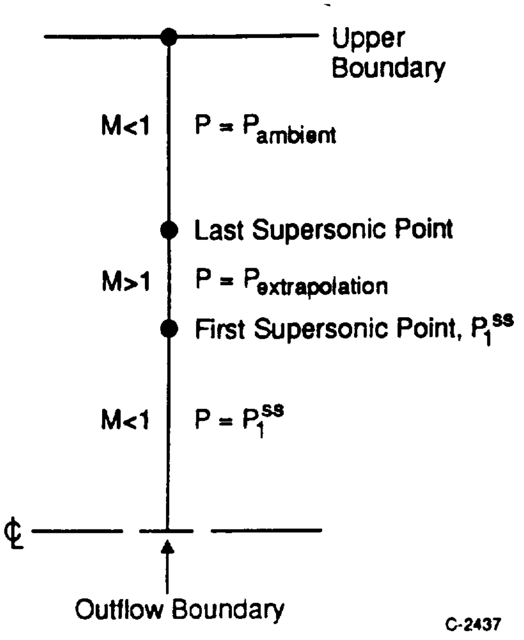

Figure 50. Outflow pressure boundary condition

During the course of this study variants of these conditions were also employed in order to assess the dependence of the simulated flow on the selected boundary conditions. Some of these results are discussed in the next subsection.

5.3.4 Simulation Results

Underexpanded jet simulations are presented for the primary jet conditions of interest to the experimental program. The most important flow variables from the point of view of the experimental effort are the U and V velocity components. The most useful variables from an overall flowfield view are the Mach number and the pressure. The temperature is also available as a flowfield diagnostic. Furthermore, the mass fractions of the gas species are also calculated at every grid point location.

Perhaps the best way to initiate the description of the simulations is to display results along the centerline of the jet. In Figure 51, the pressure, temperature and velocity is shown as a function of axial distance. This figure clearly reveals the smooth variations upstream of the Mach disk, the jumps at the Mach disk and the subsequent shock-cell variations. Consider for example the curve for the pressure variation normalized to the jet source flow pressure of 4 atm. Upstream of the Mach disk there is a rapid decrease of pressure due to the nearly isentropic expansion of the flow. At the Mach disk the pressure "jumps" to a value in excess of the ambient pressure (0.25 in normalized variables). Subsequent to the Mach disk region, the pressure oscillates about the ambient conditions within the two shock cells. The temperature possesses similar characteristics, and the streamwise (U) velocity behaves in the expected manner.

The corresponding contour plots for the flow variables are shown in Figures 52 through 55. The Mach number variation for the high pressure case (Table 5) is shown in Figure 52. Just in front of the Mach disk, the flow has accelerated to a Mach number in excess of 3 and immediately downstream it decelerates to a low subsonic flow with a Mach number of about 0.3. The location of the Mach disk is at 9 mm from the jet exit. The corresponding pressure variations are given in Figure 53. Note the three diamond-like pressure zones downstream of the Mach disk. It took many iterations before the flow relaxed to this "organized"

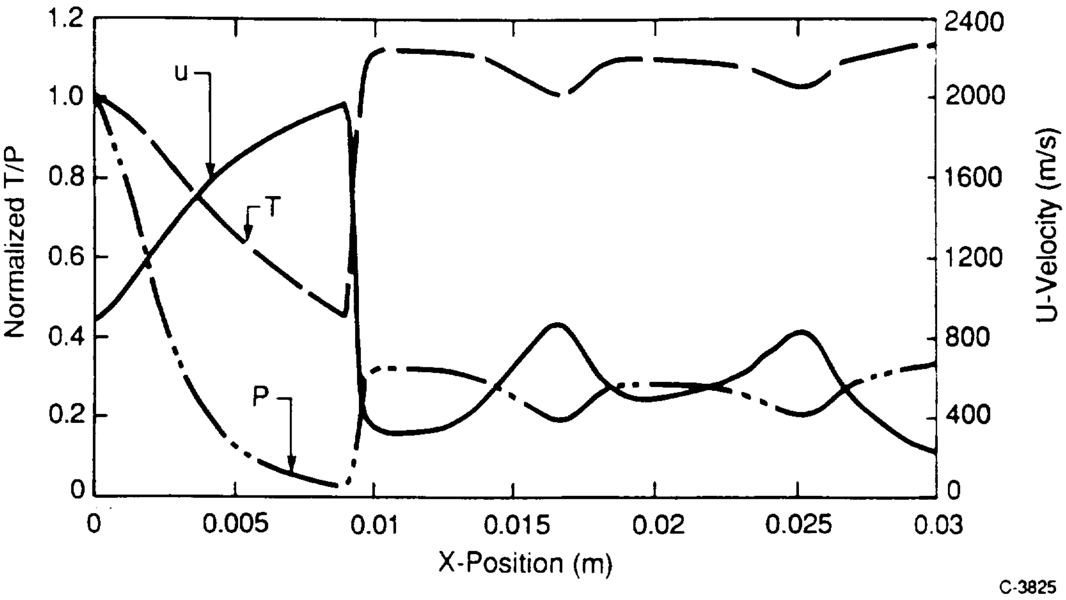

Figure 51. Centerline Flowfield Values for High Pressure Case

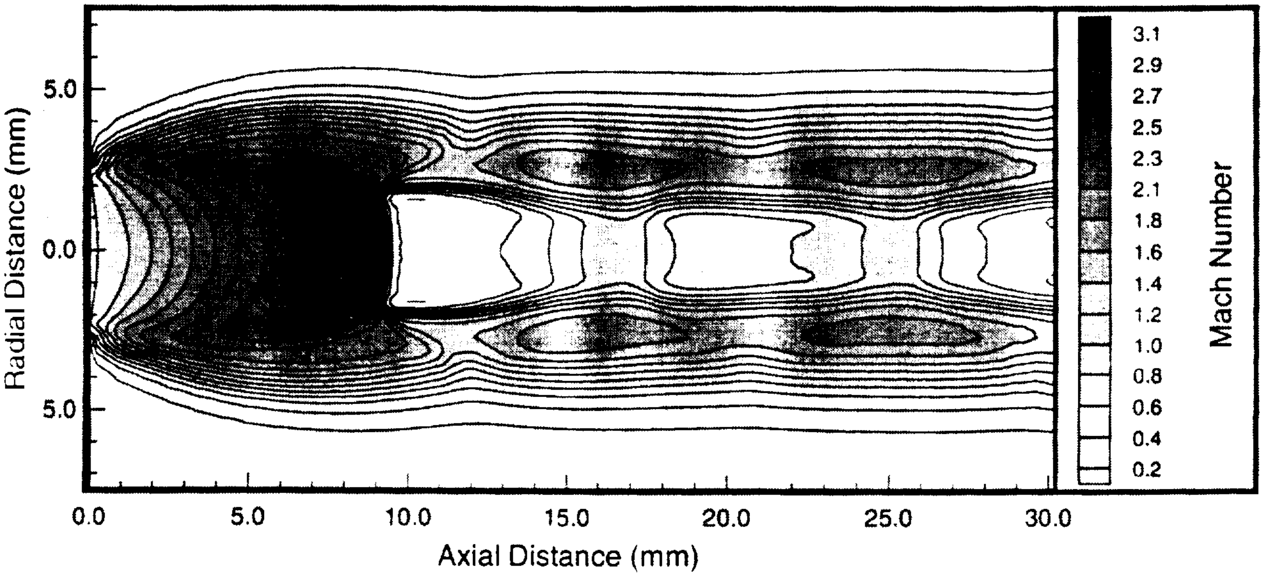

Figure 52. Mach Number for High Pressure Case

structure. The convergence history of the initial supersonic pressure p_1^{ss} at the outflow boundary is shown for the last twenty thousand steps in Figure 56. It has locked in at a value of 1.6 atm for the flow domain of interest. The temperature contours are given in Figure 54. Rapid cooling during the isentropic expansion is followed by a temperature "jump" downstream of the Mach disk and an elevated temperature that doesn't vary very much (see also Figure 51). The fact that the temperature doesn't change much behind the Mach

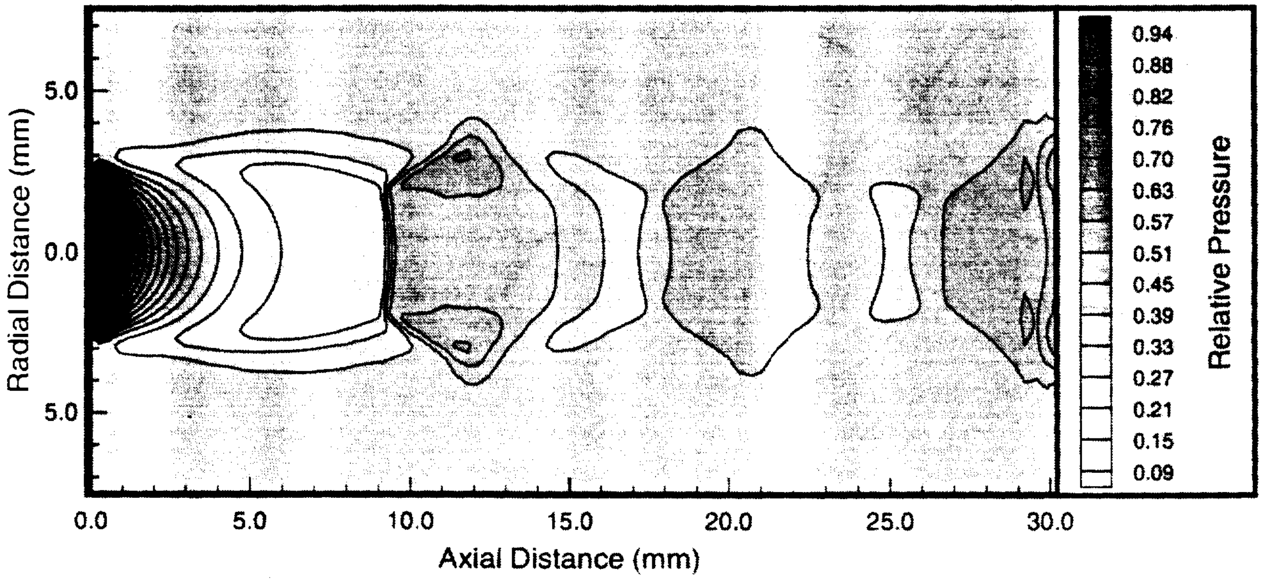

Figure 53. Pressure for High Pressure Case

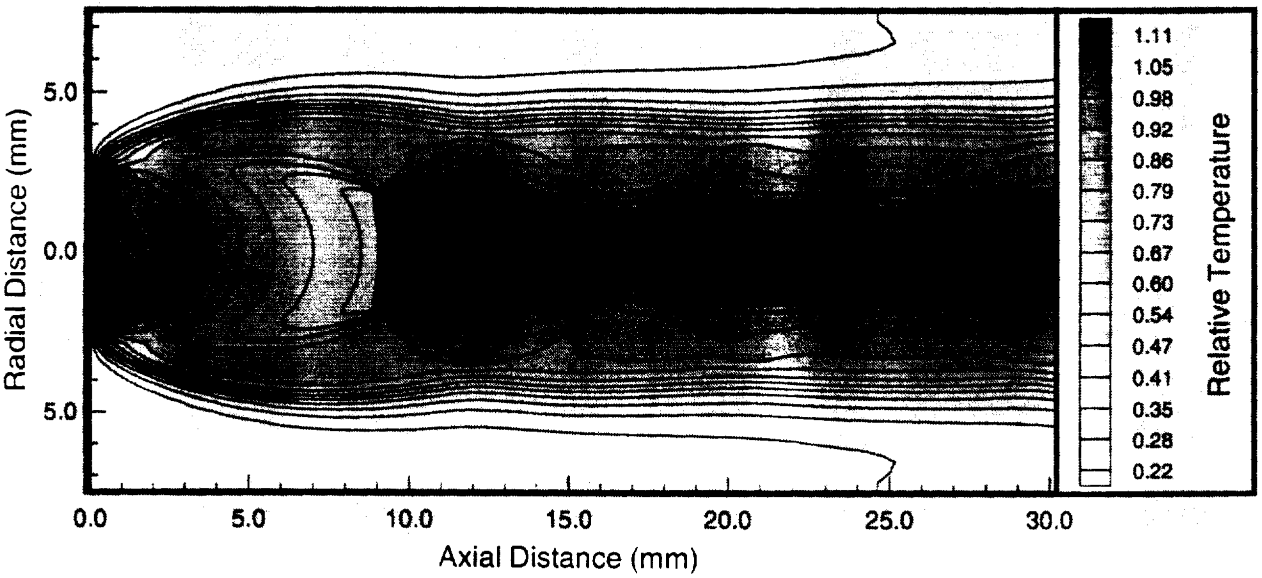

Figure 54. Temperature Contours for High Pressure Case

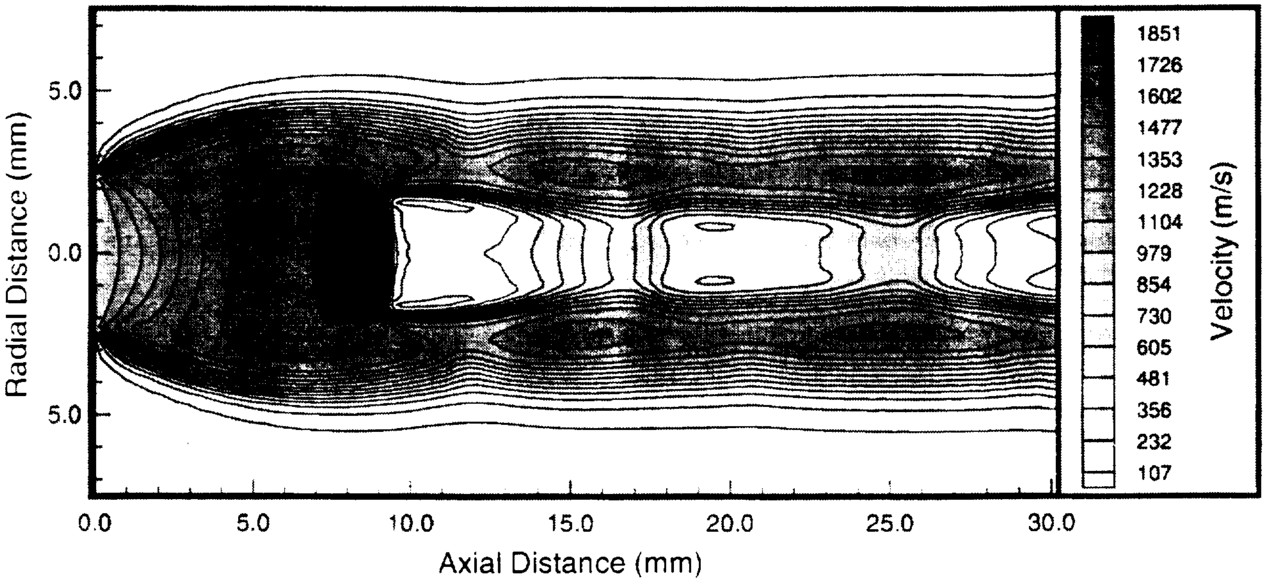

Figure 55. U-Velocity for High Pressure Case

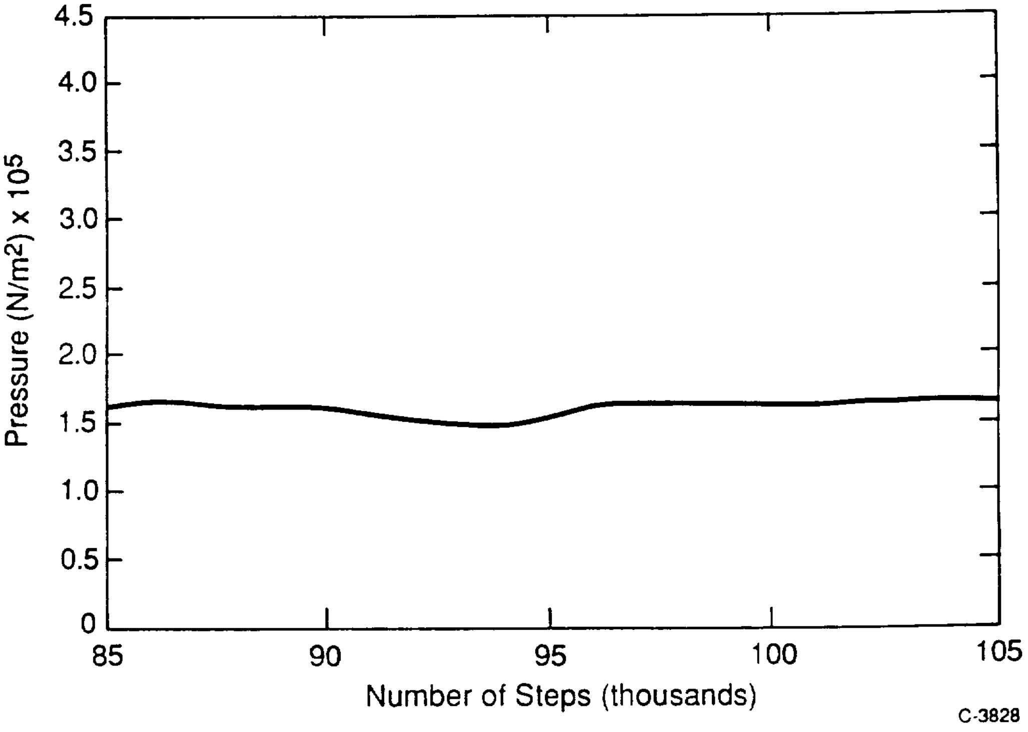

Figure 56. Initial SS Pressure p_1^{ss} at Outflow Boundary

disk also leads to relatively constant species mass fraction contours. Finally, the u-velocity field is shown in Figure 55. It has features that are very similar to the Mach number.

A series of computations were also run for the case of a higher inflow temperature (higher temperature case in Table 5). The results are shown in Figures 57 through 61. The centerline plot (Figure 57) is probably most valuable since it reveals the expected outcome that the post-Mach disk temperatures and velocities exceed those of the previous case. The Mach number (Figure 58) and pressure (Figure 59) contours reveal very minor changes compared with the high pressure case described above. Both the temperature (Figure 60) and the U-velocity (Figure 61) contours reveal the elevated conditions noted above. The contours are somewhat irregular near the centerline of the jet. This situation would relax with time if additional time steps were calculated.

The influence of the external co-flow was also explored and described in Figures 62 through 66. The results shown in Figures 51 through 55 are for a Mach 0.1 co-flow of 34.8 m/s. If the velocity of the co-flow is reduced by a factor of ten to 3.48 m/s, the flowfield changes with a small shift of the Mach disk location and some shift in the position of the cells downstream of the Mach disk. This is evidenced by comparing Figures 51 and 62. The contour plots of Mach number (Figure 63) and pressure (Figure 64) are very similar to the results shown previously for these parameters. The pressure diamonds have the same structure observed in the other simulations. The temperature (Figure 65) and the U-velocity (Figure 66) are also not very different from the earlier results. Even though it does appear that additional time steps are necessary to smooth out some of the contours near the axis of symmetry, the effect of the external co-flow appears to be minimal with no significant effect on the jet flow.

A final observation from the SPARK calculations was the lack of chemical activity in the jet near field. Figure 67 shows the calculated variation in the OH mass-fraction in the first six diameters of the jet flowfield. Along the centerline, and in most of the jet core flow, the OH mass-fraction is nearly constant,

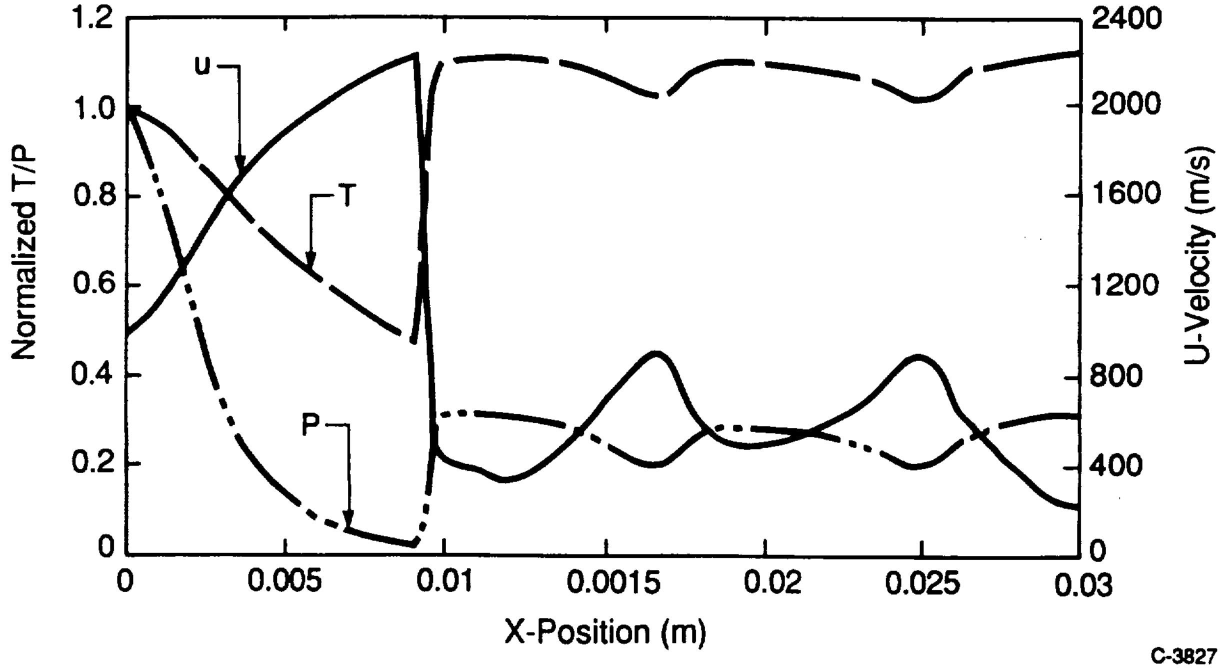

Figure 57. Centerline Flowfield Values for High Temperature Case

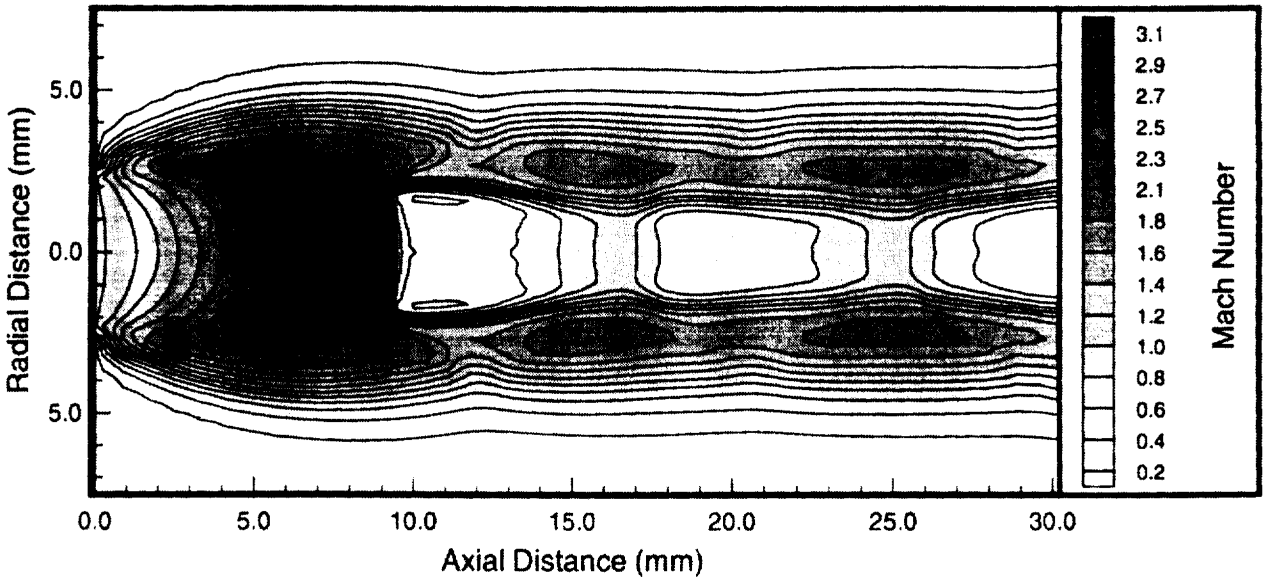

Figure 58. Mach Number Contours for High Temperature Case

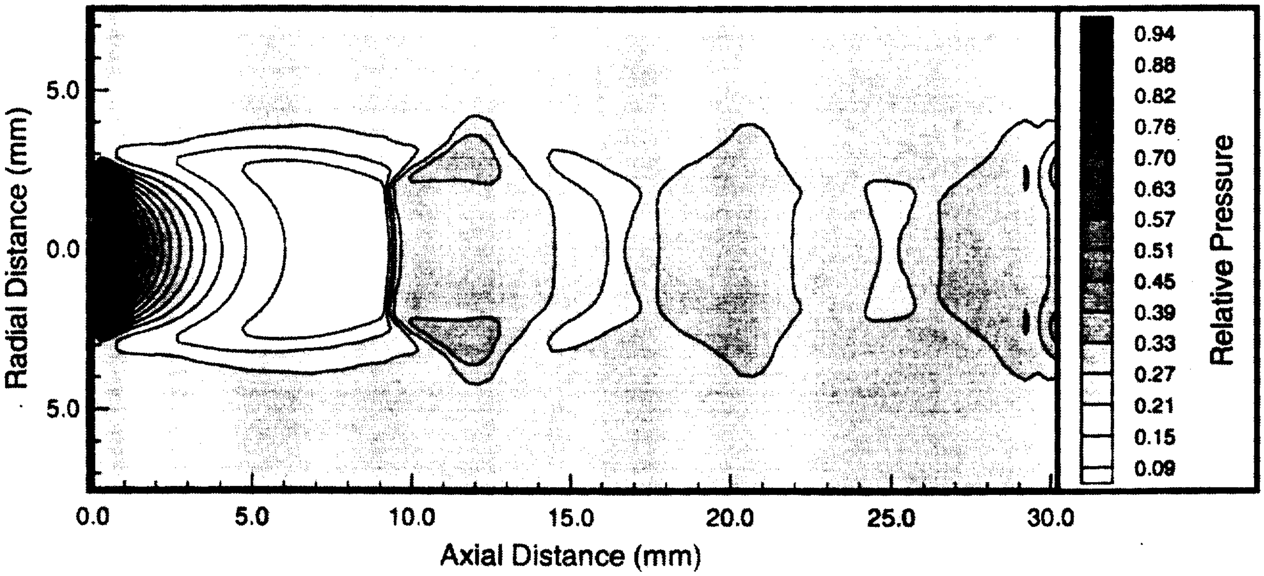

Figure 59. Pressure Contours for High Temperature Case

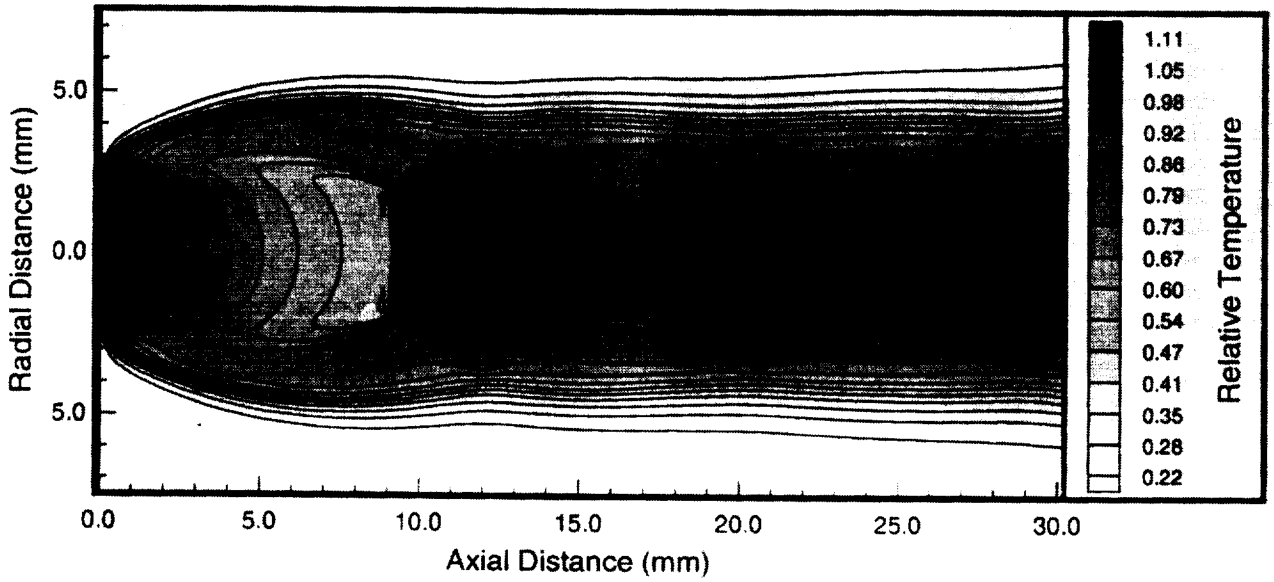

Figure 60. Temperature Contours for High Temperature Case

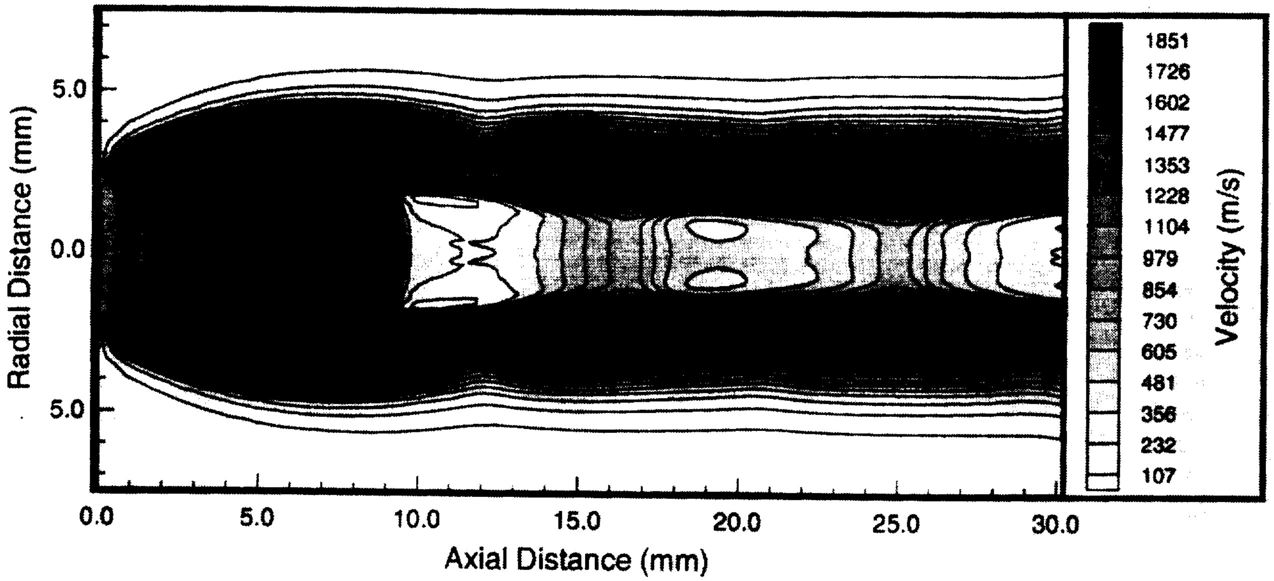

Figure 61. U-Velocity Contours for High Temperature Case

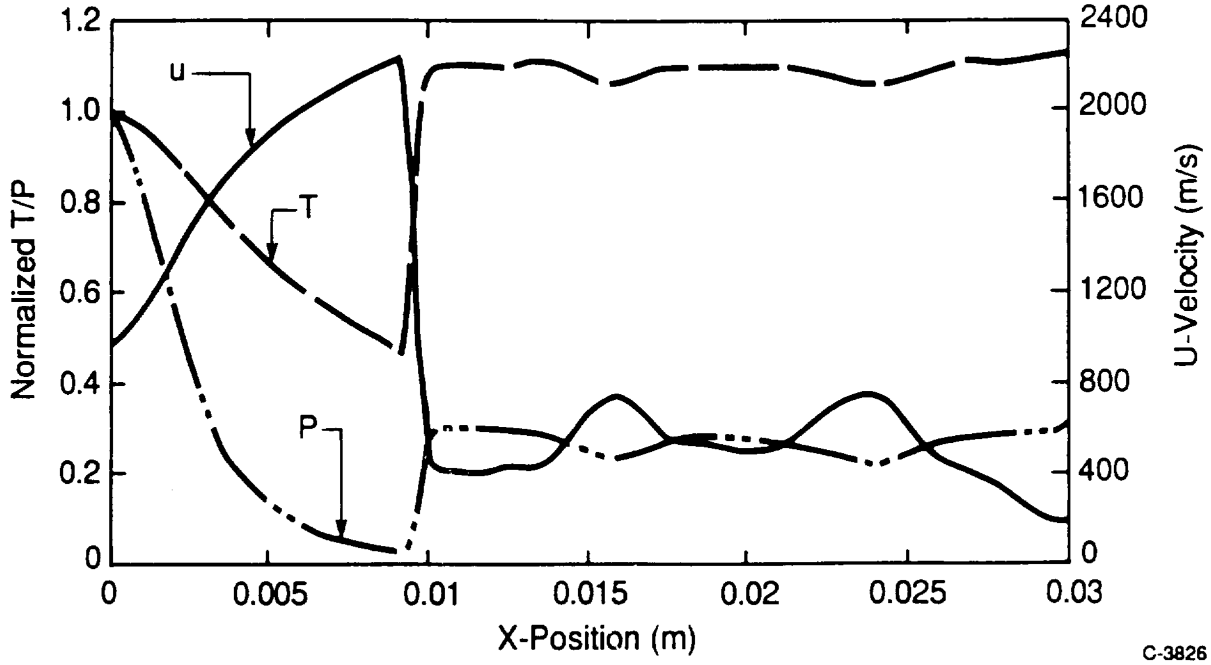

Figure 62. Centerline Flowfield Values for Reduced Co-Flow Velocity

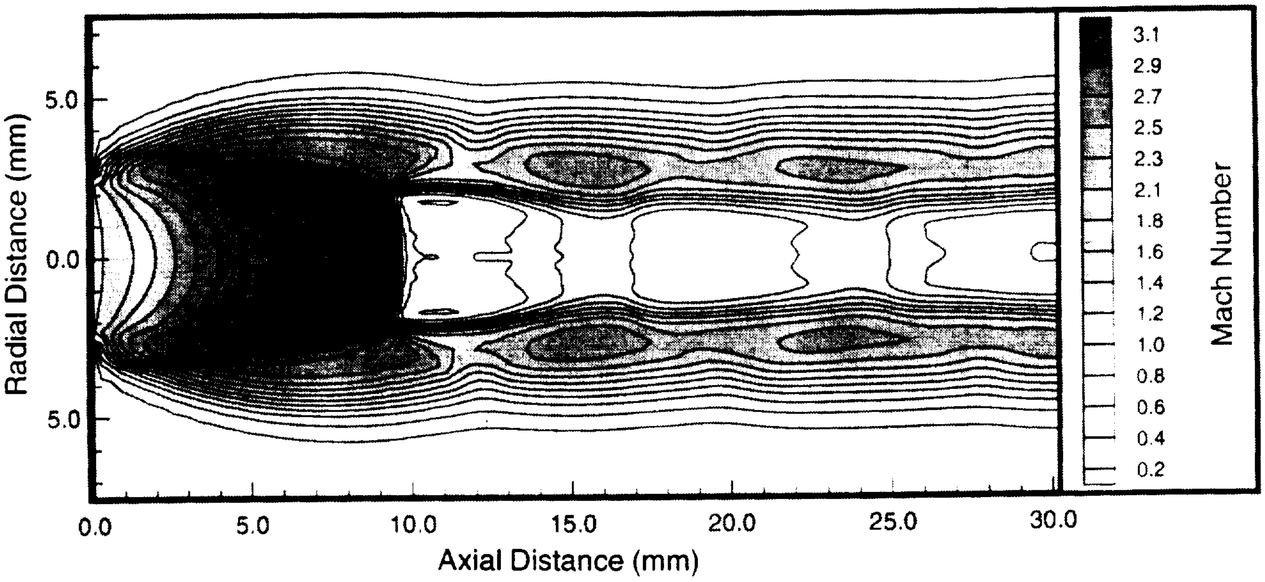

Figure 63. Mach Number Contours for Reduced Co-Flow Velocity Case

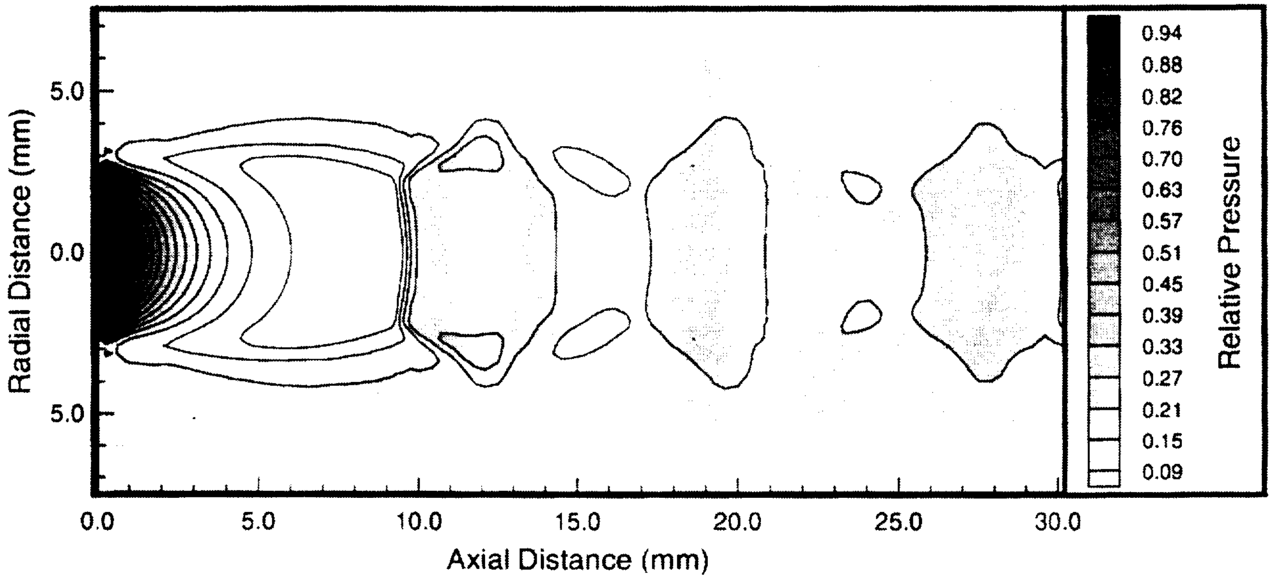

Figure 64. Pressure Contours for Reduced Co-Flow Velocity Case

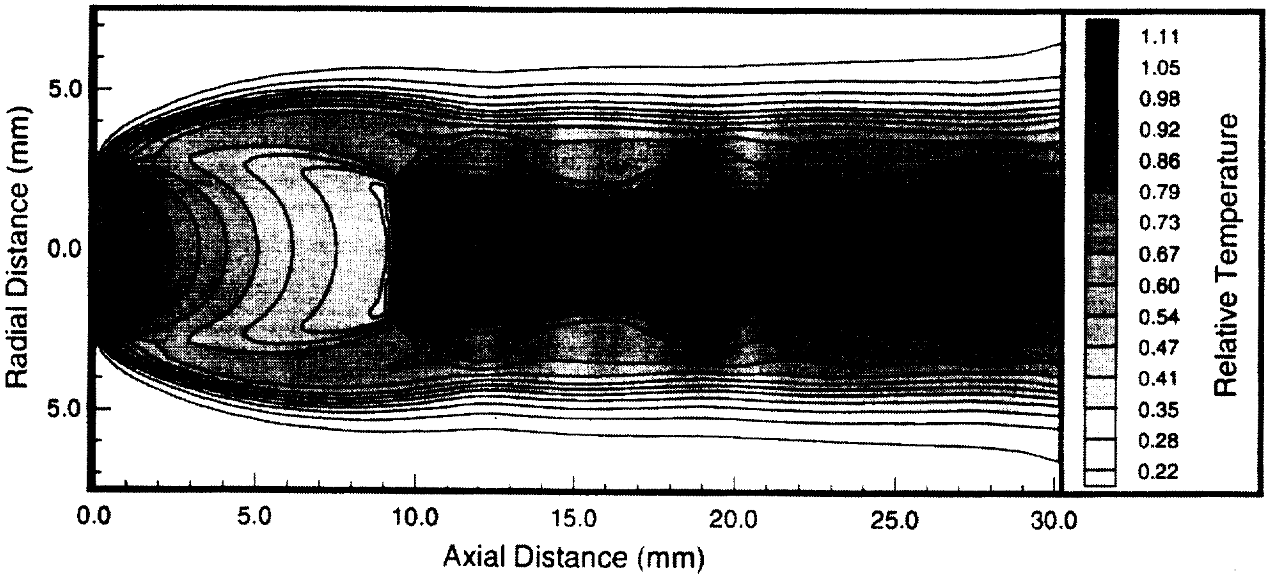

Figure 65. Temperature Contours for Reduced Co-Flow Velocity Case

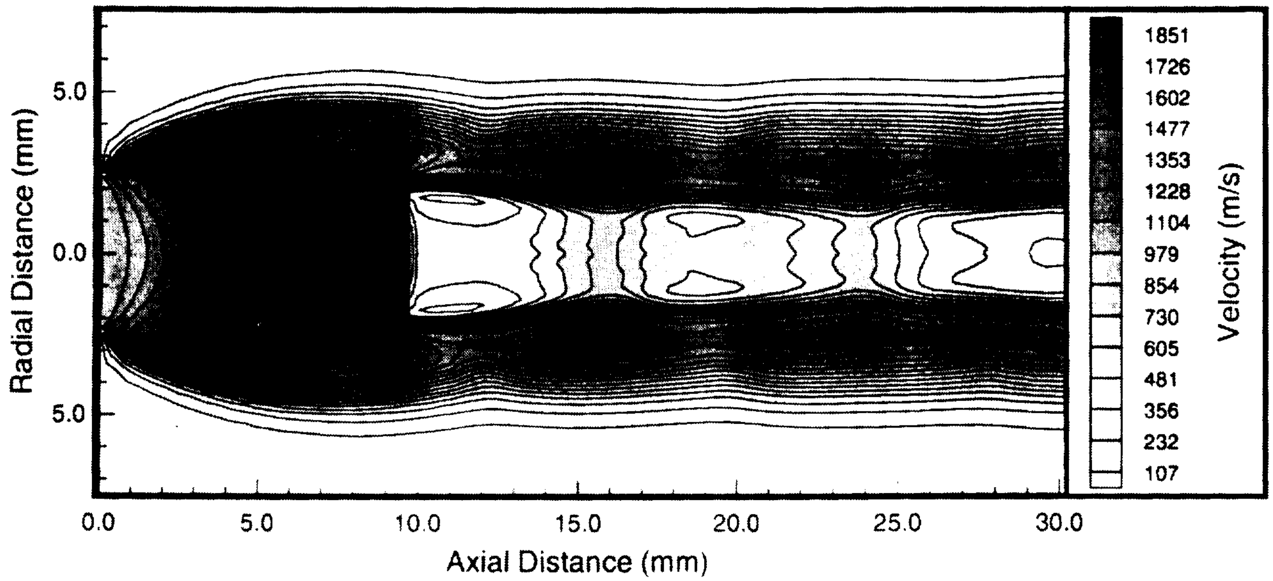

Figure 66. U-Velocity for Reduced Co-Flow Velocity Case

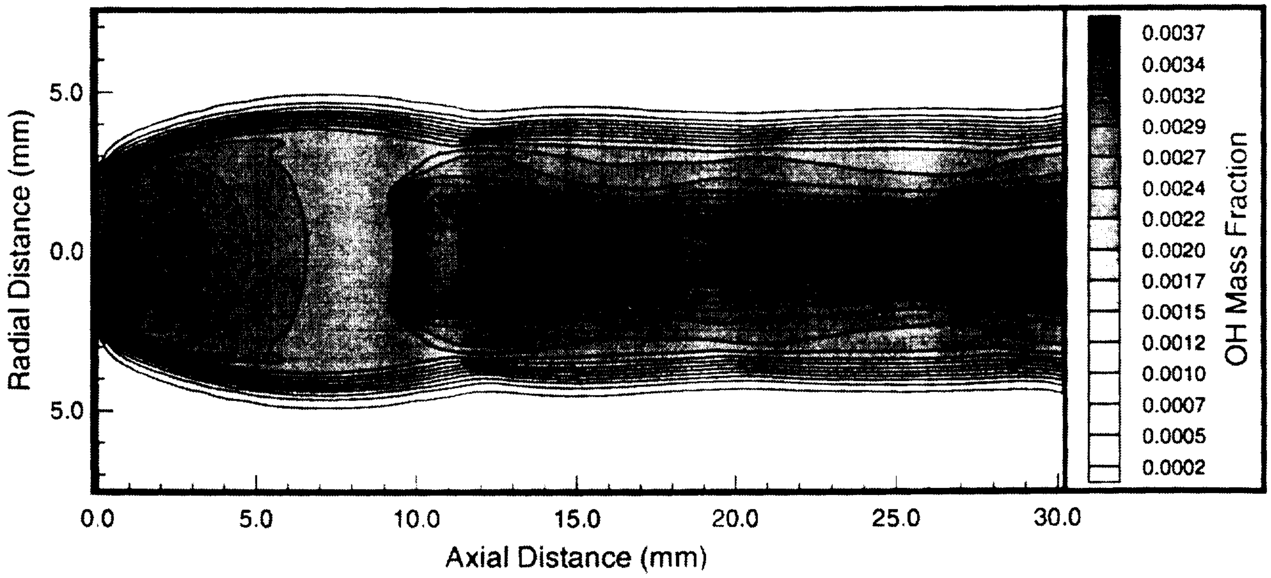

Figure 67. OH Mass-Fraction Contours in Jet Flowfield

with only about 30 percent decrease in the expansion ahead of the Mach disk. This indicates that the flow is nearly chemically frozen, with the drop in OH mass-fraction at the jet boundary due principally to mixing with the ambient air. This constancy of OH seeding ensures that the velocimeter will be able to sample most of the jet flowfield with nearly equal signal-to-noise levels. It further suggests that details of the chemical kinetics modelling may not be critical to the overall flow topology.

The SPARK modelling described in this section provides a means for quantitative comparison of the imaging velocimeter performance across the jet. It further permits the variations in background pressure and temperature to quantified, thereby enhancing our ability to project the results from the present program to new flowfield conditions.

5.4 Mean Velocity Profile Measurements

In order to verify the SPARK results and, secondarily, to confirm the operation of the burner, we conducted series of scanned velocity measurements along the burner centerline. The experimental setup for these measurements is shown in Figure 68. The output from the laser was split into two beams, one of which was directed across a methane-air flame Mekker-type burner. This channel sampled OH absorption transitions at essentially zero velocity. The second beam was focussed into the exhaust jet flow from the burner, with the burner tilted at 56 degrees from vertical. Once aligned, the beam delivery and fluorescence collection optics remained fixed on the optical table as the burner was traversed axially at 56 degrees using the rotation/translation stages described previously.

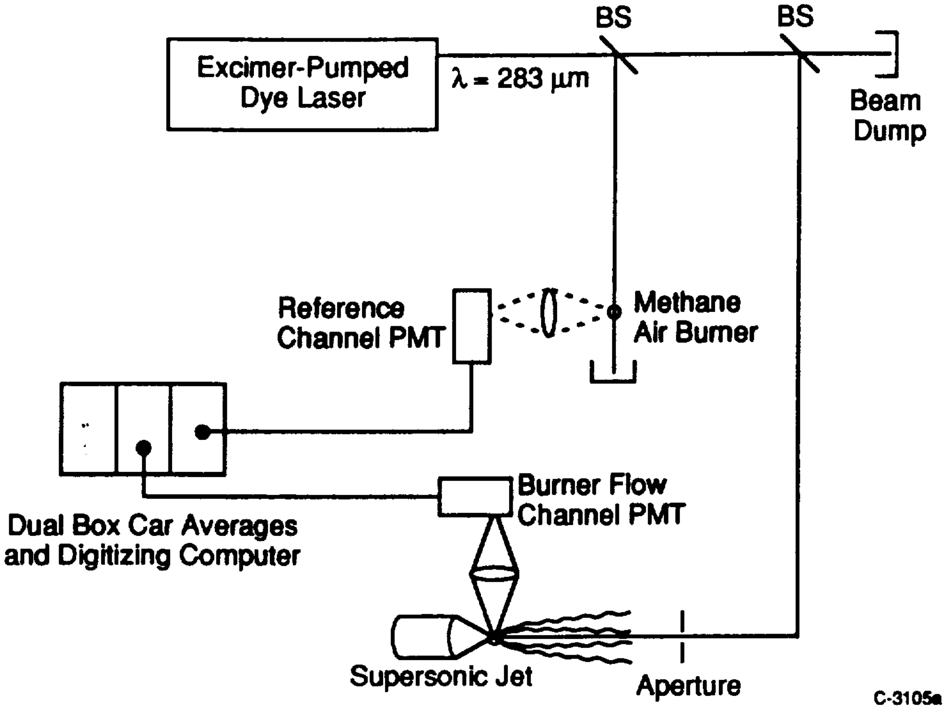

Figure 68. Experimental Setup for Mean Velocity Profile Measurements

Fluorescence was collected from both the flame and the jet flowfield using spectrally-filtered PMT's. In the jet flow channel, a series of beam apertures and field-stops were used to ensure that the PMT viewed fluorescence from a collection volume on the order of 250 μm wide. This small collection volume was necessary due to the small scales of velocity variation in the flowfield. As the laser was scanned across an absorption transition, the fluorescence was recorded simultaneously from both channels, providing both the reference (unshifted) frequency and the Doppler-shift frequency. Neither laser beam was focussed and the pulse energy was kept at about 100 μJ in order to avoid power-broadening of the transition, which would have reduced the sensitivity of the measurement.

Figure 69 is an example of the $P_1(4)$ lineshape recorded simultaneously in the flame (solid line) and jet flow (dashed line). The laser was scanned *down* in frequency so that the relative frequency scale is to lower frequencies. The jet flow lineshape was recorded at the nozzle throat and is much broader than the flame lineshape due to the higher temperature and pressure there. The measured shift between the two lineshapes is 0.088 cm^{-1} and the pressure-shift associated with the 2.8 atm pressure difference between the flame and the burner throat is - 0.022 cm^{-1}, for a net Doppler-shift of 0.066 cm^{-1}. This corresponds a directed velocity component of 556 m/s, or a measured axial velocity of 671 m/s.

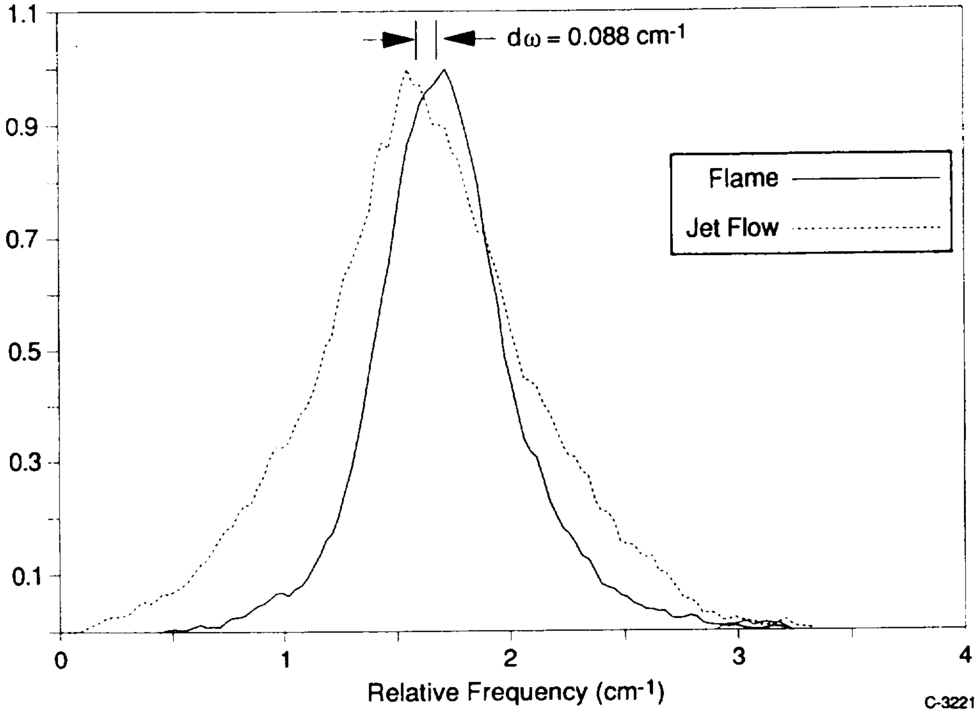

Figure 69. Doppler-Shifted OH Lineshape at Burner Throat. Doppler-shift, dω, is determined from half-power points.

Figure 70 is a similar plot where the jet flow lineshape was recorded 8 mm from the nozzle throat. The decrease in temperature and pressure at this position is evident in the narrower lineshape. The measured shift here is 0.182 cm^{-1} with a pressure shift of +0.009 cm^{-1}, for a net velocity-dependent shift of 0.191 cm^{-1}. This corresponds to an axial velocity of 1959 m/s. The series of measurements are summarized in Figure 71, where the mean velocity determinations are plotted against both the SPARK calculations and the experimental correlations. Except for the first data point at the jet throat, the measured velocity profile agrees well with the SPARK predictions. The low measured throat velocity was a persistent feature in several, repeated experiments, and may be due to non-idealities in the throat flowfield due to boundary layer effects. Downstream of the Mach disk, the velocity-shifts are small and the data generally agrees with the SPARK calculation within the accuracy of the determination of the shift.

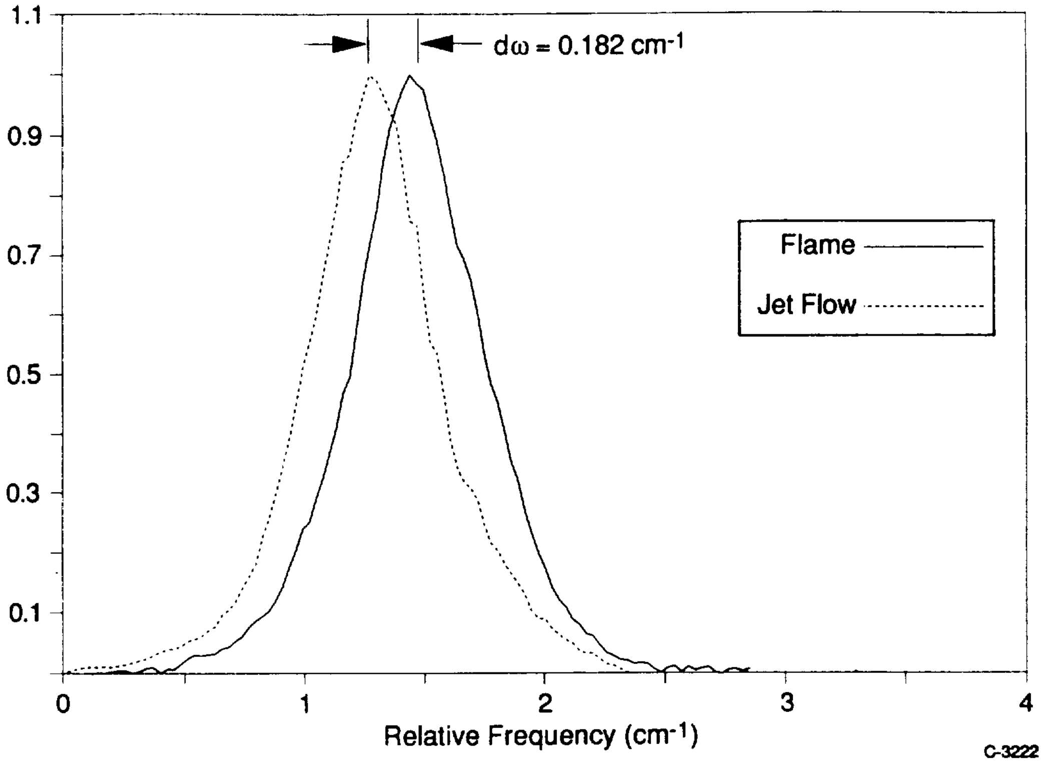

Figure 70. Doppler-Shifted OH Lineshape at 8 mm Downstream

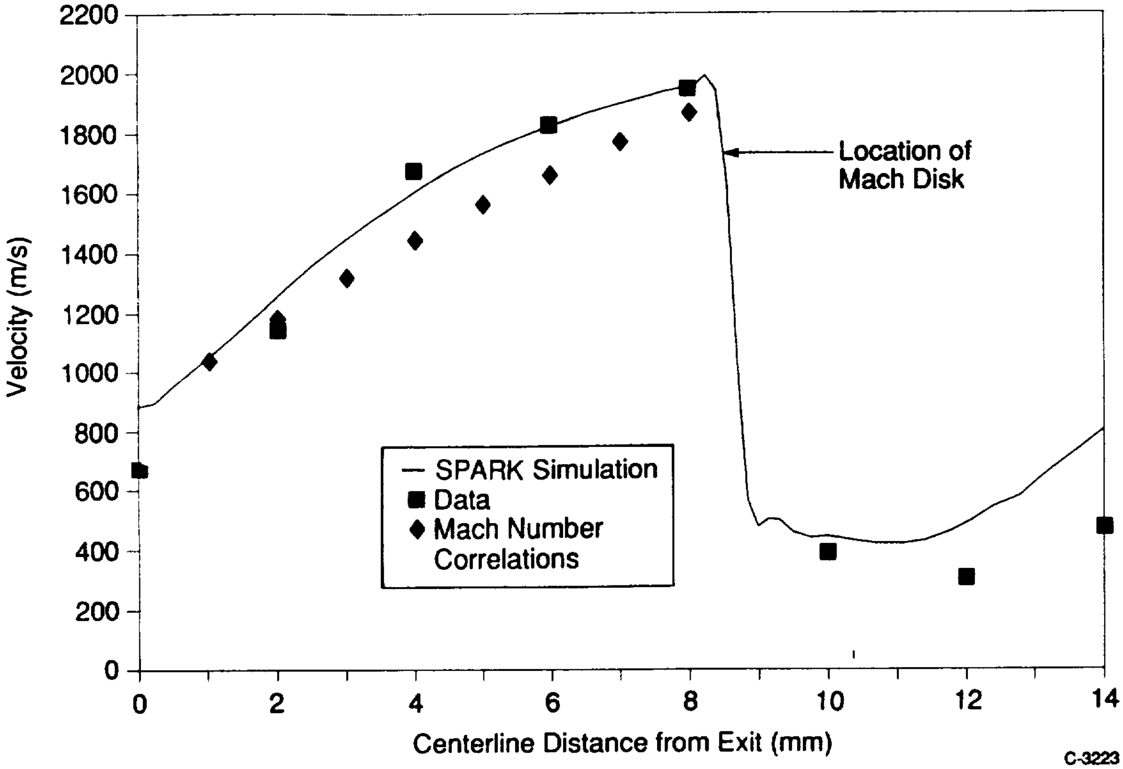

Figure 71. Comparison of Measured and Calculated Mean Velocity Profiles

The data shown in Figure 71 suggests that the SPARK calculations are an accurate determination of the jet flow properties. Another check on the validity of the SPARK calculations consisted of OH PLIF imaging to define the spatial position of the prominent shock features. Two such images, obtained using a Nd:YAG-pumped dye laser are shown in Figure 72. In both images, the flow is from left to right and the nozzle exit plane is approximately coincident with the left side of the image. The PLIF data are grouped into ten equal-increment gray levels. Neither image has been corrected for axial variations in the laser sheet intensity.

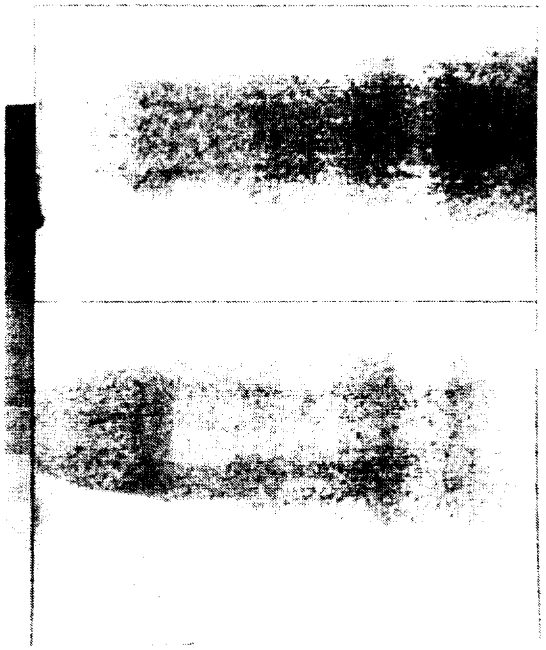

V-669

Figure 72. Example OH PLIF Images in the Jet Flowfield

The images reflect the difference in the temperature sensitivity of the two excitation strategies employed. For OH in this flow, the quenching is dominated by H_2O, which can be modelled as

$$Q = N_{H_2O}\,\sigma T^{-n}\,v$$

where σ is the cross-section for quenching and v is the mean molecular velocity. The temperature dependence of the cross-section is $0.5 < n < 0.75$.[48,49] Using the ideal gas law to replace N_{H2O} and using the SPARK result that the flow is essentially chemically frozen, the quenching term has the following thermodynamic dependence:

$$Q \sim PT^{-1}$$

where we have take $n \simeq 0.5$. The OH fluorescence signal then may be expressed as

$$S_F \sim f_B(T) \cdot \chi_{OH} \qquad (61)$$

where $f_B(T)$ is the temperature-dependent Boltzmann population fraction in the laser-excited level, χ_{OH} is the (constant) OH mole-fraction, and we have canceled the common pressure and temperature terms in the numerator and denominator. Equation 61 shows that the fluorescence image will reflect primarily the temperature dependence of the Boltzmann population fraction of the laser-excited level.

The top image was obtained from excitation of the $Q_1(5)$ transition, which exhibits a weak temperature dependence over the range of temperature variations in this part of the flow. As such, there is no indication of the Mach disk in the image. The increase in signal with downstream distance (darker levels in the image) is associated with uncorrected laser sheet energy variations rather than actual flow phenomena. The OH mole-fraction across the jet is apparently uniform, and there is no evidence of the axial "streamers" observed in the Phase I program.

The bottom image was obtained from excitation of the $Q_1(2)$ transition, which exhibits a negative temperature dependence over this range. As such, the Mach disk is clearly visible as a sudden decrease in signal level associated with the sudden increase in temperature. The Mach disk is located about 7.5 mm downstream of the nozzle throat, in good agreement with the SPARK prediction of 8 mm. Also, the overall position of the reflected shock waves near the triple-point and the jet width are in good agreement with the calculations shown in Figures 58 through 61 of Subsection 5.3.

The signal levels of this image, however, were substantially lower than expected. From the measured laser energy, collection efficiency, and expected temperature/pressure conditions, we estimated that the OH mole-fraction was only about 20 ppm in this image. We subsequently modified the burner (described in Section 4) to incorporate a zirconia/alumina insert. The insert reduced the heat transfer efficiency to the burner walls, resulting in a higher exit gas temperature and concomitant increase in the OH mole-fraction. The scanned velocity results shown in Figure 71 above were obtained after the addition of the ceramic liner. They correspond to an exit gas temperature of about 1850 K, only 200 K below the adiabatic temperature.

In order to further increase the PLIF signal levels for the velocimetry imaging experiments, we adjusted the burner conditions to operate with less N_2 (90 percent of the air value at the measure O_2 flow rate) and an overall equivalence ratio of 0.89. These conditions resulted in a further increase in the gas temperature and OH concentration. This is also the "high temperature" condition referred to in the section describing the SPARK calculations.

6. IMAGING INSTRUMENT CHARACTERIZATION EXPERIMENTS

This section describes the final experimental synthesis of the various tasks detailed in the previous sections. It begins with a discussion of the experimental setup used for the velocity imaging demonstrations along with a summary of the modifications required to our original configuration. The raw PLIF data and the data reduction procedures tailored to the specific experimental conditions are reported next. Finally, the velocity imaging results are presented and compared with the SPARK predictions.

6.1 Experimental Setup and Signal Level Considerations

The velocity imaging demonstrations were conducted in a series of experiments over the course of several weeks. During this time, numerous modifications and improvements to the basic setup were implemented, as necessitated by problems encountered with earlier attempts. The final version of the setup is shown in Figure 73. An inevitable feature of any PLIF imaging experiment is the necessity to obtain the highest possible laser pulse energy. This was particularly important for the present application where the accuracy of the velocimeter depended on the signal-to-noise ratio of two individual PLIF images. In order to maximize the available pulse energy, the harmonic separator elements from the dye laser were removed and replaced with a single Pellin-Broca prism outside of the laser cavity. This minimized reflection losses in the standard separator.

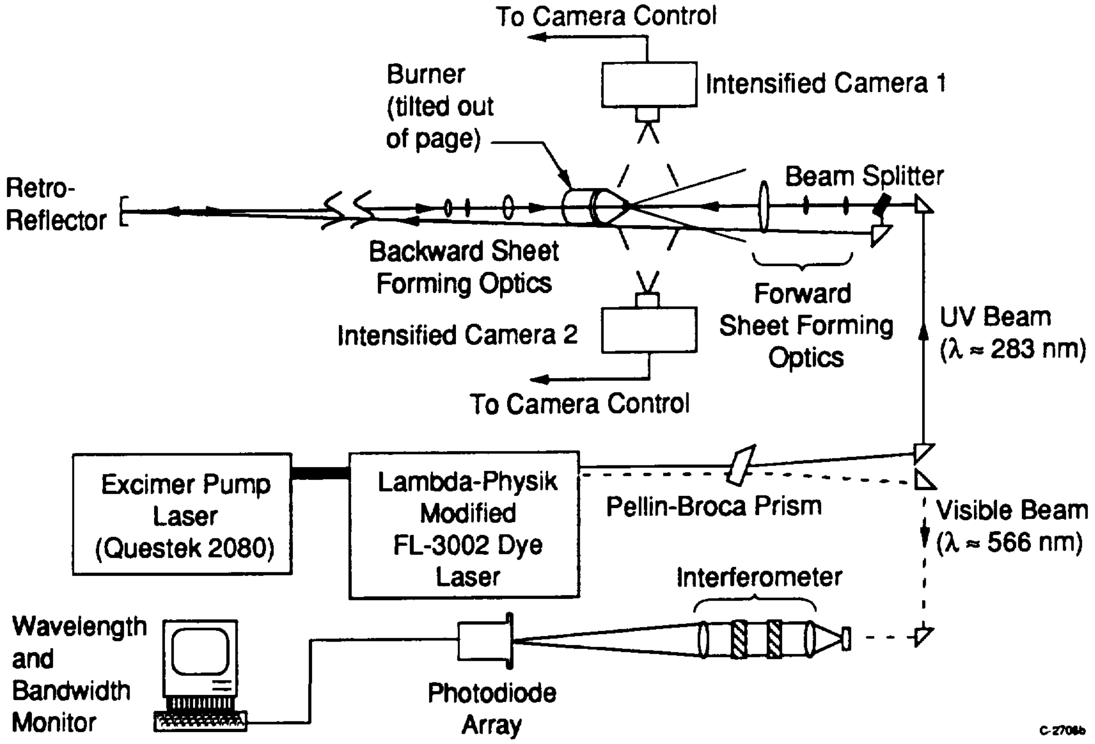
To Camera Control
Burner (tilted out of page)
Intensified Camera 1
Retro-Reflector
Beam Splitter
Backward Sheet Forming Optics
Forward Sheet Forming Optics
Intensified Camera 2
UV Beam (λ ≈ 283 nm)
To Camera Control
Excimer Pump Laser (Questek 2080)
Lambda-Physik Modified FL-3002 Dye Laser
Pellin-Broca Prism
Visible Beam (λ ≈ 566 nm)
Interferometer
Wavelength and Bandwidth Monitor
Photodiode Array
C-2708b

Figure 73. Experimental Configuration for Velocity Imaging Demonstrations

Using this approach, the UV and residual visible output from the laser could be directed along separate paths with a minimum loss in the UV. We were able to achieve approximately 3 mJ total UV pulse energy in the final experiments. The visible beam, typically at about 566 nm, was directed into the interferometer setup described in detail in Section 3. The UV beam was directed toward the burner, where an AR-coated beam splitter was used to create two beam paths. The primary, forward propagating beam, was then formed into a thin sheet approximately 2 cm in height and 250 μm thick. This sheet was directed along the top of the burner which was again tilted at 56 degrees from the vertical with the exhaust gases flowing in a direction counter to the forward beam.

Initially, we had hoped to pass this beam through the flowfield and retro-reflect it after a total propagation path of about 50 feet. This pathlength ensured that the two laser pulsed would be separated by ~50 ns and could thus be discriminated by the fast-gating camera ($\tau_{g,min}$ = 20 ns). This approach would not have required a beam splitter and the entire pulse energy would be available for each sheet. We quickly determined, however, that the strong refractive index gradients in the flowfield severely disrupted the beam over these long path lengths and we were forced to use the beam splitter and a separate optical path. The second beam passed near the burner and travelled about 25 ft across the lab to a coated mirror, where it was retro-reflected back through a series of sheet forming optics. This backward propagating beam was then focussed to the same plane in the jet flowfield as the forward propagating sheet. We typically delivered about 1.5 mJ in the forward sheet and about 0.75 mJ in the backward sheet.

Two identical Phillips CCD cameras were used to image the fluorescence. One camera was fitted with a slow gating intensifier ($\tau_{g,min}$ ~ 1 μs) and the second with a fast gating intensifier. The fast gating tube used an additional layer of metalization on the photocathode which reduced the overall sensitivity of this camera by about an order of magnitude compared to the slow gating camera. The two cameras were carefully aligned with an Air Force registration target prior to the experiments. In order to further increase the signal-to-noise ratio, only 2 mm UG-5 blocking filters were used. These transmit over 90 percent of the fluorescence, but do little to reject scattered laser light or burner incandescence integrated by the slow-gating camera. For these reasons, we were unable to image the velocity closer than about 2 mm from the nozzle exit.

Example raw PLIF images obtained by excitation of the isolated $P_1(4)$ transition at 283.463 nm are shown in Figure 74. The left image is from the slow gating camera which integrated both the forward and backward propagating laser sheets. The right image is from the fast gating camera and is from the forward propagating sheet only. The field of view in both images is 2.56 cm (H) by 1.92 cm (V) and the jet flow is from lower right to upper left. The signal level in each image has been rescaled for this figure so the gray scales do not represent the actual relative signal strengths between the two images. In actuality, the fast gating camera image is about a factor of 20 weaker than the slow gating camera image. In order to improve the signal to noise ratio, we typically averaged several frames during the course of an experimental sequence. The slow gating image at the left is the average of 24 laser pulses and the fast gating image at the right is the average of 12 laser shots. All of the data presented in this section are similarly averaged.

The velocity sensitivity of the fluorescence signal is immediately apparent from the difference in the flow structure revealed by each image. For these images, the laser was detuned from the static absorption line-center by $+0.26$ cm^{-1}, as determined by the shift in the interferogram recorded from the Fabry-Perot. At this detuning, the fluorescence signal in the static flame is down by about 1/2 from the line-center value. The slow gating camera, integrating both forward and backward propagating sheets, averages both up- and down-shifted fluorescence signals, resulting in a fluorescence signal which is independent of velocity but which retains some pressure and temperature sensitivity from the absorption lineshape near the half-width of the convolution profile. Most of the signal variations in the jet are due to variations in the laser sheet energy profile. The Mach disk is barely visible near the bottom of the image. The fast gating camera, in contrast, views only the forward propagating sheet. Since we have already detuned the laser to higher frequencies, regions of high velocity in the flow are further shifted out on the convolution lineshape, resulting in lower fluorescence signals. Thus, the right image in Figure 74 has the highest fluorescence signals in the low velocity regions immediately downstream of the Mach disk.

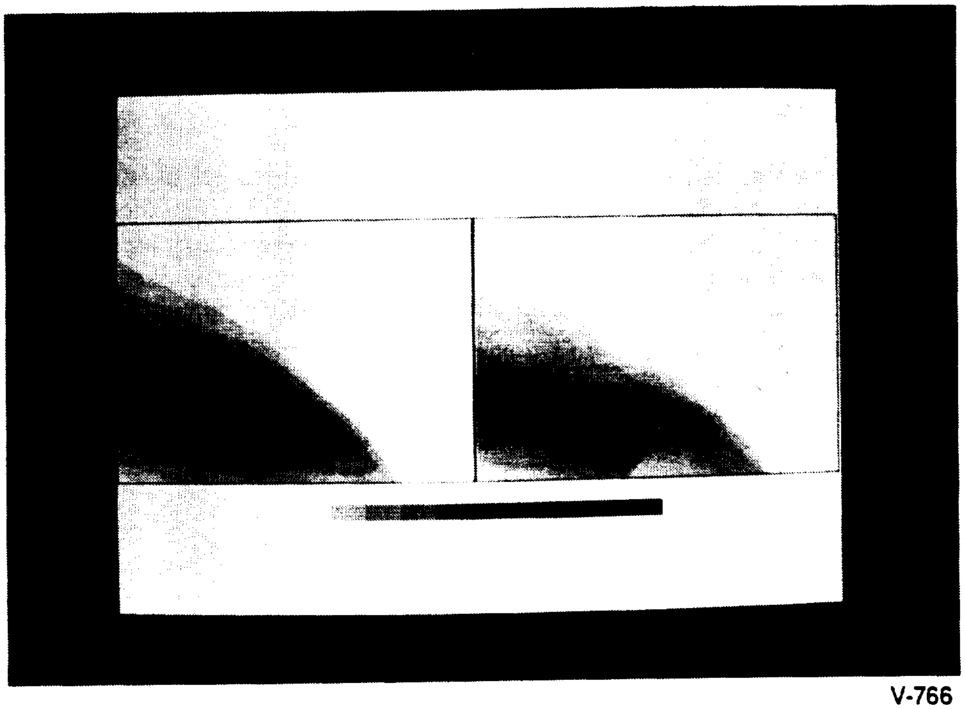
V-766

Figure 74. Comparison of Raw PLIF Images From Slow Gating Camera (left) and Fast Gating Camera (right)

Based on the SPARK prediction of 0.5 percent OH (mole-fraction) at typical post-Mach disk conditions of ~ 1 atm and 2400 K, the available laser energy generated a signal level of approximately 1500 photons/pixel. For the 10 percent quantum efficiency of the slow gating camera, this corresponds to a signal-to-noise ratio (SNR) of about 12. For the fast gating camera, the lower quantum efficiency and the fact that only one sheet of 0.75 mJ was used resulted in a single pulse SNR of only about 4. By image averaging, we were able to improve this to about 10. Since the SNR of the velocity image will depend approximately on the rms sum of the individual image SNR's, the image averaging was an important improvement in the resulting accuracy of the velocimeter. True single-pulse imaging would be possible with either an improved quantum efficiency in the fast gating detector or with higher laser pulse energy. Both such improvements are now available.

The high OH mole-fractions also introduced a possible complication from laser beam absorption. The integrated absorption strength for these conditions is about 0.1 cm^{-1}. Thus, at line-center the laser pulse energy is attenuated by about 10 percent in every centimeter. As we detune from the static line-center, relatively less of the laser bandshape experiences the strong line-center absorption. Nevertheless, distortions of the convolution lineshape can be expected to give rise to small velocity errors at the edges of the jet corresponding to the longest pathlengths through the absorbing gas for either the forward or backward propagating sheets. Depending on the magnitude and direction of the static detuning, this laser attenuation effect was observed to severely distort the images, rendering impossible any meaningful velocity determination. In practice, we were required to detune by at least ~ 0.2 cm^{-1} to the blue, so that the forward propagating sheet was further shifted by the directed jet velocity to lower frequencies. As Figure 74 shows, the backward propagating sheet traversed a significantly shorter region of absorbing gas in the field of view.

Therefore, even though it was Doppler-shifted back toward the line-center, we did not observe significant laser absorption effects in the resultant velocity images.

6.2 Data Reduction and Velocity Calculations

The flow velocity was calculated from the ratio of the PLIF images using Eq. 18, developed in the first section of this report. As discussed extensively in the previous sections, the form of the algorithm depends on both the laser bandshape and absorption lineshape. These effects are illustrated in Figure 75, where we plot the variation in the OH lineshape over the range of centerline thermodynamic conditions in the jet. Also shown for reference is a laser bandshape which is statically detuned to + 0.26 cm^{-1} and has a FWHM = 0.44 cm^{-1}. The absorption lineshapes were calculated using our measured broadening parameters and assuming equilibrium major species concentrations. The laser bandshape was measured prior to the velocity imaging experiments. This magnitude of detuning is nearly optimal in minimizing the sensitivity of the velocimeter to the uncharacterized thermodynamic variations.

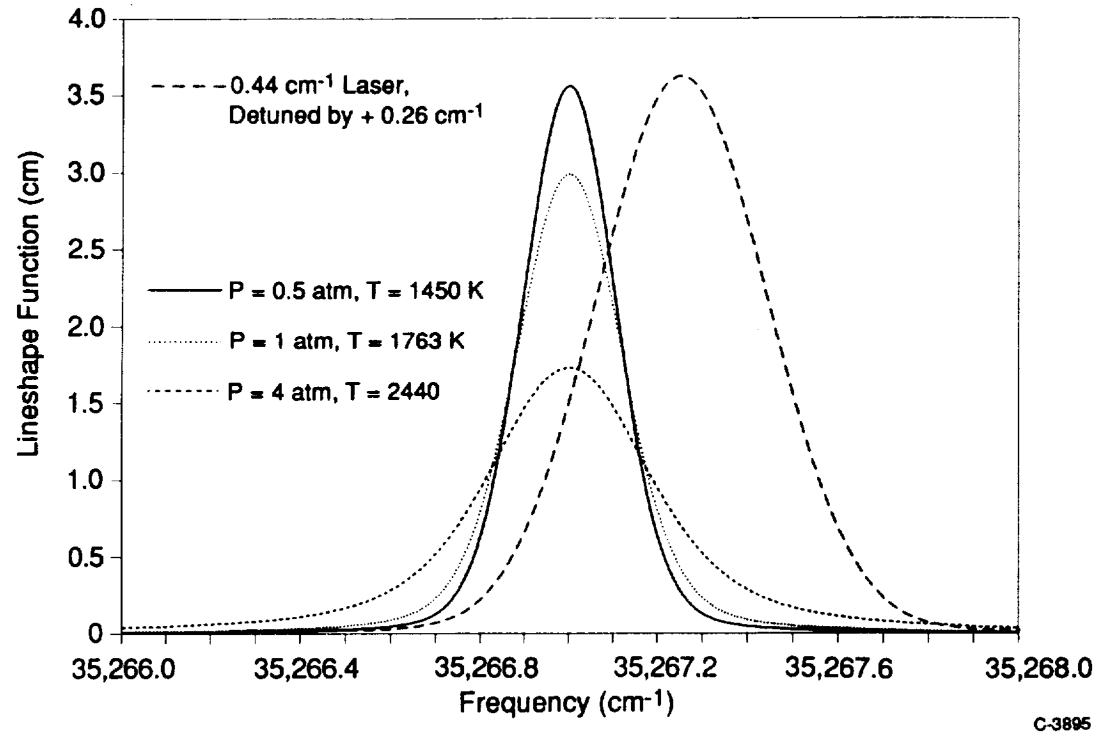

Figure 75. Comparison of OH Absorption Lineshapes at Selected Conditions in the Jet Flowfield with the UV Laser Bandshape

This is illustrated in Figure 76, where we plot the velocity algorithm, $\psi_{(v)}$, for three typical conditions of the jet near field. Except for the throat condition, the curves lie close together, indicating a small uncertainty due to the thermodynamic variations in the measured velocity. Note that the curves do not collapse to zero at zero velocity. This is due to the unequal laser energies in the forward and backward propagating sheets. At zero velocity, the velocity algorithm is equal to twice the forward image divided by the sum of the forward and backward images minus 1. Since the backward propagating laser sheet is half as intense as the forward propagating sheet, on average, this calculation yields $\psi_{(0)} = 0.3333$, instead of zero. The effect of the unequal laser sheet intensities is to reduce the velocity dynamic range of the measurement.

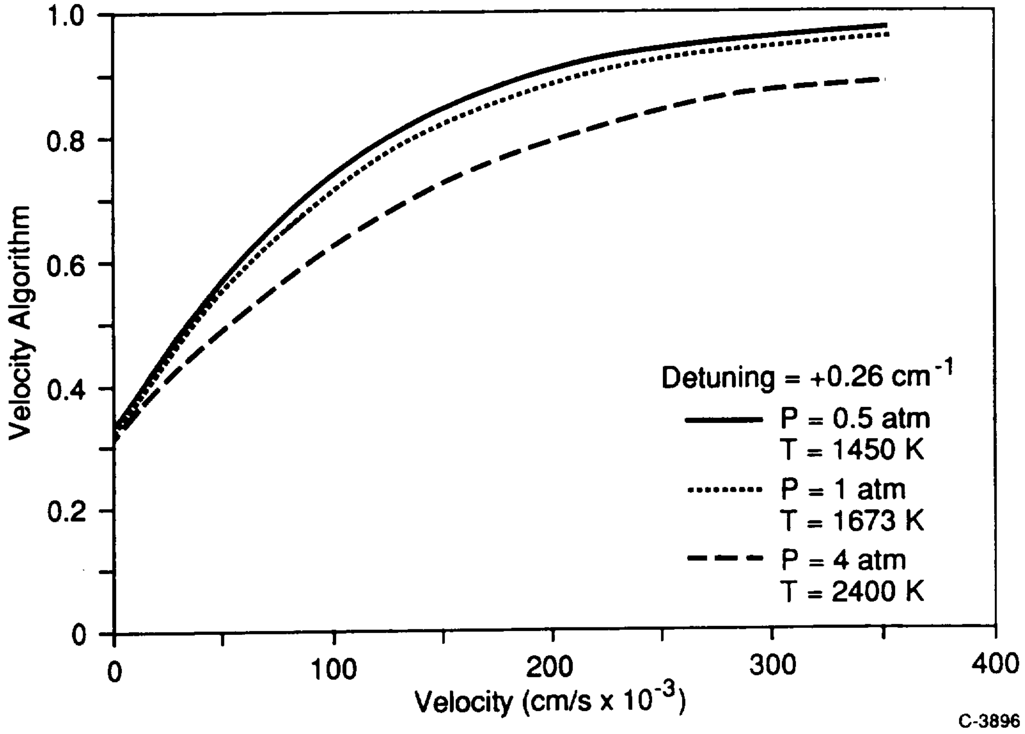

Figure 76. Comparison of the Velocity Algorithm for Thermodynamic Variations Shown in Figure 75

This dependence of the velocity algorithm on the relative sheet intensity was a significant experimental concern and ultimately proved to be the limiting source of error in the present demonstrations. Figure 77 shows the effect of variations in the relative laser sheet intensity on the functional form of the velocity algorithm. In this case, the calculation was for $P = 1$ atm, $T = 1673$ K, and a static detuning of $+0.18$ cm^{-1}. The three curves shown span a range of I_B/I_F from 0.25 to 0.5. Comparison of Figure 77 with Figure 76 shows that small variations in the relative laser sheet intensity distributions have a much greater impact on the accuracy of the measured velocity than do the thermodynamic variations within the jet itself. We found the experimental constraint to generate and maintain equal uniformity of the varying forward and backward laser sheets to be the principle experimental challenge.

An initial experimental configuration where the relative sheet intensity overlap is guaranteed was conducted first. The burner was directed vertically, so that only the radial velocity components of the jet could Doppler-shift the absorption lineshapes. In this setup, only the slow gating camera was used along with a single, forward propagating sheet. The beam splitter was removed and the full laser pulse energy was directed into the forward sheet. This image was then simply mirrored about the axis of symmetry of the flowfield to synthesize the backward propagating sheet image. The images were then processed according to Eq. 18 and scaled so that the zero velocity contour at the jet centerline was at the center of the A/D dynamic range of the image, as shown in the lower figure.

Figure 78 shows the form of the velocity algorithm for these experimental conditions. For clarity, we have only shown the case corresponding to the principal jet flow conditions of nearly 1 atm and 2400 K. The solid line is the algorithm which is anti-symmetric about zero. The dashed curve is a linear function with the same slope at $v = 0$, showing that for this limited velocity range, the algorithm is essentially linearly proportional to the flow velocity. In other words, $\psi_{(v)} = Cv$, where C is an experimental constant. No non-linear mapping of the result from processing the two images according to Eq. 18 is necessary. Since a single

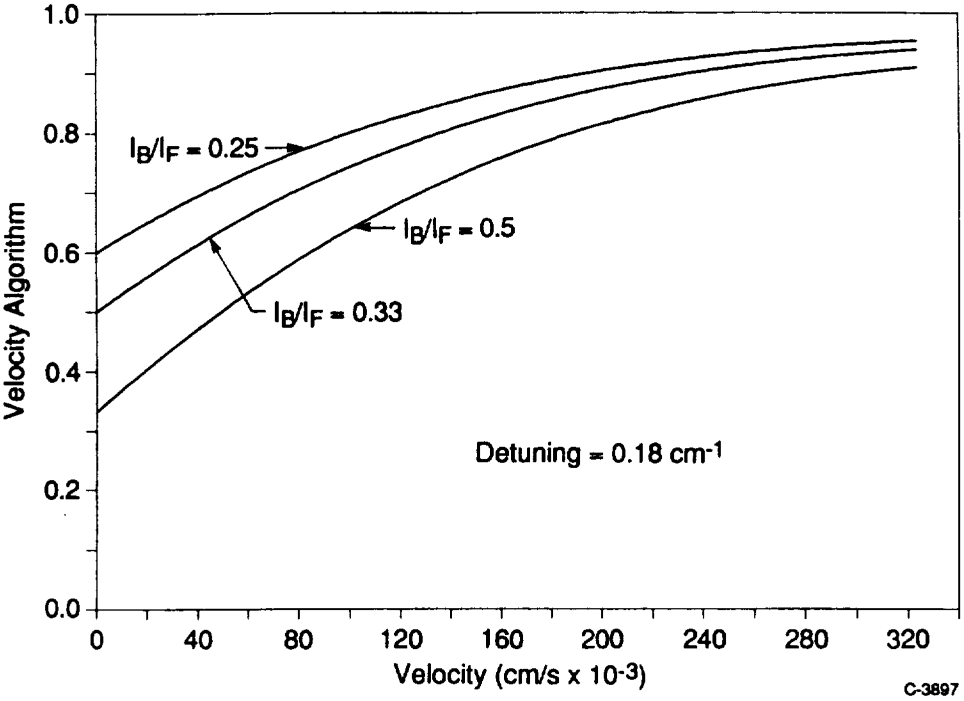

Figure 77. Comparison of the Velocity Algorithm for Various Values of the Relative Sheet Intensity

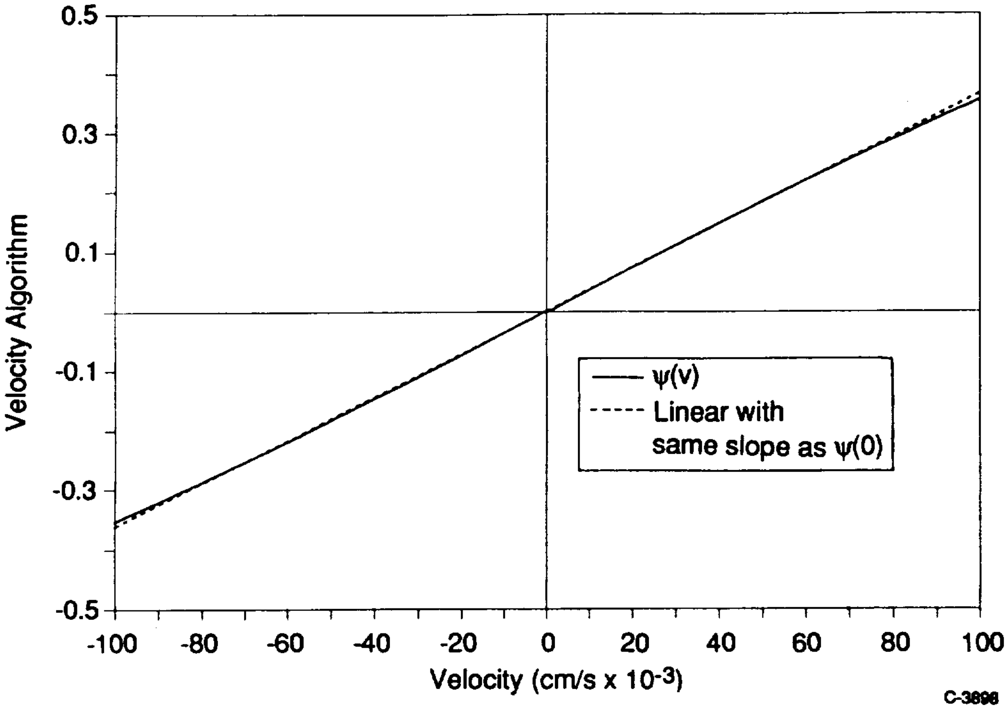

Figure 78. Velocity Algorithm Corresponding to the Radial Velocity Determination

laser sheet was used to generate the two images, the laser sheet intensity variation is by definition constant and we have introduced no velocity uncertainty due to this effect.

Figure 79 is a comparison of the calculated radial velocity distribution (here plotted as the antisymmetric component aligned with direction of the laser sheet propagation) to the measured velocity distribution. The measured velocity frame has been scaled to match the velocity range in the calculated frame. Since the algorithm of Eq. 18 is essentially a linear map of the velocity, the scaling is simply placing the relative velocity map on an absolute basis against the code predictions. The agreement between the calculated and measured velocity distributions is excellent through all regions of the near jet flowfield. From the nozzle exit at the bottom of the image, through the Mach disk, and extending to the end of the second shock cell, all of the major flow patterns are correctly visualized, despite the order of magnitude variation pressure and the factor of 2 variation in temperature. Note that regions of the flow with velocity variations less than 100 m/s are clearly resolved. Some differences in the width of the Mach disk and the exact shape of the waves downstream of the Mach disk are observable. This region of the flowfield is dominated by viscous mixing effects which are not well modelled by the SPARK code turbulence model. It is unreasonable to assign high confidence to the calculated details of all the subtle wave interactions here and we believe the measured velocity distributions are more accurate than the code predictions. Nevertheless, the overall agreement is excellent. This result clearly demonstrates the essential feasibility of the velocity imaging technique in high pressure, high temperature supersonic combusting flowfields with large, uncharacterized temperature and pressure variations.

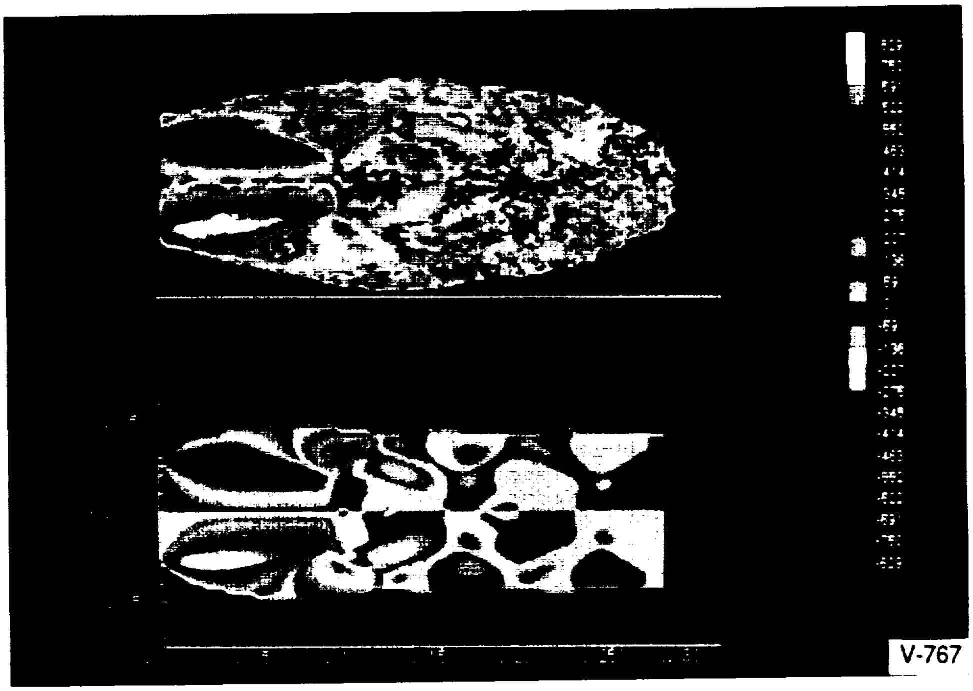

Figure 79. Comparison of Measured (Upper) and Calculated (Lower) Radial Velocity Distributions

The radial velocity imaging demonstration, however, does not demonstrate the capability of the technique for measurements in flows without axes of symmetry or for single pulse images. This type of measurement places much more stringent demands on the maintenance of constant, known relative laser sheet intensities. Great care was taken to align the laser sheets so that the inevitable variations in each laser sheet's

PAGE [illegible] INTENTIONALLY BLANK

intensity were overlapped. This was done prior to the actual velocity measurements by inserting a small propane torch in the measurement plane and sequentially recording the forward and backward sheet intensities in the quasi-uniform OH field. Figure 80 shows a typical example of the intensity variation of two well-aligned sheets prior to the beginning of a velocity measurement. Both sheets exhibit more than a factor of two variation in the local intensity, although the large scale pattern of the variations are similar. The solid line is a plot of the ratio I_B/I_F and shows that the ratio is reasonably uniform over the lower half of the image. (The camera pixel numbers are the row numbers beginning at the top of the image.) Some differences exist, principally due to the evolution of the far-field diffraction patterns in the original laser beam as the backward propagating sheet travels over its ~ 15 m delay path. The relative stability of the ratio in the lower half of the frame, however, corresponds to the active portion of the frame where the jet signal occurred.

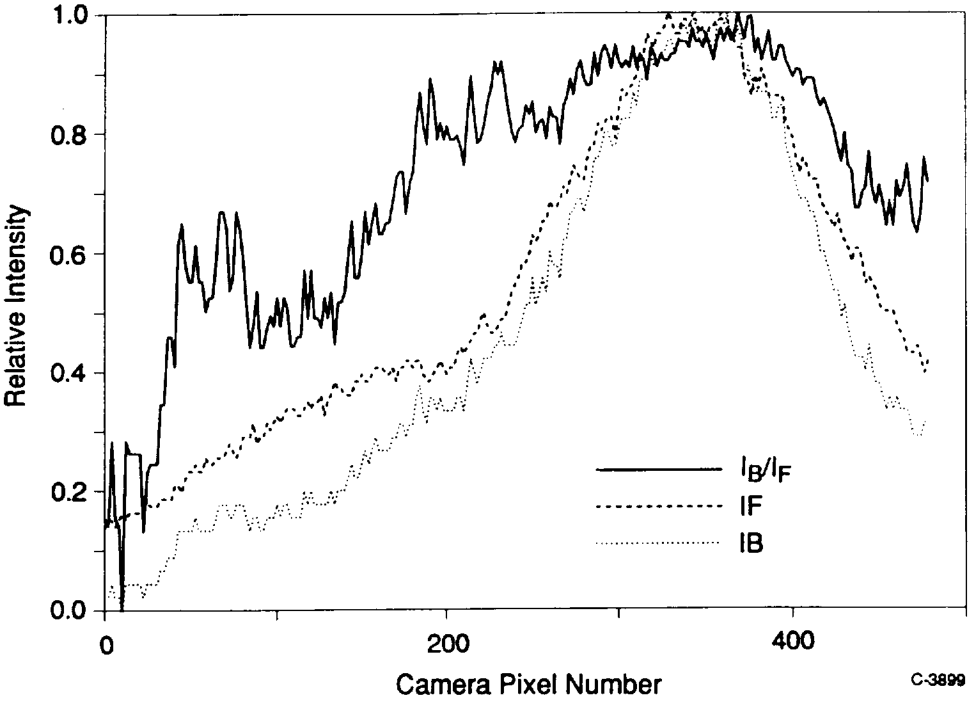

Figure 80. Plot of the Relative Sheet Intensity Distributions Before a Burner Firing

We observed that this relative overlap changed during the course of the burner operation. Figure 81 shows two images taken with the fast gating camera during a burner firing. The left image is generated from the forward propagating sheet while the right image is generated by the backward propagating sheet. Although the laser sheets were carefully aligned prior to the firing, it is evident that the backward propagating sheet is now somewhat higher in the frame than the forward propagating sheet. This is also evident in the slow gating camera image at the left of Figure 74, where the sum of the backward and forward propagating sheet image clearly shows the region of greatest laser intensity to be higher in the frame than in the forward propagating sheet recorded with the fast gating camera. This increase in the height of the backward propagating sheet was a persistent feature in all of the experiments and we were unable to specifically locate the source of the problem. After the firing, the backward sheet would eventually "sag" back to its pre-firing position, indicating that some thermal change in one of the beam steering optics may be the source. We note that the beam splitting and steering optics near the laser would have to deviate by only about 125 μrad to

PRECEDING PAGE BLANK NOT FILMED

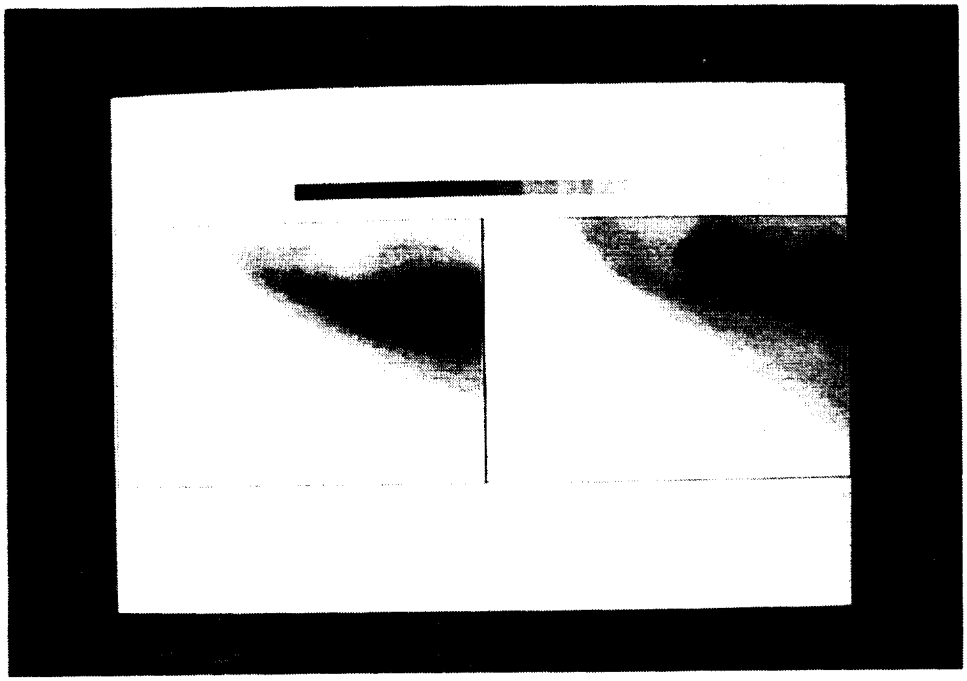

V-768

Figure 81. Comparison of PLIF Images from Forward and Backward Propagating Sheets Showing Shift of Backward Sheet

steer the backward propagating sheet by this magnitude. Remote control of the beam reflection prism might have alleviated this problem, but was beyond the program resources.

Initial data reduction revealed that this mismatch of laser sheet intensities introduced large errors in the velocity images, as indicated by the sensitivity of the velocity algorithm to the magnitude of the intensity ratio shown in Figure 77. Since the sum image acquired by the slow gating camera contained very few flow features, however, we were able to shift this image downward in the frame by about 25 rows, or about 5 percent of the total field of view, without washing out the flow features. This procedure, of course, is not strictly correct since we also translate the jet flow features and the information generated by the forward propagating sheet. However, the single image recorded by the fast gating camera from the forward propagating sheet contains the principal velocity information and the arguments presented above show that the velocity algorithm, over these flow conditions, is more sensitive to the relative sheet intensities. Figure 82 shows the shifted sum image (upper left) and the unshifted forward sheet only image (upper right) along with the ratio image obtained using Eq. 18. The upper images show that the region of highest laser intensity in the two sheets are now reasonably overlapped. The images were rescaled so that the lowest velocity regions at the edge of the jet were at the bottom of the A/D range.

Figure 83 is a plot of the velocity algorithm for this case (shifted so as to approach zero for zero velocities). For the larger range of in-plane velocity components, the non-linear nature of the algorithm (solid line) is evident when compared to a linear curve with the same slope at the origin (dashed line). The ratio image from Eq. 18 was then re-mapped to this non-linear velocity range.

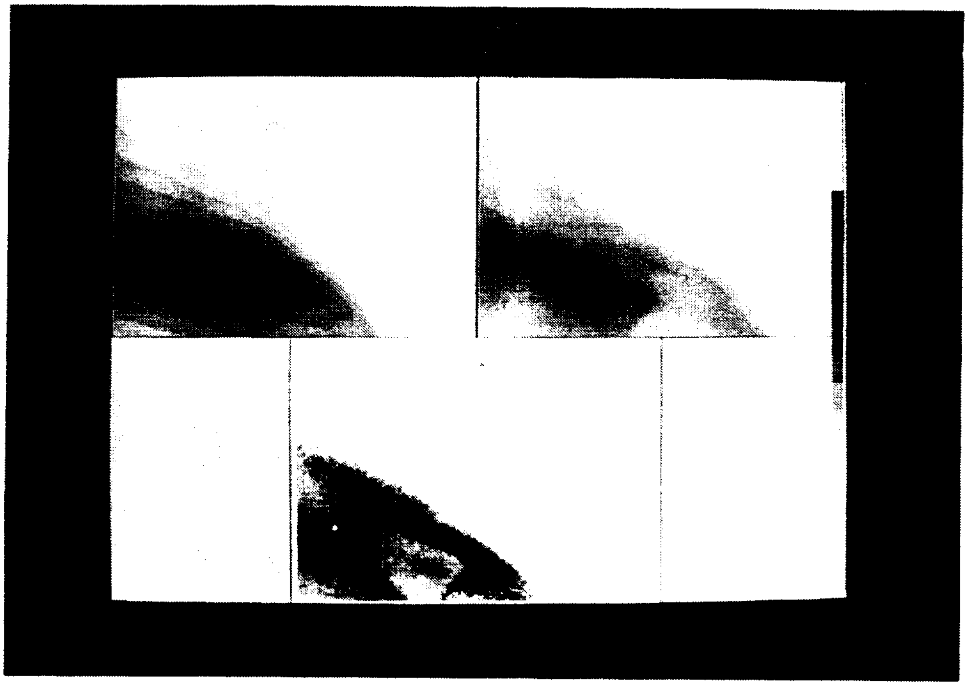

Figure 82. Example PLIF Images Used to Calculate the Angled Jet Velocity Component. Upper left: sum image; upper right: forward sheet only; lower: result of processing upper images according to Eq. 18.

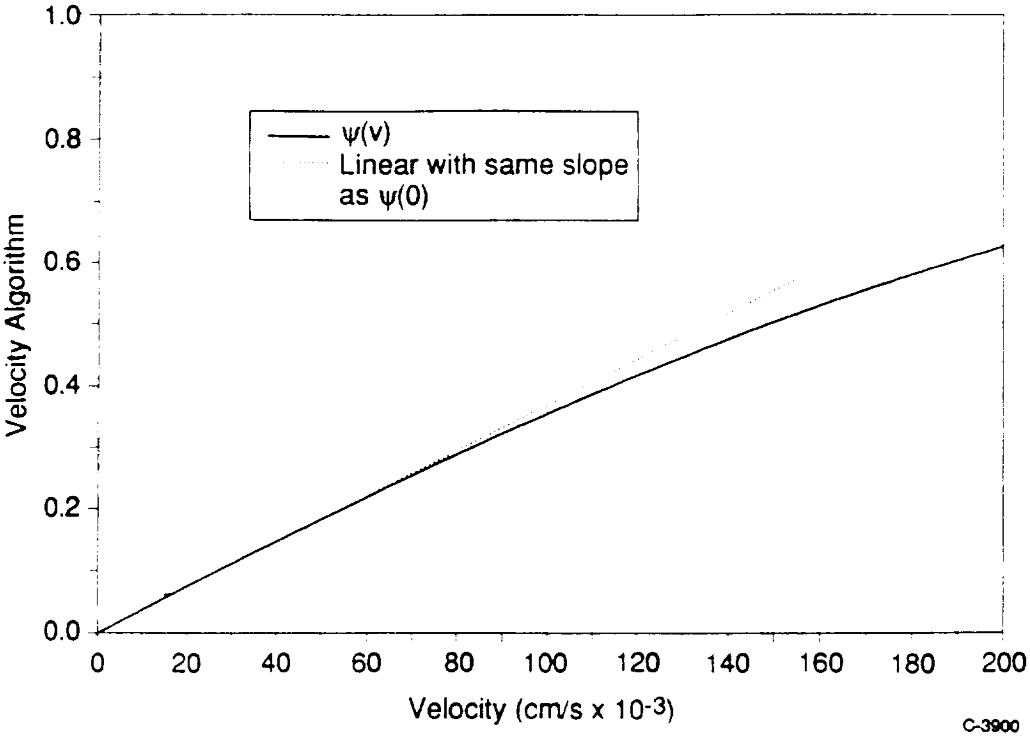

Figure 83. Velocity Algorithm for Two Camera Velocity Determinations

Figure 84 is a comparison of the velocity image obtained from the two camera determination with the 56 degree velocity component calculated by the SPARK code. The gray scale is a linear mapping of velocity from 0 to 1750 m/s. Despite the problems described above with the relative laser sheet variations, the agreement between the measured and calculate velocity distributions is reasonable. Note that the white region below the Mach disk at the bottom center of the measured velocity image is due to lack of OH fluorescence signal there and does not represent an erroneous determination of low velocity. The region of high velocity near the triple point is also observed in the data and relative velocity variations are in general correctly captured. Deviations between the measured and calculated velocity distributions near the top and bottom of the flowfield are attributable to the variations in the relative laser sheet intensity there, as plotted in Figure 80.

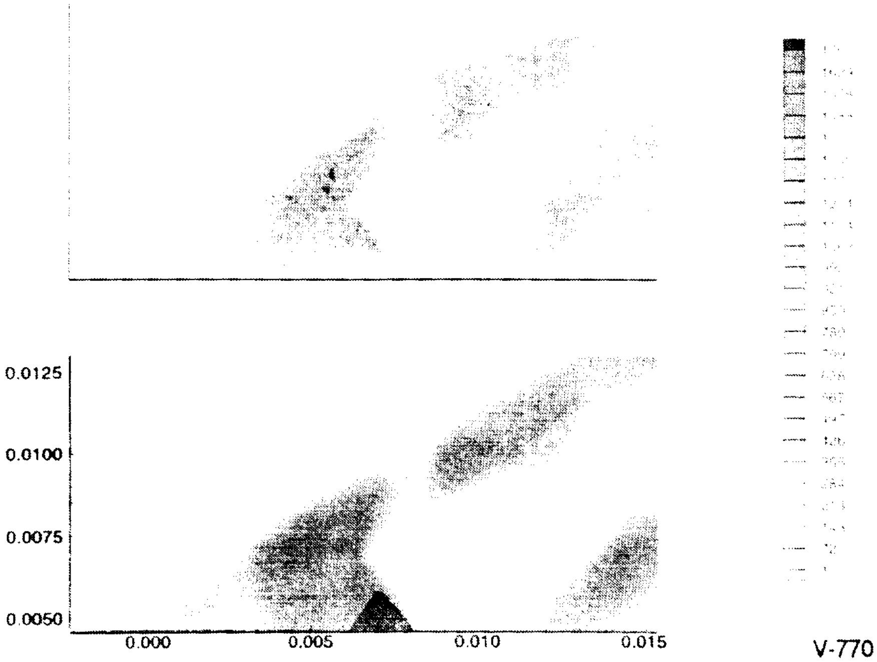

Figure 84. Comparison Between Measured and Calculated Angular Velocity Distribution

A clear difference between the measured and calculated velocity distributions is evident near the termination of the first shock cell beyond the Mach disk. The calculated flowfield evolved so that each cell terminated in a weak normal wave. Visual observation of the visible emission from the jet flow suggested that this cell in fact terminated with intersecting reflected waves. The axisymmetry of the flow results in the first shock cell terminating in a reasonably well defined cone, rather than the truncated cone predicted by the flow model. Since this is another of the viscous phenomena of the flow, we believe the code is in error in this region of the flowfield. A more sophisticated compressible turbulence model would be required to improve the performance of the calculation.

A second comparison is shown in Figure 85. The measured velocity distribution corresponds to the same experimental conditions as in Figure 84, although the measurements were obtained about 5 minutes later during the same burner firing. Data sets were also acquired with the fast gating camera delayed so as to capture the image from the backward going sheet. After processing with the appropriately modified velocity algorithm, the velocity distributions were generally similar to those shown here, although the lower signal

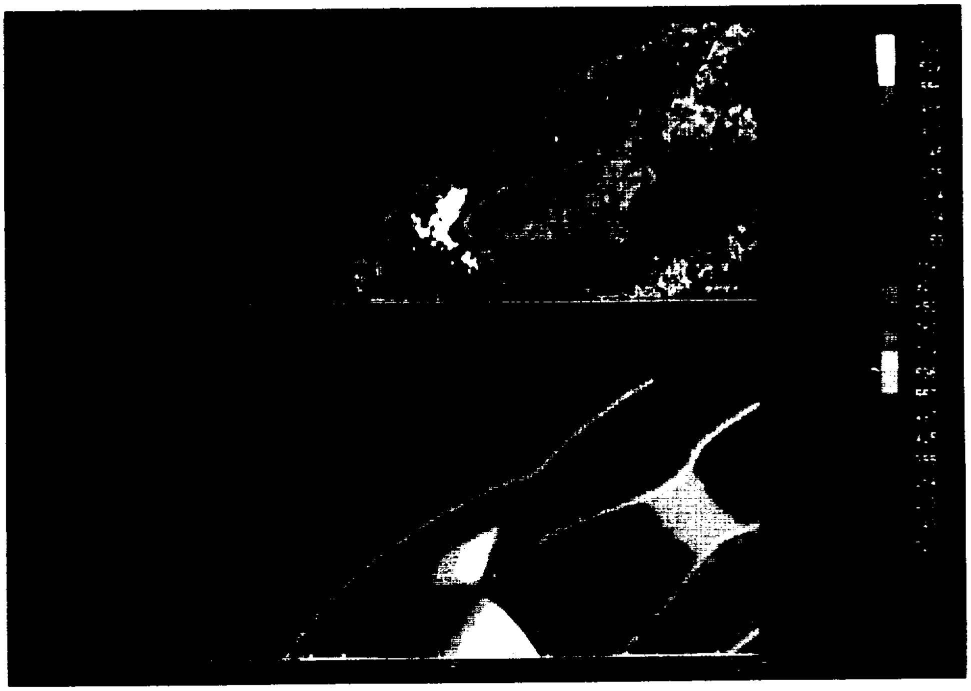

V-771

Figure 85. Comparison Between Measured and Calculated Angular Velocity Distribution

levels in the backward propagating sheet resulted in a higher overall noise level. All of the successful velocity imaging determinations were obtained from detuning the laser to higher frequencies. Although, in principle, the detuning should be nominally symmetric (leaving aside small effects due to the collisional shifting), we found that detuning to lower frequencies resulted in the forward propagating sheet being shifted up to line center where the laser attenuation discussed above distorted the images. This indicates that small laser attenuation effects, not necessarily significant in conventional PLIF concentration measurements, must be carefully considered in devising a successful strategy for velocity imaging.

Since the dominant source of error in the two camera experiments arose from an experimental artifact, it is not straightforward to determine a single figure of merit for the accuracy of the technique as demonstrated in these experiments. The single camera demonstrations are free from the relative laser sheet intensity artifacts and are perhaps a better measure of the ultimate accuracy of the technique. In these images, the relative velocity uncertainty is on the order of ± 50 m/s out of a total dynamic range of 1600 (-830 m/s $< v <$ 830 m/s), or about 3 percent. This uncertainty appears to be limited by the shot noise statistics in the image rather than any systematic error due to the changing thermodynamic conditions in the flowfield. Of course, this low uncertainty has been achieved by averaging together 24 images. The single shot uncertainty would be about 15 percent for these experimental conditions. Improvements in the available laser pulse energy would reduce the single shot uncertainty.

The angular velocity determinations are also shot noise limited. Figures 84 and 85 were calculated from the average of 24 slow gating images and 12 fast gating images. The random velocity variation due to the shot noise is about ± 200 m/s, or 12 percent of the total dynamic range. Systematic errors due to the variations in the relative laser sheet intensity increase this uncertainty near the edges of the laser sheets. Since the pulse energy for each PLIF image is less than half of that used in the radial velocity determination, PAGE [illegible] INTENTIONALLY BLANK

the single shot uncertainty is concomitantly higher. At these low energy levels (less than 1 mJ/pulse) the single shot uncertainty of the fast-gating camera image approaches 40 percent. Attempts to calculate velocity images from selected single-pulse data were plagued by these large, random uncertainties which essentially masked most significant flow features.

Clearly accurate velocity mapping at these pressures, temperatures, and OH concentration levels requires more laser energy than was available from our pulsed dye laser. Pumping with XeCl instead of XeF would approximately double the output pulse energy. In general, however, currently available excimer-pumped dye lasers, while possessing the required spectral characteristics, will not produce more than about 5 mJ/pulse around 283 nm. Other pulsed dye laser systems, however, can produce 30 to 40 mJ at these wavelengths. These energy levels would permit true single shot velocity imaging with acceptable uncertainties. Our examination of the Spectra-Physics PDL-series dye lasers determined that their pulse-to-pulse spectral stability was not adequate for velocimetry applications. Other manufacturers, however, such as Lumonics, market dye lasers with higher single pulse output energy and claim to have better spectral purity than the Spectra-Physics products. If single-shot velocity imaging is a stringent requirement, this or some other dye laser should be explored to verify that its spectral stability is sufficient for velocimetry applications. Additional improvements could be obtained with higher quantum efficiency in the fast-gating camera. Nevertheless, the velocity imaging technique has been demonstrated, and single-short imaging is possible using the results developed in this program.

PRECEDING PAGE BLANK NOT FILMED

7. SUMMARY AND CONCLUSIONS

This report details the results of a combined experimental and analytical demonstration of the applicability of Doppler-shifted OH PLIF velocimetry in the high pressure, high temperature flowfields relevant to practical supersonic combustion devices. As a part of this development, the state of the art in fluorescence-based flow diagnostics has been advanced in several ways.

Firstly, a detailed set of accurate measurements of the OH (1,0) band collisional broadening and shifting parameters in H_2-air combustion environments was produced. These are the first such measurements of these transitions and the most accurate OH broadening measurements published to date. In addition to providing important information required for the general application of OH fluorescence flow diagnostic, and OH velocimetry in particular, these results shed new light on the fundamental relationship between broadening collisions and energy transfer collisions in OH A $^2\Sigma^+$ $v' = 1$.

Secondly, the single- and multi-pulse spectral properties of widely-used pulsed dye lasers were characterized for the first time. We showed that a common Nd:YAG-pulsed dye laser system in flow diagnostic applications, the Spectra-Physics PDL-series, exhibited significant pulse-to-pulse bandshape fluctuations. While not a barrier to fluorescence concentration or thermometry measurements, these fluctuations would likely prohibit meaningful velocity measurements. A second prevalent dye laser system, the Lambda-Physik FL-series, was shown to exhibit multiple axial mode bandshapes with a single-pulse bandshape which was considerably more narrow than the manufacturer's published specifications. The spectral stability of this laser, however, was superior and, with an intra-cavity modification, we were able to achieve stable, relatively broadband laser bandshapes from this laser. This work helped uncover the general issue of the spectral properties of pulsed dye lasers in flow diagnostics research.

A stable, high pressure H_2-air burner was developed, providing a reproducible source of high pressure, high temperature combustion gases. The underexpanded jet exhaust flow was calculated with a finite-rate chemistry, 2-D Navier Stokes simulation code. The results of this modelling were compared with available experimental correlations and with mean velocity measurements along the jet centerline. The agreement between the model, the literature properties, and the measured variations was generally very good. The model was subsequently used to guide the strategies employed in the velocimetry demonstrations and to judge the accuracy of the imaging velocimeter's results. This integrated application of CFD modelling and advanced diagnostic development is an important step in the continued advancement of flow diagnostics and highlights the importance of such synthetic experimental/analytical efforts in studies of turbulent reacting flows.

Finally, the various technical efforts of the program were brought together in a series of experiments demonstrating the applicability of OH Doppler-shifted PLIF velocimetry in high pressure, high temperature combustion flows. The series consisted of a sequence of increasingly complex experimental configurations. In the simplest, a single camera, single laser configuration for mean velocity measurements in flows with an axis of symmetry, we demonstrated velocity imaging with an accuracy of ± 50 m/s out of a dynamic range of 1600 m/s. This accuracy was achieved despite an order of magnitude variation in pressure and a factor of two variation in temperature across the measurement plane. This demonstration succeeded in the essential goals of the program.

Velocity imaging was also demonstrated in a more complex configuration involving two cameras and a single laser. Although experimental artifacts specific to our setup precluded true single-shot imaging, the basic approach was validated. These demonstrations highlighted the importance of generating and maintaining uniform relative laser sheet intensity distributions in the experiments. This report contains a detailed exposition of all the technical effort involved in the velocimetry demonstrations. It should serve as guide to the diagnostic user community in extending the application of this technique to practical aerospace test facilities.

Acknowledgements

The authors gratefully acknowledge assistance from several knowledgeable sources. Robert Anderson, the NASA technical monitor, provided consistent guidance, including support of the design and analysis of the high-frequency pressure transducer, and securing CRAY computer time from NASA Lewis to support the SPARK modeling. Erwin Lezberg and Ray Gaugler, also of NASA-Lewis, consulted in the design of the supersonic burner and the heat transfer analysis of the nozzle. David Rossi and Kevin Friel, of PSI, assembled the burner, gas delivery, and safety systems. Phillip Paul, Sandia National Laboratory, and Bernd Nikolaus, Lambda-Physik, suggested possible laser bandshape modification strategies. Albert Chang and Mike DiRosa, from Stanford University, along with Phillip Varghese, from the University of Texas, assisted us with the non-linear lineshape fitting routines. Our SPARK modeling efforts were enhanced by discussions with Prof. Haj-Hariri, of the Universtiy of Virginia, as well as Dean Ecklund and Phil Drummond of NASA Langley.

8. REFERENCES

1. Hiller, B. Booman, R.A., Hassa, C., and Hanson, R.K., "Velocity Visualization in Gas Flows Using Laser-Induced Phosphorescence of Biacetyl," *Rev. Sci. Instrum.* 55(12), 1964 (1984).

2. Miles, R.B., Connors, J.J., Markovitz, E.C., Howard, P.J., and Roth, G.J., "Instantaneous Profiles and Turbulence Statistics of Supersonic Free Shear Layers By Raman Excitation Plus Laser-Induced Electronic Fluorescence (RELIEF) Velocity Tagging of Oxygen," *Exp. in Fluids* 8, 17 (1989).

3. Boedeker, L.R., "Velocity Measurement By H_2O Photolysis and Laser-Induced Fluorescence of OH," *Opt. Lttrs.* 14(10), 473 (1989).

4. Goss, L.P., Chen, T.H., Trump, D.D., Sarka, B., and Nejad, A.S., "Flow-Tagging Velocimetry Using UV-Photodissociation of Water Vapor," Paper No. 91-0355, presented at the 29th Aerospace Sciences Meeting, Reno, 1991.

5. Measures, R.M., "Selective Excitation Spectroscopy and Some Possible Applications," *J. Appl. Phys.* 39, 5232 (1968).

6. Zimmerman, M. and Miles, R.B., "Hypersonic-Helium-Flowfield Measurements with the Resonant Doppler Velocimeter," *Appl. Phys. Lett.* 37, 885 (1980).

7. Chang, A.Y., Battles, B.E., and Hanson, R.K., "Simultaneous Measurements of Velocity, Temperature, and Pressure Using Rapid CW Wavelength-Modulation LIF of OH," *Opt. Lttrs.* 15(12), 706 (1989).

8. Klavuhn, K.G., Gauba, G., and McDaniel, J.C., "High-Resolution OH LIF Velocity Measurement Technique for High-Speed Reacting Flows," AIAA Paper No. 92-3422, presented at the 28th Joint Propulsion Conference, Nashville (1992).

9. McDaniel, J.C., Hiller, B., and Hanson, R.K., "Simultaneous Multiple-Point Velocity Measurements Using Laser-Induced Iodine Fluorescence," *Opt. Lttrs.* 8(1), 51 (1983).

10. Hiller, B., McDaniel, J.C., Rea, E.C., Jr., and Hanson, R.K., "Laser-Induced Fluorescence Technique for Velocity Field Measurements in Subsonic Gas Flows," *Opt. Lttrs.* 8(9), 474 (1983).

11. Hiller, B. and Hanson, R.K., "Simultaneous Planar Measurments of Velocity and Pressure Fields in Gas Flows Using Laser-Induced Fluorescence," *App. Opt.* 27(1), 33 (1988).

12. Paul, P.H., Lee, M.P., and Hanson, R.K., "Molecular Velocity Imaging of Supersonic Flows Using Pulsed Planar Laser-Induced Fluorescence of NO," *Opt. Lttrs.* 14(9), 417 (1989).

13. Palmer, J.L., McMillin, B.K., and Hanson, R.K., "Planar Laser-Induced Fluorescence Imaging of Velocity and Temperature in Shock Tunnel Free Jet Flow," AIAA Paper No. 92-0767, presented at the 30th Aerospace Science Meeting, Reno (1992).

14. Engleman, R.,"Collision Broadening of Transient Absorption Spectra 1. Hydroxyl Linewidths in the (0,0) (A-X) Transition at Low Temperatures," *J. Quant. Spectrosc. Radiat. Transfer* 9, 391 (1969).

a-2

15. Wang, C.C., Killinger, D.K., and Huang, C.-M., "Rotational Dependence in the Linewidth fo the Ultraviolet Transitions of OH," *Phys. Rev. A* **22**, 188 (1980).

16. Shirinzadeh, B., Bakalyar, D.M., and Wang, C.C., "Measurement of Collision-Induced Shift and Broadening of the Ultraviolet Transitions of OH," *J. Chem. Phys.* **82**, 2877 (1984).

17. Rea, E.C., Jr., Chang, A.Y., and Hanson, R.K., "Shock-Tube Study of Presssure Broadening of the A $^2\Sigma^+$ - X $^2\Pi$ (0,0) Band of OH by Ar and N_2," *J. Quant. Spectrosc. Radiat. Transfer* **37**, 117 (1987).

18. Nadler, M., and Kaskan, W.E., "Collisional Broadening of OH $^2\Sigma^+$ - $^2\Pi$ Lines in Flames," *J. Quant. Spectrosc. Radiat. Transfer* **10**, 25 (1970).

19. Rea, E.C., Jr., Chang, A.Y., and Hanson, R.K., "Collisional Broadening of the A $^2\Sigma^+$ - X $^2\Pi$ (0,0) Band of OH by H_2O and CO_2 in Atmospheric-Pressure Flames," *J. Quant. Spectrosc. Radiat. Transfer* **41**, 29, (1989).

20. Copeland, R.A., Wise, M.L. and Crosley, D.R., "Vibrational Energy Transfer and Quenching of OH (A $^2\Sigma^+$, $v'=1$)", *J. Phys. Chem.* **92**, p. 5710 (1988).

21. Kessler, W.J., Allen, M.G., and Davis, S.J., "Rotational Level-Dependent Collisional Broadening and Line Shift of the A $^2\Sigma^+$ - X $^2\Pi$ (1,0) Band of OH in Hydrogen-Air Combustion Gases," *J. Quant. Spectrosc. Radiat. Transfer* **49**(2), p. 107, (1993).

22. Armstrong, J.A., Bloembergen, N., Ducuing, J., and Pershan, P.S., "Interactions Between Light Waves in a Nonlinear Dielectric," *Phys. Rev.* **127**(6), p. 1918, (1962).

23. Kajava, T.T., Lauranto, H.M., and Salomaa, R.R.E., "Mode Structure Fluctuations in a Pulsed Dye Laser," *App. Opt.* **31**(33), p. 6987, (1992).

24. Nyland, T.W., Englund, D.R., and Anderson, R.C., "On the Dyanmics of Short Pressure Probes: Some Design Factors Affecting Frequency Response," NASA TN D-6151, Lewis Res. Ctr. (1971).

25. Bergh, H. and Tijdeman, H., "Theoretical and Experimental Results for the Dynamic Response of Pressure Measuring Systems," Report NLR-TR-F238, Natioanl Aero- and Astronautical Res. Inst., Amsterdam, 1965.

26. Dash, S.M. and Wolf, D.E., "Interactive Phenomena in Supersonic Jet Mixing Problems, Part I: Phenomenology and Numerical Modelling Techniques," *AIAA J.* **22**(7), p. 905, (1984).

27. Ewan, B.C.R. and Moodie, K., "Structure and Velocity Measurements in Underexpanded Jets," *Combust. Sci. and Tech.* **45**, p. 275 (1986).

28. Crist, S., Sherman, P.M., and Glass, D.R., "Study of the Highly Underexpanded Sonic Jet," *AIAA J.* **4**(1), p. 68, (1966).

29. Askenas, H. and Sherman, F.S., "The Structure and Utiliztion of Supersonic Free jets in Low Density Wind Tunnels," in *Rarefied Gas Dynamics 2*, p. 84, Academic Press, New York, (1966).

30. Fox, J.H., "On the Structure of Jet Plumes," *AIAA J.* 12(1), p. 105, (1974).

31. Dash, S.M., Wolf, D.E., and Seiner, J.M., "Analysis of Turbulent Underexpanded Jets, Part I: Parabolized Navier-Stokes Model, SCIPVIS," *AIAA J.* 10(1), p. 112, (1972).

32. Anderson, J.B., "Inviscid Freejet Flow with Low Specific Heat Ratios," *AIAA J.* 10(1), p. 112, (1972).

33. Hiller, B., "Combined Planar Measurements of Velocity and Pressure Fields in Compressible Gas Flows Using Laser-Induced Iodine Fluorescence," Ph.D. Thesis, Department of Mechanical Engineering, Stanford University, (1986).

34. Drummond, J.P., "A Two-Dimensional Numerical Simulation of a Supersonic, Chemically Reacting Mixing Layer," NASA Technical Memorandum 4055, December 1988.

35. Carpenter, M.H., "Three Dimensional Computations of Cross-Flow Injection and Combustion in a Supersonic Flow," AIAA Paper 89-1870, June 1989.

36. Klavuhn, K.G., Gauba, G. and McDaniel, J.C., "High-Resoution OH LIF Velocity Measurement Technique for High-Speed Reacting Flows," AIAA Paper 92-3422, July 1992.

37. Drummond, J.P., "Numerical Solution for Perpendicular Sonic Hydrogen Injection into a Ducted Supersonic Airstream," *AIAA J.*, 17(5), 531, May 1979.

38. MacCormack, R.W., "The Effect of Viscosity on Hypervelocity Impact Cratering," AIAA Paper 69-354, April-May 1969.

39. Eklund, D.R., Northam, G.B., and Fletcher, D.G., "A Validation of the SPARK Navier-Stokes Code for Nonreacting Scramjet Combustor Flow Fields," AIAA Paper No. 90-2360, July 1990.

40. Eklund, D.R., Northam, G.B., and Hartfield, R.J., "A Detailed Investigation of Staged Normal Injection into a Mach 2 Flow," 27th JANNAF Combustion Meeting, November 5-9, 1990.

41. Segal, C., Haj-Hariri, H., and McDaniel, J.C., "A Numerical Investigation of Hydrogen Combustion in a Mach 2 Airflow," AIAA Paper No. 92-0341.

42. Rigghs, D.W. and McClinton, C.R., "A Computational Investigation of Flow Losses in a Supersonic Combustor," AIAA Paper 90-2393, July 1990.

43. Carpenter, M.H., "The Effects of Finite-Rate Chemical Processes on High Enthalpy Nozzle Performance: A Comparison Between SPARK and SEAGULL," AIAA Paper No. 88-3157, 1988.

44. Smith, R.E., and Weigel, B.L., Analytic and Approximate Boundary-Fitted Coordinate Systems for Fluid Flow Simulation," AIAA Paper 80-0192, January 1980.

45. Sangiovanni, J.J., Barber, T.J., and Syed, S.A., "The Role of Hydrogen/Air Chemistry in Nozzle Performance Simulation for Hypersonic Propulsion Systems," AIAA Paper 90-2492, 26th Joint Propulsion Conference, July 1990.

46. Harradine, D., Lyman, J., Oldenborg, R., Schott, G., and Watanabe, H., "Hydrogen/Air Combustion Calculations: The Chemical Basis of Efficiency in Hypersonic Flows," AIAA Paper 88-2713, Thermophysics, Plasmadynamics, and Laser Conference, June 1988.

47. H. Haj-Hariri, Private communication, September 1992.

48. Barlow, R.S. and Collignon, A., "Linear LIF Measurements of OH in Nonpremixed Methane-Air Flames: When are Quenching Corrections Unnecessary?," AIAA Paper 91-0179, 29th Aerospace Sciences Meeting, 1991.

49. Cattolica, R.J., and Mataga, T.G., "Rotational-Level-Dependent Quenching of OH A $^2\Sigma^+$ ($v'=1$) by Collisions with H_2O in a Low Pressure Flame, *Chem. Phys. Lett.* 182(6), p. 623, 1991.

REPORT DOCUMENTATION PAGE

Form Approved
OMB No. 0704-0188

Public reporting burden for this collection of information is estimated to average 1 hour per response, including the time for reviewing instructions, searching existing data sources, gathering and maintaining the data needed, and completing and reviewing the collection of information. Send comments regarding this burden estimate or any other aspect of this collection of information, including suggestions for reducing this burden, to Washington Headquarters Services, Directorate for Information Operations and Reports, 1215 Jefferson Davis Highway, Suite 1204, Arlington, VA 22202-4302, and to the Office of Management and Budget, Paperwork Reduction Project (0704-0188), Washington, DC 20503.

1. AGENCY USE ONLY *(Leave blank)*	**2. REPORT DATE** September 1993	**3. REPORT TYPE AND DATES COVERED** Final Contractor Report

4. TITLE AND SUBTITLE Instantaneous Velocity Field Imaging Instrument for Supersonic Reacting Flows	**5. FUNDING NUMBERS** WU–324–02 C–NAS3–26254
6. AUTHOR(S) M.G. Allen, S.J. Davis, W.J. Kessler, H.H. Legner, K.R. McManus, P.A. Mulhall, T.E. Parker, and D.M. Sonnenfroh	
7. PERFORMING ORGANIZATION NAME(S) AND ADDRESS(ES) Physical Sciences Incorporated 20 New England Business Center Andover, MA 01810	**8. PERFORMING ORGANIZATION REPORT NUMBER** E–8131
9. SPONSORING/MONITORING AGENCY NAME(S) AND ADDRESS(ES) National Aeronautics and Space Administration Lewis Research Center Cleveland, Ohio 44135–3191	**10. SPONSORING/MONITORING AGENCY REPORT NUMBER** NASA CR–191162

11. SUPPLEMENTARY NOTES

Project Manager, Robert C. Anderson, Instrumentation and Control Technology Division, (216) 433–3643.

12a. DISTRIBUTION/AVAILABILITY STATEMENT Unclassified - Unlimited Subject Category 35	**12b. DISTRIBUTION CODE**

13. ABSTRACT ***(Maximum 200 words)***

This report describes the technical tasks conducted to develop and demonstrate a new gas velocity measurement technique for high enthalpy reacting flows. The technique is based on Doppler-shifted Planar Laser-Induced Fluorescence (PLIF) imaging of the OH radical. The imaging approach permits, in principle, single-shot measurements of the 2-D distribution of a single velocity component in the measurement plane, and is thus a technique of choice for applications in high enthalpy transient flow facilities. In contrast to previous work in this area, the present program demonstrated an approach which modified the diagnostic technique to function under the constraints of practical flow conditions of engineering interest, rather than vice-versa. In order to accomplish the experimental demonstrations, the state-of-the-art in PLIF diagnostic techniques was advanced in several ways. This report describes each of these tasks in detail and is intended to serve as a reference in supporting the transition of this new capability to the fielded PLIF instruments now installed at several national test facilities. Among the new results of general interest in LIF-based flow diagnostics, this report includes a detailed set of the first measurements of the collisional broadening and shifting behavior of OH (1,0) band transitions in H_2-air combustion environments. Such measurements are critical in the design of a successful strategy for PLIF velocity imaging; they also relate to accurate concentration and temperature measurements, particularly in compressible flow regimes. Furthermore, the results shed new light on the fundamental relationship between broadening and energy transfer collisions in OH $A\,^2\Sigma^+$ v' = 1. The first single-pulse, spectrally-resolved measurements of the output of common pulsed dye lasers were also produced during the course of this effort. As with the OH broadening measurements, these data are a significant aspect of a successful velocity imaging strategy, and also have potential implications for many other LIF measurement techniques. Our results indicated the need to modify the commercially available laser cavity in order to accommodate the constraints imposed by typical SCRAMJET combustion characteristics as well as to increase the instrument's velocity dynamic range to span an intra-image range in excess of 2 km/s. The various technical efforts were brought together in a series of experiments demonstrating the applicability of the technique in a high pressure, high temperature H_2-air combustion system. The resultant images were compared with 2-D flow simulations in order to determine the accuracy of the instrument. Mean velocity imaging in flows with an axis of symmetry was demonstrated with an accuracy of ±50 m/s out of an intra-image dynamic range of 1600 m/s, including reversed flow. A more complex configuration amenable to single-shot imaging in flows without an axis of symmetry was also demonstrated. Limitations imposed by available equipment resulted in an accuracy of about ±200 m/s out of 1750 m/s in these demonstrations. Minor modifications to the present configuration were suggested to improve this performance. In the following pages, each technical task is described in detail, along with significance of the results for the overall imaging velocimeter configuration. This report should allow the user community to integrate this new measurement capability into their existing instrumentation platforms.

14. SUBJECT TERMS Laser applications; Laser-induced fluorescence; Velocity measurements; Gas flow measurement; Supersonic flow	**15. NUMBER OF PAGES** 97
	16. PRICE CODE A06

17. SECURITY CLASSIFICATION OF REPORT Unclassified	**18. SECURITY CLASSIFICATION OF THIS PAGE** Unclassified	**19. SECURITY CLASSIFICATION OF ABSTRACT** Unclassified	**20. LIMITATION OF ABSTRACT**